Model and Test of an Actively Controlled Cryogenic Micro Valve

by

Tyler R. Brosten

A thesis submitted in partial fulfillment of
the requirements for the degree of

MASTER OF SCIENCE
(MECHANICAL ENGINEERING)

at the

UNIVERSITY OF WISCONSIN-MADISON

2006

Model and Test of an Actively Controlled Cryogenic Micro Valve

Tyler R. Brosten

Under the supervision of Professor Greg F. Nellis
at the University of Wisconsin – Madison

ABSTRACT

Future NASA missions require cooling of large optical structures, cryogen storage systems, and instrument chambers and therefore cooling must be applied in a controlled and efficient fashion over a large spatial extent. A cooling system that uses an actively controlled, micro-scale valve may be integrated with heat exchangers and sensors in order to allow the individual branches of a distributed cooling system to be independently controlled in response to local temperature changes. The ability to control the flow area associated with the valve increases the efficiency and flexibility of the distributed cooling system by allowing the cooling to be concentrated according to need. Previous work has selected a suitable micro valve design that addresses the required specifications. However, the precise nature of the flow behavior inside the micro valve was not addressed. Therefore, this thesis focuses on the modeling and test of the pressure-flow behavior of a micro-scale valve over a range of operating conditions.

Variable voltage actuation of the PZT actuator within the micro-valve modulates the flow area and therefore the pressure distribution and fluid flow behavior. Fluid-structure models were developed to predict the pressure distribution and flow rates. Experimental data from prototype micro valves was used to validate the analytical predictions.

Approved: _____

Professor Greg F. Nellis
Department of Mechanical Engineering
University of Wisconsin-Madison

Acknowledgements

For most students to excel, a certain amount of belief and understanding is required by those above them. My case is no acceptation. I would like to thank Professor Nellis and Professor Klein for giving me the opportunity to work on this project and their belief in my capabilities as a student. Professor Nellis in particular has been influential in my overall understanding of how to approach and solve problems. I hope to one day instill upon my students the qualities in which Professor Nellis and Professor Klein continually grant to their students.

I would also like to thank Dan Hoch for his patience and desire to teach me his wide array of technical skills. Also I would like to thank Ryan Taylor for helping on a number of topics both inside and outside of this project. The hard work of Jong Park was also instrumental in allow me to complete my project.

The knowledge and experience gained by those who have helped me at UW-Madison will last a lifetime. Thank you everyone.

Table of Contents

List of Figures

List of Tables

List of Symbols

α ..... groove aspect ratio

$A_{applied}$ ..... area which is pressurized on the Pyrex© face

$A_{c,g}$ ..... cross-sectional area of the groove

A_{epoxy} ..... area of the epoxy normal to the Pyrex© face

A_i ..... pre-contraction areas perpendicular to the direction of flow

A_o ..... flow area associated with the land

$C_{i,j}$ ..... linearization constant

δ ..... clearance between the land surface and the Pyrex seat

$\delta_{const\text{-}diff}$ ..... difference between the experimental data and FE model

δ_o ..... initial seat displacement

δ_s ..... structural seat displacement

δ_v ..... seat displacement from voltage actuation

D_h ..... hydraulic diameter of the groove

dx,dy ..... nodal separation distances

d_2 ..... inlet diameter

d_1 ..... exit cone throat diameter

d_g ..... groove depth

E_{epoxy} ..... elastic modulus of the epoxy joint

F_{geom} ..... ratio of the pressure drop in the groove to the total pressure drop

f ..... friction factor

γ ..... ratio of specific heats for the gas or fluid flowing through the land

g_s ..... groove entrance spacing

h_c ..... inlet cone height

g_w ..... groove entrance width

hg,lg ..... high and low pressure groove subscripts

i,j ..... x,y location of the mesh

K ..... constant that depends on the groove aspect ratio

K_c, K_e ..... inertial coefficients

$K_{c\text{-}g}$ ..... inertial contraction coefficient for entrance into the high pressure groove

K_l ..... inertial correlation coefficient

Kn_δ ..... Knudsen number based on the valve seat clearance

l ..... land subsript

l_g ..... groove length

m_h ..... manifold height

m_w ..... manifold width

m_l ..... manifold length

$\dot{m}$ ..... mass flow rate

$\dot{m}_{est}$ ..... linearized inertial mass flow rate

$\bar{\dot{m}}$ ..... non-dimensional mass flow rate

$\dot{m}_{characteristic}$ ..... characteristic mass flow rate

μ ..... viscosity

M ..... Mach number

$\dot{m}'$ ..... compressible mass flow rate per unit channel width

m_r ..... mass flow ratio

m,n ..... integers

N_g ..... number of half grooves in the valve

p,P ..... local pressure

P_g ..... area averaged pressure groove pressure

P_o ..... outlet pressure

P_r ..... ratio of inlet pressure to the outlet pressure

per_g ..... perimeter of the groove

ΔP_h ..... total pressure drop through the manifold

P_{low} ..... low pressure groove exit pressure

P_{high} ..... high pressure groove inlet pressure

P_{inlet} ..... valve inlet pressure

P_{outlet} ..... valve outlet pressure

R ..... ideal gas constant

Re ..... Reynolds number based on the valve seat clearance

ρ ..... density

Re_{land} ..... ratio of inertial to viscous pressure loss over the land

σ ..... tangential momentum accommodation coefficient

T ..... valve temperature

t_{epoxy} ..... epoxy joint thickness

u ..... x direction velocity

u_m ..... x direction bulk velocity

v ..... y direction velocity

V ..... local mean velocity magnitude

v_m ..... y direction bulk velocity

V_g ..... mean x-axis velocity in the groove

V_l ..... mean flow velocity over the land

w_{tip} ..... width of the tip

w_g ..... groove width

w_l ..... land width

w_{tip} ..... width of the tip

Chapter 1

INTRODUCTION

1.1 Actively Controlled Cooling Systems

A system capable of actively controlling the temperature of a device or process with a high degree of stability could be used in many fields of industry; one specific application of such technology would be to cool hardware and instruments for future space missions. The temperature sensitivity and extreme thermal environment that characterize the application future space flight hardware provide the motivation and design guidelines for the development of the actively controlled cooling system considered in this thesis. Such a system will use a distributed cooling network employing actively controlled valves that are directly integrated with heat exchangers and sensors. Each cooling branch of the network might work independently in response to local temperatures measured by these integrated temperature sensors so that the temperature distribution over a large spatial area can be controlled with a high degree of accuracy and stability. The cooling for such a system could be realized in a variety of ways; the simplest is the use of cryogenic fluid supplied at constant temperature, as shown in Fig. 1.1. Note that while Fig. 1.1 shows a central computer controlling the valves it is possible that the control logic would be distributed as well as the physical hardware.

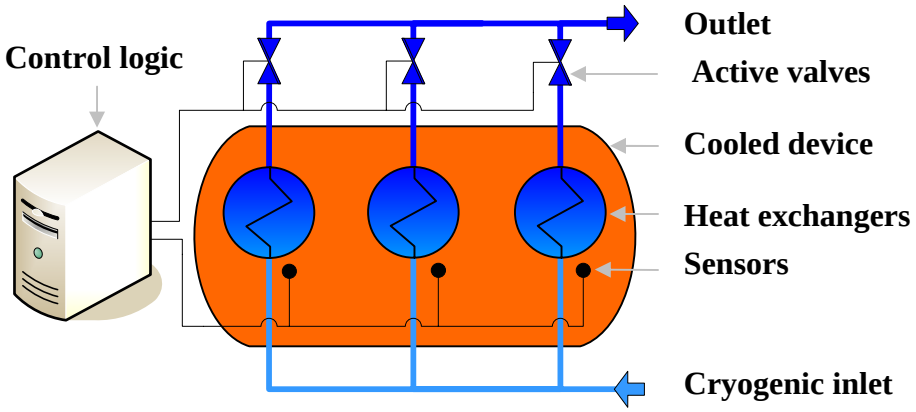

Figure 1.1: Actively controlled valves in a distributed cooling system

1.2 Active Micro Valve Design

The transient flow control required by the dynamic cooling network shown in Fig. 1.1 relies on actively controlled valves. The technical requirements for these active valves are stringent. In order to allow a large number of cooling branches to be used in order to provide distributed cooling over a large area without significantly affecting the total size and mass of the system it is desirable that the size of the active valves is limited to the MEMS scale. The active micro valves must exhibit a high degree of flow modulation, at least an order of magnitude; this will allow the system to respond to a wide range of operating conditions, provide a large amount of cooling for quick response, and essentially shut off cooling for de-activated portions of the system. Due to the intended operation in a space environment, the micro valve design must maintain functionality at cryogenic helium temperatures. To address these and other requirements, a literature review and preliminary analysis has been conducted and this effort has resulted in a suitable preliminary design for the active micro valve (Taylor 2005).

The general design that has been selected for the micro valve considered in this thesis forces a silicon micro machined plate against a fixed Pyrex® substrate containing the inlet and outlet ports. The positioning of the silicon plate relative to the Pyrex® substrate is accomplished through voltage driven, out-of-plane, stacked, piezoelectric (PZT) block-shaped actuators. PZT actuators provide small displacement, typically a few micro-meters, even at room temperature and their performance is degraded somewhat at cryogenic temperatures (Taylor 2005). However, the PZT actuators provide a large force which makes them robust to friction and allows them to withstand high operating pressures. Also, these actuators consume little power when energized which is extremely important for a cryogenic application.

To overcome the displacement limitations of PZT actuators while allowing a high degree of flow modulation, a perimeter augmentation design was incorporated into the silicon plate. A series of alternating high and low pressure grooves are connected to a high and low pressure distribution manifold in order to provide a large flow area in a limited volume. The structural shell of the valve is made from the machine-able glass ceramic, Macor®, which was selected for its low porosity, low thermal thermal coefficient of expansion at cryogenic temperatures, and low out-gassing which limits contamination. The valve design is summarized by the cut away view shown in Fig. 1.2.

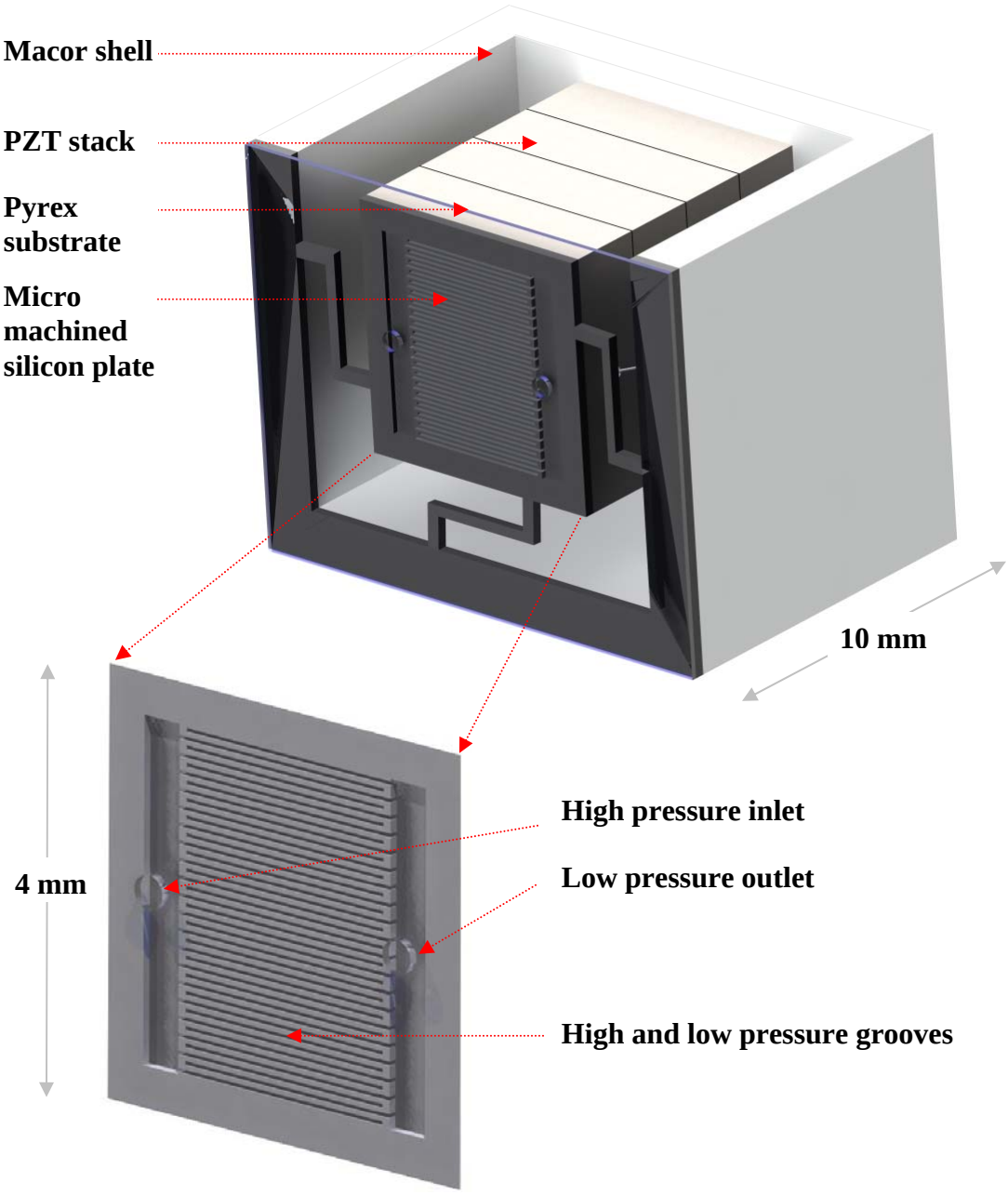

Figure 1.2: Cut away view of micro valve design showing close-up of the micro machined silicon plate

1.3 Modeling and Experimental Testing of an Active Micro Valve

The design shown in Fig. 1.2 has the potential to address the underlying performance specifications associated with the cryogenic micro valve. However, in order to optimally design the valve and characterize the prototype devices it is necessary to develop

advanced analytical and numerical models that are predictive and therefore can be compared with experimental data. This thesis describes the development of a two dimensional, detailed flow model of the valve and compares the predicted flow behavior with experimental data. Also, some structural modeling of the valve is presented in order to address key concerns associated with reliability and deformation; the structural model is compared to experimental data where possible. It is hoped that this thesis will provide a useful tool and valuable insight for future work in the micro valve design and development process.

1.4 References

Taylor, R. (2005). M.S. thesis, The University of Wisconsin, Madison, WI.

Chapter 2

INDIVIDUAL LAND AND GROOVE MODEL

2.1 Problem Discussion

The first step towards the development of a flow model of the valve is focused on characterizing the interaction of adjacent high and low pressure grooves via flow across the land. This chapter presents a flow model of a single land adjacent to a high and low pressure groove. Results will be presented in a non-dimensional form in an attempt to provide generalized flow behavior of the land and groove combination. The computational domain associated with this effort is presented in Fig. 2.1.

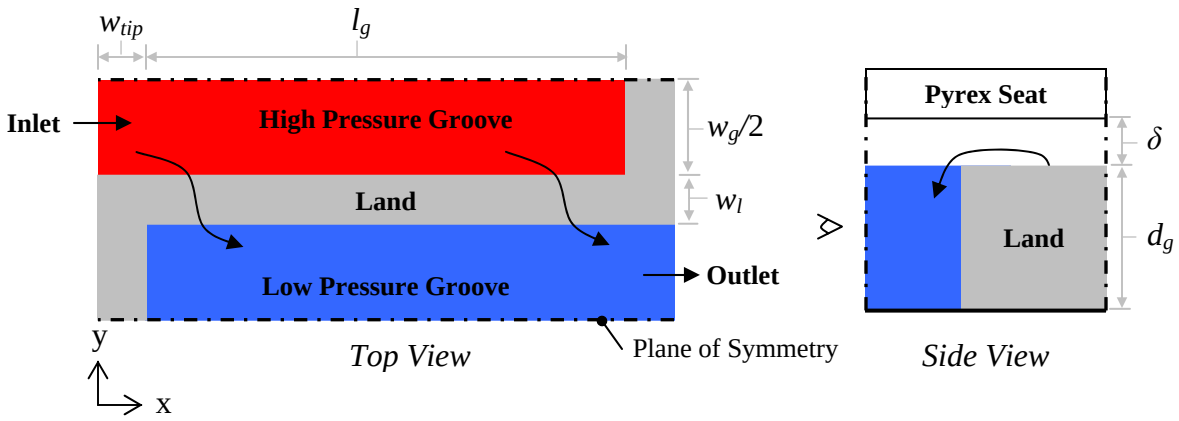

Figure 2.1: Computational domain of a single land and groove

In Fig. 2.1, w_{tip} is the width of the tip of the groove (i.e., the separation between the end of the low pressure groove and the high pressure manifold), l_g is the groove length (i.e., the length of the high pressure groove that is actually exposed, via the land, to the low pressure groove), w_g is the groove width (perpendicular to the main flow direction), w_l is the land width, d_g is the groove depth, and δ is the clearance between the land surface and the Pyrex seat.

A secondary purpose of this chapter is to investigate the effect of the two dimensionality of the flow over the land. To facilitate the two dimensional solution, the assumptions of laminar, incompressible, constant viscosity, no-slip, steady flow will be made relative to flow in both the land and grooves. However, a number of authors have investigated one dimensional flow in micro-channels, for example Arkilic et al. 2001 and Turner et al. 2004 have concluded that both compressible and slip effects can become important in micro-channel flow under some conditions. The land represents the most likely location where slip and compressible effects may be important for this application as it is characterized by the smallest dimension. The incompressible solution derived in this chapter is used to show that the two dimensionality of the flow over the land has a negligible effect on its behavior; therefore, the one dimensional results which include compressibility and slip are used to model the flow over the land in the final flow model of the valve (presented in Chapter 5).

2.2 Governing Equations for the Land

2.2.1 2-D Governing Equation for Incompressible Flow with No-Slip Conditions

The Navier-Stokes equations govern the flow across the land for the assumed laminar, incompressible, constant viscosity, no-slip, steady flow; the *x* and *y* equations are shown in Eqs. (2.1) and (2.2), according to Schuetter 2004:

$$\frac{\partial p}{\partial x} = \mu \frac{\partial^2 u}{\partial z^2} \tag{2.1}$$

$$\frac{\partial p}{\partial y} = \mu \frac{\partial^2 v}{\partial z^2} \tag{2.2}$$

where u and v are the velocities in the x and y directions, p is the local pressure, μ is the viscosity (assumed to be constant), and z is the direction perpendicular to the land. Also, dx and dy are the nodal separation distances:

$$dx = \frac{l_g}{m-1} \tag{2.3}$$

$$dy = \frac{w_l}{n-3} \tag{2.4}$$

The integration of Eqs. (2.1) and (2.2) in z, together with the application of the no-slip boundary condition at the land and the valve seat surfaces (i.e., $u = v = 0$ at $z = 0$ and $z = \delta$ where δ is the gap height) leads to a parabolic velocity distribution:

$$u = \frac{1}{2\mu}\frac{\partial p}{\partial x}\left[z^2 - z\,\delta\right] \tag{2.5}$$

$$v = \frac{1}{2\mu}\frac{\partial p}{\partial y}\left[z^2 - z\,\delta\right] \tag{2.6}$$

The bulk velocities in the x and y direction (u_m and v_m) are obtained by integrating Eqs. (2.5) and (2.6) across the gap (i.e., from $z = 0$ to $z = \delta$):

$$u_m = \frac{1}{\delta}\int_0^{\delta} u\,dz = -\gamma_s \frac{\partial p}{\partial x} \tag{2.7}$$

$$v_m = \frac{1}{\delta}\int_0^{\delta} v\,dz = -\gamma_s \frac{\partial p}{\partial y} \tag{2.8}$$

where

$$\gamma_s = \frac{\delta^2}{12\mu} \tag{2.9}$$

The bulk velocities represent the mass integrated flow over z at any x and y position in terms of the pressure gradient and allow the three-dimensional flow problem to be reduced to a two-dimensional problem in pressure (the pressure is assumed to be uniform in z, a result that can be

derived from the scale of the *z*-directed Navier-Stokes equation). A mass balance is carried out on a control volume that is differentially small in *x* and *y* but extends from the land to the seat in *z* (i.e., the element has height δ and area *dx* by *dy*). Figure 2.2 illustrates the mass terms associated with this differential control volume; the continuity equation suggested by Fig. 2.2 (using the assumption that ρ is constant) is:

$$\frac{\partial(\delta u_m)}{\partial x} + \frac{\partial(\delta v_m)}{\partial y} = 0 \tag{2.10}$$

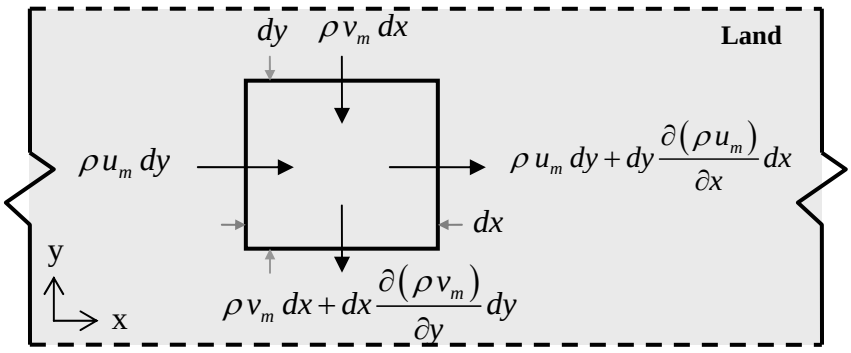

Figure 2.2: Mass terms on a differential element in the land region

Substitution of Eqs. (2.7) and (2.8) into Eq. (2.10) leads to:

$$\frac{\partial}{\partial x}\left(\delta^3 \frac{\partial p}{\partial x}\right) + \frac{\partial}{\partial y}\left(\delta^3 \frac{\partial p}{\partial y}\right) = 0 \tag{2.11}$$

For this analysis, the height, δ, is assumed to be spatially uniform (i.e., it is assumed that the top of the land and the Pyrex© valve seat are both flat and these surfaces are parallel) so that δ is constant and therefore Eq. (2.11) can be written as:

$$\frac{\partial^2 p}{\partial x^2} + \frac{\partial^2 p}{\partial y^2} = 0 \tag{2.12}$$

2.2.2 Investigation of the Incompressible and No-Slip Assumptions

The minimum dimension associated with a single land and groove is the valve seat clearance, δ, shown in Fig. 2.1. It is likely that the maximum value of the valve seat clearance will not exceed a few micrometers due to the actuation capability of the PZT stack. This is a very small length scale and therefore the use of the no-slip condition at the upper and lower surfaces is questionable. The applicability of the no-slip condition is governed by the Knudsen number, which represents the ratio of the mean free molecular path to a minimum geometric length scale, Forsythe 2003. For this application, the appropriate Knudsen number should be based on the valve seat clearance (Kn_δ):

$$Kn_\delta = \sqrt{\frac{\pi\gamma}{2}}\frac{M}{Re} \tag{2.13}$$

where γ is the ratio of specific heats for the gas or fluid flowing through the land, M is the Mach number, and Re is the Reynolds number based on the valve seat clearance, as defined below.

$$M = \frac{V}{c} \tag{2.14}$$

$$Re = \frac{\rho V \delta}{\mu} \tag{2.15}$$

where V is the local mean velocity magnitude and c is the local speed of sound in the fluid or gas. The Knudsen number as a function of the valve seat clearance is shown in Fig. 2.3 for various operating conditions assuming helium gas.

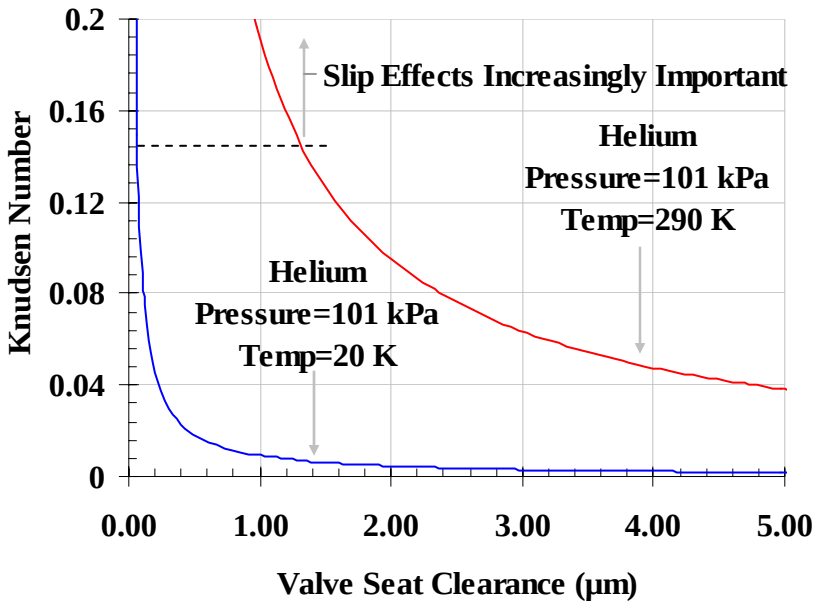

Figure 2.3: Knudsen number in the land as a function of valve seat clearance for various operating conditions with helium gas

Turner et al. 2004 has experimentally studied the effect of slip and compressibility on pressure driven (i.e., Poiseuille) micro-channel flow and observed a 50% increase in the mass flow rate with a Knudsen number of 0.15 relative to the no-slip condition result associated with a Knudsen number of approximately 0.001. Therefore, Fig. 2.3 indicates that solutions obtained using the no-slip Navier-Stokes equations derived in Section 2.2.1 are likely to significantly underestimate the solution obtained using a more appropriate Navier-Stokes equation with slip conditions; this is particularly true for room temperature helium at atmospheric pressure with valve seat clearances that are less than approximately 1.5 µm. However, at higher pressures rarefaction effects become less important. Turner also observed an 8% decrease in the mass flow rate with a Mach number of 0.35 relative to a Mach number of 0.0; this suggests that compressibility effects may be important in micro-channel flow.

Arkilic et al. 1997 also suggest that compressible effects for micro-scale Pousielle flow in a channel can be non-negligible. They derived a one-dimensional, isothermal, compressible flow equation for the mass flow rate in pressure-driven flow through parallel plates which accounts for slip conditions on the upper and lower boundaries of the channel:

$$\dot{m}' = \frac{\delta^3 P_o^2}{24 \mu L R T}\left[P_r^2 - 1 + 12 \sigma Kn_o \left(P_r - 1 \right) \right] \qquad (2.16)$$

In Eq. (2.16) $\dot{m}'$ is the mass flow rate per unit channel width, δ is the gap height, P_o is the outlet pressure, L is the channel length, R is the ideal gas constant, T is the temperature, Kn_o is the outlet Knudsen number (based on δ), σ is the tangential momentum accommodation coefficient, and P_r is the ratio of inlet pressure to the outlet pressure. For most engineering calculations σ is typical assumed to be 1.0, however values less than unity on silicon surfaces have been observed.

In order to establish the applicability of the incompressible and no-slip assumptions, the mass flow ratio (m_r) is defined as the ratio of the mass flow rate per unit flow area predicted by Eq. (2.16) (i.e., including both compressibility and slip effects and therefore denoted *S-C*) to the ratio of mass flow rate per unit flow area resulting from Eq. (2.7) in the limit of a one dimensional flow (i.e., ignoring both compressibility and slip and therefore denoted *NS-IC*). The numerator and denominator are computed by assuming equivalent inlet and exit pressures to the channel:

$$m_r = \frac{\dot{m}_{S-C}}{\dot{m}_{NS-IC}} \qquad (2.17)$$

Figure 2.4 shows a contour plot of the mass flow ratio, (m_r) in the parameter space of the gap height (δ) and pressure ratio (P_r) for room temperature helium gas with an outlet pressure of 101.0 kPa and a length, (L) of 50.0 μm. The viscosity used in Eq. (2.7) was evaluated at the average of the inlet and outlet pressure while the density in the mass flow rate calculation was

evaluated at the outlet pressure. The tangential momentum coefficient, (σ), was assumed to be 0.8.

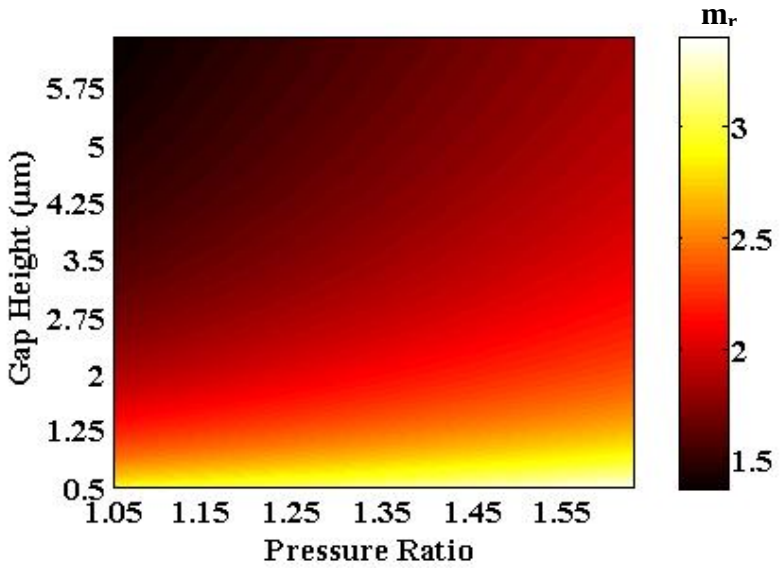

Figure 2.4: Mass flow ratio as a function of pressure ratio and clearance for one dimensional flow over the land with the set of conditions described above

Figure 2.4 shows that the incompressible no slip solution, Eq. (2.7), under-predicts the compressible slip solution for room temperature helium at high pressure ratio and small clearance. The magnitude of under-prediction is quite large. Unfortunately the compressible slip solution, Eq. (2.16), was derived for one dimensional flow and is strictly valid only for this case. However, if it can be shown that the impact of the two dimensionality of the flow within the land is not significant for this application, then Eq. (2.16) provides a more complete characterization of the pressure/flow behavior within the land than the Reynolds-type equation derived in Section 2.2.1. The subsequent sections explore the impact of two dimensional flow within the land using the incompressible, no-slip governing equations.

2.3. Governing Equations for the Groove

Flow through the grooves is assumed to be hydro dynamically fully developed; a more complete description of the flow within the grooves is obtained in Chapter 3 using computational fluid dynamics. The pressure gradient in the groove is related to the local mass flow rate ($\dot{m}$) according to:

$$\frac{dp}{dx} = -\frac{K\,\mu\,per_g^2}{32\,\rho\,A_{c,g}^3}\dot{m} \tag{2.18}$$

where p is the local pressure, μ and ρ are the viscosity and density of the gas, respectively, both of which are assumed to be constant, per_g and $A_{c,g}$ are the perimeter and cross-sectional area of the groove:

$$per_g = 2\left(d_g + w_g\right) \tag{2.19}$$

$$A_{c,g} = \left(d_g + \delta\right) w_g \tag{2.20}$$

where d_g is the groove depth, w_g is the groove width, and δ is the clearance between the land surface and the Pyrex seat. For fully developed flow, the parameter K is a constant that depends on the groove aspect ratio (α) according to Rohsenow 1998:

$$K = 24\left[1 - 1.3553\alpha + 1.9467\alpha^2 - 1.7012\alpha^3 - 0.9564\alpha^4 - 0.2537\alpha^5\right] \tag{2.21}$$

where the aspect ratio is defined as:

$$\alpha = \frac{\min\left(d_g + \delta, w_g\right)}{\max\left(d_g + \delta, w_g\right)} \tag{2.22}$$

The pressure drop due to the contraction from the high pressure groove into the land region is proportional to the kinetic energy of the fluid:

$$\Delta P = K_c \frac{\dot{m}^2}{2\,\rho\,A_o^2} \tag{2.23}$$

where A_o is the flow area associated with the land. The constant of proportionality is the inertial coefficient, K_c, and may be estimated according to White 2003 [2.7]:

$$K_c = 1 - \left(\frac{A_o}{A_i} \right)^2 \tag{2.24}$$

where A_o and A_i are the post- and pre-contraction areas perpendicular to the direction of flow. The inertial coefficient, K_c, is more rigorously investigated in Chapter three using a CFD simulation. The pressure change due to the expansion from the land region into the low pressure groove is also assumed to be proportional to the kinetic energy of the fluid and is expressed in a manner similar to Eq. (2.23), using an inertial expansion coefficient; the value of the expansion coefficient, K_e, may be estimated according to White 2003:

$$K_e = 0.42 \left(1 - \left(\frac{A_o}{A_i} \right)^2 \right) \tag{2.25}$$

2.4. Discretization of the Governing Equations

The land region and grooves are organized into m equally spaced rectangular control volumes in the x direction and n volumes in the y direction, as shown in Fig. 2.5. Subscript i,j refers to the x,y location of the mesh; $i = 0$ corresponds to the left-hand edge while $i = m$ is the right-hand edge and $j = 0$ is the low pressure groove while $j = n$ is the high pressure groove.

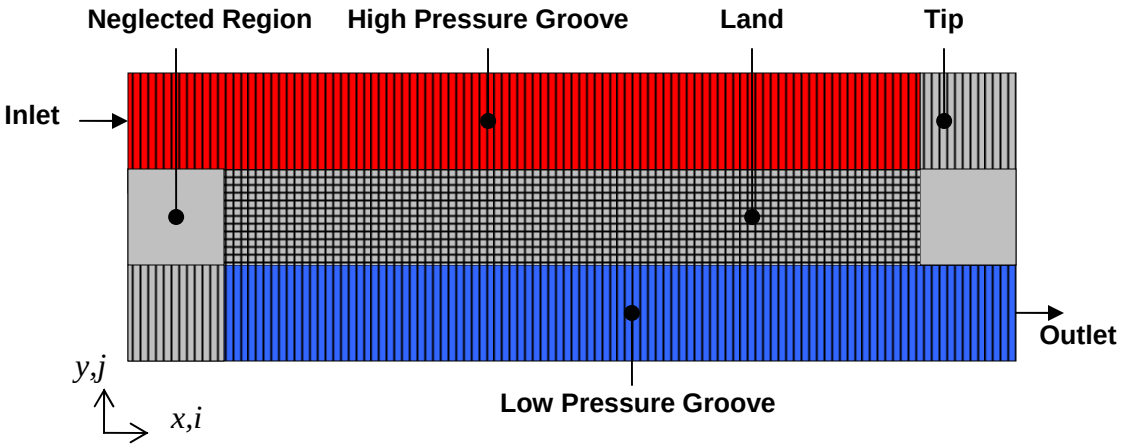

Figure 2.5: Grid mapping scheme for the numerical simulation of a single land and groove

Solution of the discretized form of the governing equations will be accomplished by using an iterative relaxation process with sparse matrix decomposition in the MATLAB© environment, Incropera et. al 2001.

2.4.1 Groove Discretization

Discretization of the governing equations for the grooves is accomplished through a mass balance on a control volume, as shown in Fig. 2.6 for the high pressure groove.

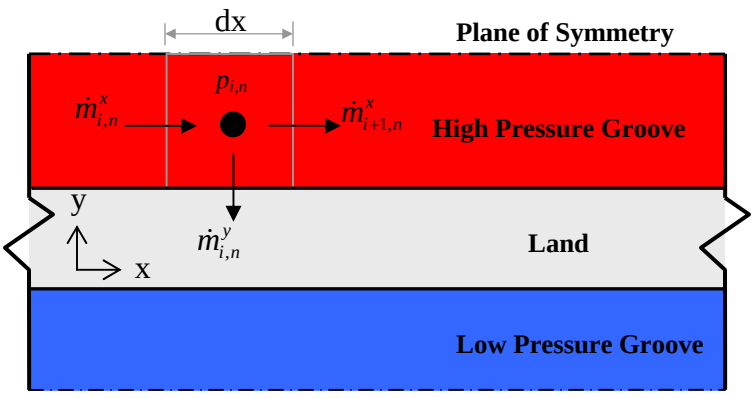

Figure 2.6: Mass balance for the high pressure groove

The flow along the groove ($\dot{m}_{i,n}^{x}$) is related to the pressure gradient according to Eq. (2.18); a 1st order approximation of the pressure gradient leads to:

$$\dot{m}_{i,n}^{x} = \frac{32\,\rho\,A_{c,g}^{3}}{K\,\mu\,per_{g}^{2}}\frac{p_{i-1,n} - p_{i,n}}{dx} \tag{2.26}$$

The flow into the land ($\dot{m}_{i,n}^{y}$) occurs across the land lip and therefore is related to the inertial pressure loss. The inertial pressure loss is assumed to occur over a negligible distance and therefore occurs between nodes *i,n* and *i,n*-1. Equation (2.23) written for node *i* is therefore:

$$\dot{m}_{i,n}^{y} = \sqrt{\left(p_{i,n} - p_{i,n-1}\right)\frac{2\,\rho\,A_{L}^{2}}{K_{c}}} \tag{2.27}$$

The mass balance of Fig. 2.6 yields the following:

$$\dot{m}_{i,n}^{x} = \dot{m}_{i+1,n}^{x} + \dot{m}_{i,n}^{y} \tag{2.28}$$

Equations (2.26) and (2.27) are substituted into Eq. (2.28), rearranging yields:

$$\left(p_{i-1,n} - p_{i,n}\right)\left(\beta_{g}\right) = \left(p_{i,n} - p_{i+1,n}\right)\left(\beta_{g}\right) + \sqrt{\left(p_{i,n} - p_{i,n-1}\right)\left(\frac{2\rho A_{o}^{2}}{K_{c}}\right)} \tag{2.29}$$

where:

$$\beta_{g} = \frac{16\,\rho\,A_{c,g}^{3}}{K\,\mu\,per_{g}^{2}dx} \tag{2.30}$$

The area A_o is the area associated with the interface between the groove and the land within the control volume; the area is normal to the *y*-direction vector and has width *dx* and height δ. The constant K_c is the inertial contraction coefficient.

The non-linear Eq. (2.29) is linearized, as shown in Eq. (2.31).

$$\left(p_{i-1,n} - p_{i,n}\right)\left(\beta_{g}\right) = \left(p_{i,n} - p_{i+1,n}\right)\left(\beta_{g}\right) + \left(p_{i,n} - p_{i,n-1}\right)\left(C_{i,n}\right) \tag{2.31}$$

where, $C_{i,n}$ depends on the pressures and is evaluated using in an iterative, successive substitution relaxation process:

$$C_{i,n} = \sqrt{\frac{2\rho A_L^2}{\left(p^*_{i,n} - p^*_{i,n-1}\right) K_c}} \tag{2.32}$$

In Eq. (2.32), the superscript (*) denotes the solution from the previous iteration. Convergence is assumed to occur when the maximum difference between the linearized inertial mass flow rate, $\dot{m}_{est}$ shown in Eq. (2.33), and the actual inertial mass flow rate, shown in Eq. (2.27), falls below the relative value of 10^{-5}.

$$\dot{m}_{est} = \left(p_{i,n} - p_{i,n-1}\right) C_{i,n} \tag{2.33}$$

Collection of like terms in Eq. (2.31) yields the final linearized form:

$$p_{i+1,n}\left(\beta_g\right) + p_{i-1,n}\left(\beta_g\right) + p_{i,n-1}\left(C_{i,n}\right) - p_{i,n}\left(2\beta_g + C_{i,n}\right) = 0 \qquad \text{for } i = 1..(m-1) \tag{2.34}$$

The discretized form of the governing equation for a control volume in the low pressure groove is equivalent to Eq. (2.34) but written for nodes *i*,0 and *i*,1.

The definition of the inlet and exit boundary conditions for the grooves, at nodes (0,*n*) and (*m*,0), is accomplished by applying continuity to node (*0*,*n*), as shown in Fig. 2.7.

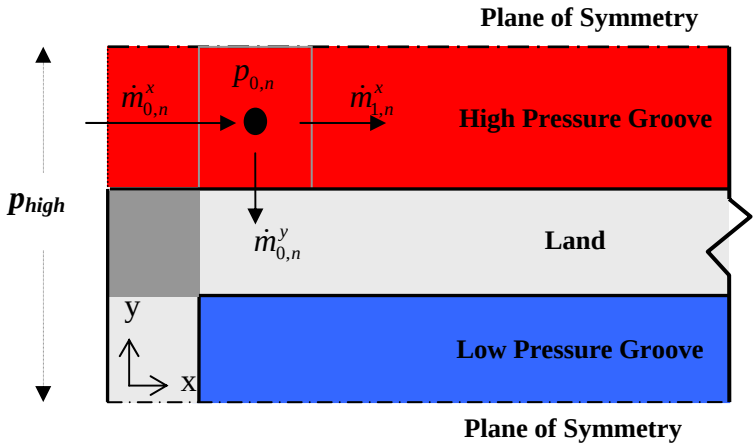

Figure 2.7: Mass balance for the high pressure groove entrance

The flow along the groove and into the land is evaluated using Eqs. (2.26) and (2.27), substitution of their definition into the mass balance shown in Fig. 2.7 leads to:

$$\dot{m}^x_{0,n} = \left(p_{0,n} - p_{1,n}\right)\left(\beta_g\right) + \left(p_{0,n} - p_{0,n-1}\right)\left(C_{0,n}\right) \tag{2.35}$$

The pressure drop from p_{high} to $p_{0,n}$ is assumed to occur due to viscous losses through the tip width in the high pressure groove and an inertial entrance loss:

$$p_{high} - p_{0,n} = \left(\frac{1}{\beta_{g,tup}}\right)\dot{m}^x_{0,n} + \left(\frac{2K_{c,g}}{\rho A^2_{c,g}}\right)\dot{m}^{x\ 2}_{0,n} \tag{2.36}$$

Equation (2.36) is linearized in the following manner:

$$p_{high} - p_{0,n} = \frac{\dot{m}^x_{0,n}}{\beta_{g,tip}} + C_{hg}\,\dot{m}^x_{0,n} \tag{2.37}$$

Rearranging leads to:

$$\dot{m}^x_{0,n} = \frac{p_{high} - p_{0,n}}{\dfrac{1}{\beta_{g,tip}} + C_{hg}} \tag{2.38}$$

The constant C_{hg} is evaluated in an iterative process:

$$C_{hg} = \frac{\left(p^*_{high} - p^*_{0,n}\right)}{\dot{m}^*} - \frac{1}{\beta_{g,tip}} \tag{2.39}$$

where:

$$\dot{m}^* = \frac{-\psi + \sqrt{\psi^2 + 4\eta\left(p^*_{high} - p^*_{0,n}\right)}}{2\eta} \tag{2.40}$$

$$\psi = \frac{1}{\beta_{g-tip}} \tag{2.41}$$

$$\eta = \frac{2K_{c-g}}{\rho A^2_{c,g}} \tag{2.42}$$

$$\beta_{g,tip} = \frac{16\,\rho\,A^3_{c,g}}{K\,\mu\,per_g^2\left(\frac{dx}{2} + w_{tip}\right)} \tag{2.43}$$

The subscript (*) represents the previous iterative solution. The constant K_{c-g} represents the inertial contraction coefficient for entrance into the high pressure groove, which can be estimated according to:

$$K_{c-g} = 1 - \left(\frac{A_{c,g}}{2\,h_g\left(w_l + w_g\right)}\right)^2 \tag{2.44}$$

Substitution of Eq. (2.38) into Eq. (2.35) results in the final linearized form:

$$0 = -p_{high}\left(\frac{1}{\beta_{g,tip}} + C_{hg}\right)^{-1} + p_{0,n}\left(\beta_g + C_{0,n} + \left(\frac{1}{\beta_{g,tip}} + C_{hg}\right)^{-1}\right) - p_{1,n}\left(\beta_g\right) - \left(C_{0,n}\right)p_{0,n-1} \tag{2.45}$$

The governing equations for the control volume (m,0) in the low pressure groove follow a similar form.

Definition of the boundary conditions for the groove ends (i.e., at nodes m,n and 0,0), is accomplished by applying continuity to these nodes, as shown in Fig. 2.8 for node m,n.

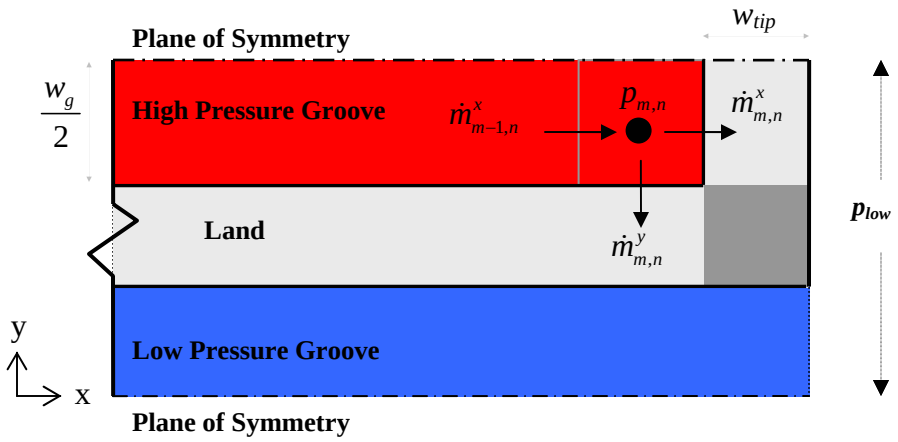

Figure 2.8: Mass balance for the high pressure groove end

Continuity is applied to control volume in Fig. 2.8, which results in Eq. (2.46):

$$\left(p_{m-1,n} - p_{m,n}\right)\left(\beta_g\right) = \dot{m}^x_{m,n} + \left(p_{m,n} - p_{m,n-1}\right)\left(C_{m,n}\right) \tag{2.46}$$

The pressure drop from $p_{m,n}$ to p_{low} is related to the combination of the viscous losses occurring through the width of the tip as well as an inertial loss due to contraction and expansion; therefore, the term $\dot{m}^x_{m,n}$ is given by:

$$p_{m,n} - p_{low} = \left(\frac{w_{tip}}{\gamma_s}\right)\frac{2\dot{m}^x_{m,n}}{\rho\,\delta\,w_g} + \frac{2\left(K_c + K_e\right)}{\rho\,\delta^2\,w_g^2}\dot{m}^{x\ 2}_{m,n} \tag{2.47}$$

Equation (2.47) is linearized in a process equivalent to that described in Eqs. (2.36) through (2.42). The governing equations for the control volume (0,0) in the low pressure groove follows an equivalent form as demonstrated above.

2.4.2 Land Discretization

Equation (2.12) which governs the flow over the land region is discretized using a second order central difference approximation:

$$p_{i,j}\left[-\frac{2}{dx^2}-\frac{2}{dy^2}\right]+p_{i+1,j}\frac{1}{dx^2}+p_{i-1,j}\frac{1}{dx^2}+p_{i,j+1}\frac{1}{dx^2}+p_{i,j-1}\frac{1}{dx^2}=0 \quad (2.48)$$

$$\text{for } i=1..(m-1) \quad j=1..(n-1)$$

The left and right boundaries of the land assume a zero flow condition which, when combined with a first order approximation of Eq. (2.7), leads to the following:

$$p_{1,j}=p_{0,j} \quad \text{for } j=1..(n-1) \quad (2.49)$$

$$p_{m-1,j}=p_{m,j} \quad \text{for } j=1..(n-1) \quad (2.50)$$

Discretization of the upper boundary on the land is accomplished by applying continuity a node on the boundary *i,n*, as shown in Fig. 2.9.

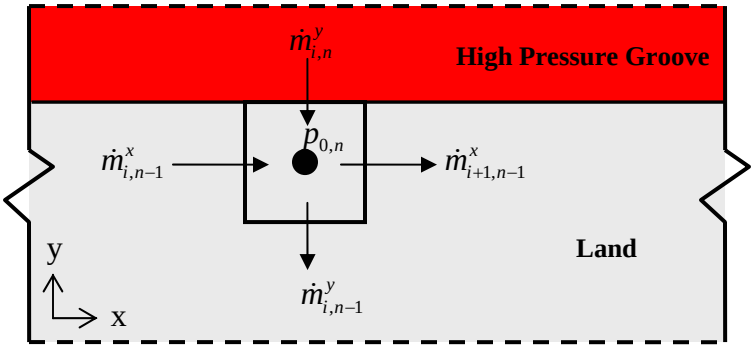

Figure 2.9: Mass balance for the upper boundary of the land

The term $\dot{m}^x_{i,n-1}$ is evaluated using a first order approximation of the pressure gradient:

$$\dot{m}^x_{i,n-1}=\gamma_s\,\rho\,dy\,\delta\frac{p_{i-1,n-1}-p_{i,n-1}}{dx} \quad (2.51)$$

The term $\dot{m}^y_{i,n-1}$ is also evaluated using a first order approximation of the pressure gradient:

$$\dot{m}^y_{i,n-1}=\gamma_s\,\rho\,dx\,\delta\frac{p_{i,n-1}-p_{i,n-2}}{dy} \quad (2.52)$$

The term $\dot{m}^y_{i,n}$ was previously derived in Eq. (2.27). Substitution of Eqs. (2.51), (2.52), and (2.27) into the mass balance shown Fig. 2.9 yields:

$$\left(p_{i-1,j}-p_{i,j}\right)\left(\gamma_s\frac{dy}{dx}\right)+\left(p_{i+1,j}-p_{i,j}\right)\left(\gamma_s\frac{dy}{dx}\right)+\left(p_{i,j-1}-p_{i,j}\right)\left(\gamma_s\frac{dx}{dy}\right)+\left(p_{i,j+1}-p_{i,j}\right)\left(C_{i,j+1}\right)=0$$

(2.53)

Collecting like terms we obtain the final linearized form:

$$p_{i-1,n-1}\left(\gamma_s\frac{dy}{dx}\right)+p_{i+1,n-1}\left(\gamma_s\frac{dy}{dx}\right)+p_{i,n-2}\left(\gamma_s\frac{dx}{dy}\right)+p_{i,n}\left(C_{i,n}\right)-p_{i,n-1}\left(\gamma_s\frac{dy}{dx}+\gamma_s\frac{dx}{dy}+C_{i,n}\right)=0$$

$$\text{for } i=1..(m-1)$$

(2.54)

The governing equation for a control volume in the land region adjacent to the low pressure groove, (j=2), follows a similar form as Eq. (2.54).

2.4.3 Incompressible No-Slip Two Dimensional Results

The Matlab code of the incompressible two dimensional model which has been developed in the preceding sections can be found in Appendix A. In an attempt to demonstrate typical flow behavior, sample results of the model output will be presented in this section. However, before results of the model can be presented, adequate values for the node numbers, m and n must be determined. A simple method for determining values for m and n is to run the model parametrically for different values of m and n while recording the output mass flow rate. Once convergence in the mass flow rate has been detected then adequate values of m and n have been reached. Figure 2.10 demonstrates the results of this analysis method for the dimensions, properties, and conditions, shown in Table 2.1.

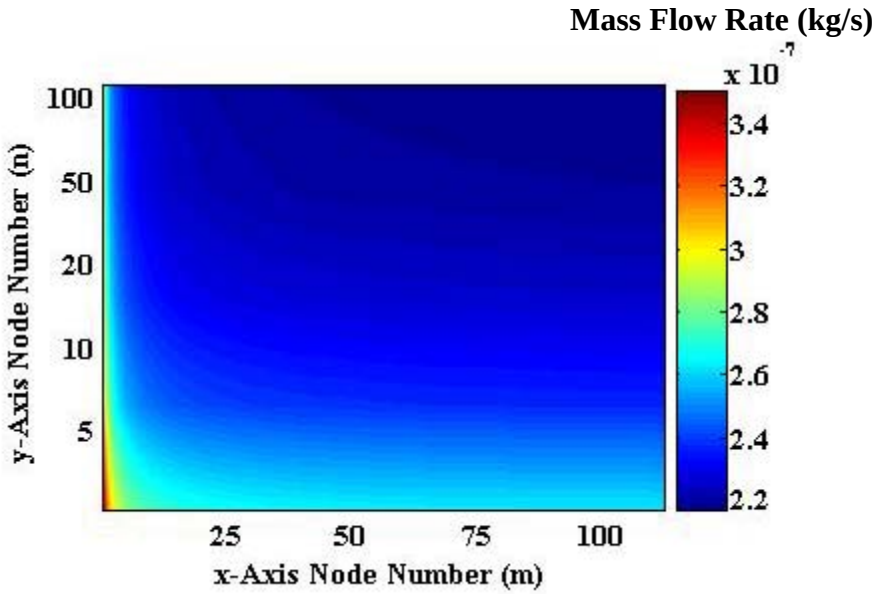

Figure 2.10: *x* and *y* axis node number analysis, for the dimensions, properties, and conditions shown in Table 2.1

Table 2.1: Variables used to generate Fig. 2.10

Variable	Value	
δ	3.0	µm
d_q, w_q	100.0	µm
w_l ,w_{tip}	50.0	µm
l_q	2800	µm
P_{high}	100.0	kPa
P_{low}	0.0	kPa
ρ	0.5	kg/m^3
μ	2.0e-5	kg-s/m

From Fig. 2.10 we can see that approximate values of m=75.0 and n=50.0 would be acceptable, as convergence in the mass flow rate has occurred. Figures 2.11 through 2.12 illustrate typical distributions of the mean *x*-velocity, mean *y*-velocity, and pressure over the land for the properties, dimensions, and conditions from Table 2.2 with m=75.0 and n=50.0.

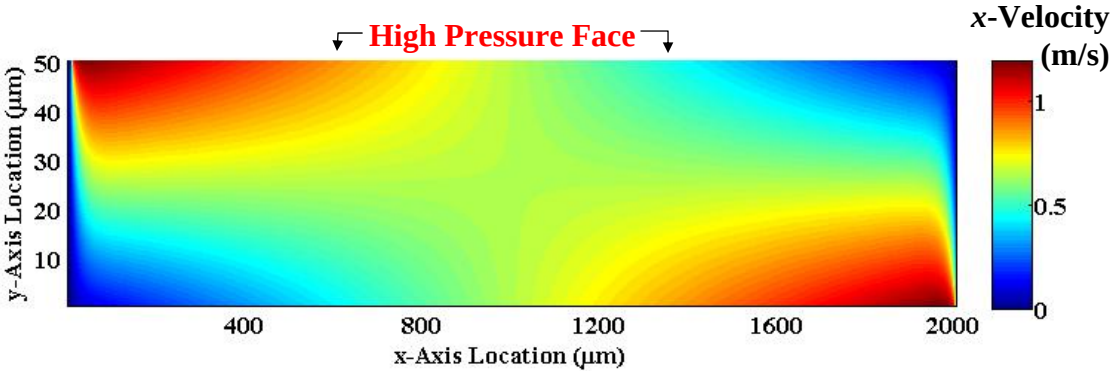

Figure 2.11: *x*-Axis velocity over the land for the properties, dimensions and conditions, shown in Table 2.2

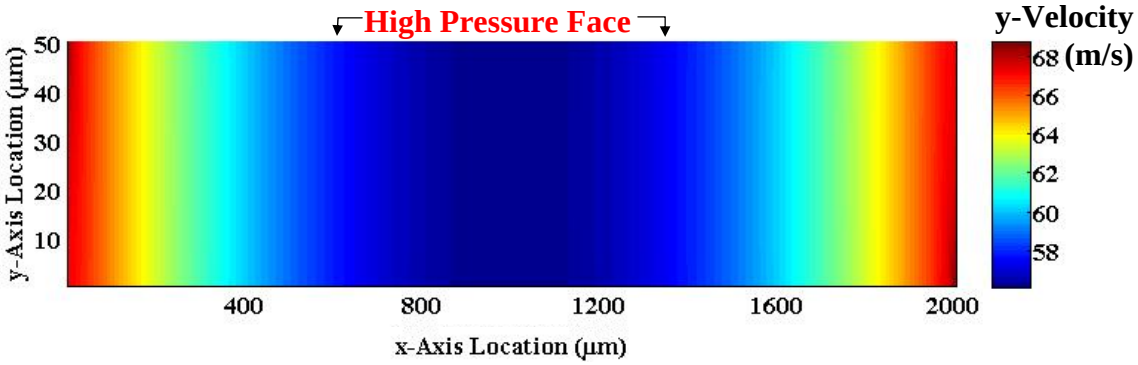

Figure 2.12: *y*-Axis velocity over the land for the properties, dimensions and conditions, shown in Table 2.2

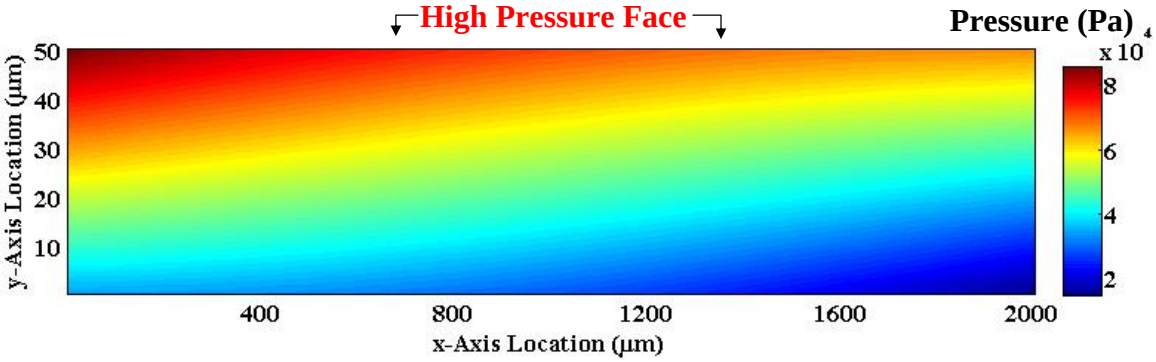

Figure 2.13: Pressure in the land for the properties, dimensions and conditions, shown in Table 2.2

Table 2.2: Variables used for Figs. 2.11-2.13

Variable	Value	
δ	4.0	µm
d_g, w_g, w_l ,w_{tip}	50.0	µm
l_g	2000	µm

Table 2.2 cont.		
P_{high}	100.0	kPa
P_{low}	0.0	kPa
ρ	0.5	kg/m^3
μ	2.0e-5	kg-s/m

The solution for Figs. 2.11 through 2.13 represents a case where the total pressure drop occurs as a combination of pressure loss in the land and the grooves. Despite the two dimensional nature of the pressure distribution seen in Fig. 2.13, the *x*-axis velocity magnitude in Fig. 2.11 is much less than the *y*-axis velocity magnitude in Fig. 2.12. This fact combined with large difference in length scale for the *x* and *y* axes, suggests that flow over the land is primarily one-dimensional (i.e., the flow at any *x*-location is primarily in the *y*-direction), as we will see in following sections.

2.5 Governing Non-Dimensional Numbers

From both a computational and conceptual standpoint, it is desirable to reduce the large number of variables that define the single land and groove model to obtain a smaller set of important non-dimensional numbers that governs a non-dimensional mass flow rate. The non-dimensional mass flow rate, $\bar{\dot{m}}$, is defined as the ratio of the actual mass flow rate for a given valve geometry ($\dot{m}$) to a characteristic mass flow rate ($\dot{m}_{characteristic}$).

$$\bar{\dot{m}} = \frac{\dot{m}}{\dot{m}_{characteristic}} \tag{2.55}$$

A physically meaningful characteristic mass flow rate is defined as the mass flow rate that would result if the pressure gradient in the groove and inertial losses at the groove/land interfaces were negligible:

$$\dot{m}_{characteristic} = \frac{\left(P_{high} - P_{low}\right)\delta^3 l_g \rho}{12 \mu w_l} \tag{2.56}$$

where P_{high} is the inlet pressure, P_{low} is the outlet pressure, δ is the valve seat clearance, μ is the viscosity, w_l is the land width, l_g is the groove length, and ρ is the average density. Equation (2.56) neglects the inertial pressure loss over the land and flow over the tip and therefore it will over-predict the mass flow rate relative to any real valve configuration.

It was found that two key non-dimensional numbers were sufficient to adequately correlate the flow over the land-groove interface; this set is not comprehensive but the other non-dimensional numbers were found to have a small effect on the flow under the conditions of interest. The first non-dimensional number (Re_{land}) represents the ratio of inertial to viscous pressure loss over the land:

$$Re_{land} = \frac{\Delta P_{inertial}}{\Delta P_{viscous}} \tag{2.57}$$

where:

$$\Delta P_{inertial} \propto \rho V^2 \tag{2.58}$$

$$\Delta P_{viscous} \propto \frac{\mu\ w_l\ V}{\delta^2} \tag{2.59}$$

The variable, V, is defined as the mean velocity of the gas over the land that would be associated with the previously defined characteristic mass flow rate

$$V = \frac{\dot{m}_{characteristic}}{\rho l_g \delta} \tag{2.60}$$

Substituting Eq. (2.60) into Eq. (2.57) leads to:

$$Re_{land} = \frac{(P_{high} - P_{low})\delta^4 \rho}{\mu^2 w_l^{\ 2}} \tag{2.61}$$

Note that the Reynolds number depends on the operating conditions (i.e., the applied pressures, density, and viscosity) as well as on the geometry. The second non-dimensional number (F_{geom}) is a function only of valve geometry and not of the operating conditions. F_{geom} is defined as the ratio of the pressure drop in the groove (assuming that it carries the characteristic mass flow rate across its entire length) to the total pressure drop across the valve.

$$F_{geom} = \frac{l_g \; K \; \mu \; per_g^2 \; \dot{m}_{characteristic}}{\rho \; A_g^3 \; (P_{high} - P_{low})} \tag{2.62}$$

Substituting Eq. (2.56) into Eq. (2.62) yields:

$$F_{geom} = \frac{l_g^2 \; K \; per_g^2 \; \delta^3}{w_l \; A_{c,g}^2} \tag{2.63}$$

One objective of the non-dimensional analysis is to provide a simple calculation tool (e.g., a design chart or a curve fit) that will allow quick estimates of the mass flow rate for a given valve configuration without requiring that the full, two dimensional numerical model be run for each valve/land set in a valve that might include 100's of such features. The degree to which this objective can be achieved is related to how well the non-dimensional mass flow rate collapses onto a single curve when it is expressed in terms of Re_{land} or F_{geom} (with the other independent dimensionless variable fixed). In order to obtain such dimensionless curves it was necessary to use the detailed numerical model of the flow through the valve (described above) to generate a large number of predicted results; that is, the detailed model was run many times in a stochastic fashion and the results were subsequently analyzed to verify that the predicted dimensionless mass flow rate was adequately correlated with the two independent dimensionless parameters.

The method of obtaining these simulation predictions was to fix the geometry factor, F_{geom}, while varying the Reynolds number. Each of the input variables (e.g., groove width, land height, etc.) was allowed to vary randomly over a set range with the exception of the groove length; the groove length was always re-calculated in order to maintain a fixed value of the F_{geom}. Helium at room temperature and pressure was assumed to be the working fluid for these simulations. Once a sufficient number of simulations had been run for a fixed value of F_{geom}, the dimensionless mass flow rate was plotted as a function of Re_{land}, as shown in Fig. 2.14 for various values of F_{geom}.

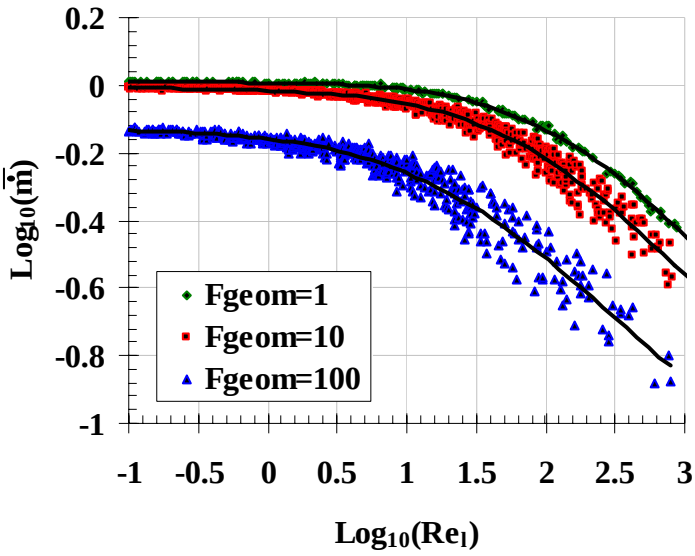

Figure 2.14: Dimensionless mass flow rate as a function of Re_{land} for various values of F_{geom}.

Figure 2.14 shows that the "data" collapse more completely onto a single curve as Re_l and F_{geom} are reduced. Note that a decreasing F_{geom} value represents a decreasing percentage of the total pressure drop occurring in the grooves. Therefore we might hypothesize that we are accurately capturing the behavior of a single land and groove which is governed entirely by the land. However, Fig. 2.14 also suggests that the behavior of the land and groove which is not governed

by the land, a configuration which is controlled by a combination of groove and land losses, is not being fully characterized by the non-dimensional numbers described above.

For a given valve design, all geometric variables except for the valve seat clearance (which is varied by the actuator) will remain fixed during operation. For a fixed geometry, the resistance to flow resulting from the grooves will remain fixed, while only the resistance to flow from the land will vary. Plotting $\bar{\dot{m}}$ as a function of Re_l for a fixed geometry while allowing the pressure drop, density, and viscosity to vary, reveals that the "data" collapse to a smooth curve. Shown in Fig. 2.15 is $\bar{\dot{m}}$ as a function of Re_l for δ=5.0 μm, d_g=115.0 μm, w_g=100.0 μm, w_l =50.0 μm, l_g=2800 μm, no-slip, and F_{geom}=30.0.

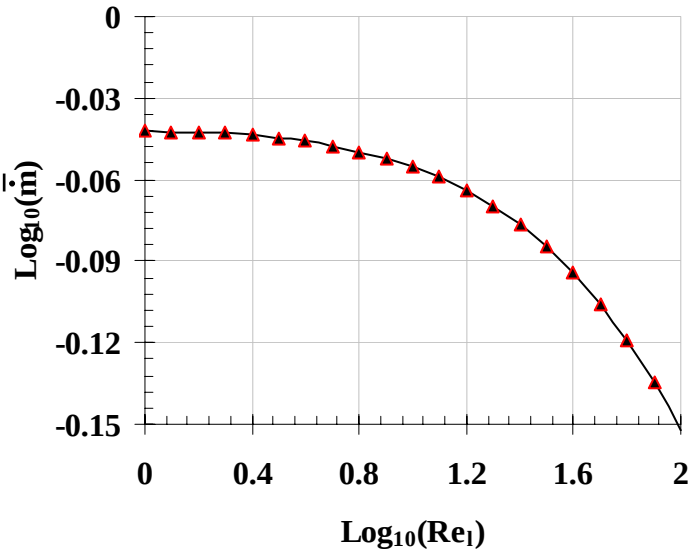

Figure 2.15: Dimensionless mass flow rate as a function of Re_l using the fixed geometry described above.

Definition of the non-dimensional curves, as demonstrated in Fig. 2.15, for a given valve design allows quick calculations of the mass flow rate in a single land and groove for any given valve seat clearance, boundary conditions, and fluid or gas. Figure 2.15 reaffirms the hypothesis that

the viscous and also the inertial land behavior is represented by using the non-dimensional numbers Re_l, $\bar{\dot{m}}$, and F_{geom}.

One useful aspect of the non-dimensional numbers developed in the preceding discussion is their application toward experimental testing. For a given design, we may want to understand the operation of the valve under cryogenic conditions but we may be limited to a room temperature environment (due to structural or other constraints). Under such a scenario, we could use the dimensionless numbers developed above to determine suitable room temperature testing conditions that are dimensionally similar to a cryogenic testing environment. Inspection of F_{geom}, Eq. (2.63), reveals that it is purely geometry based, therefore similarity in regard to experimental testing is automatically achieved if the same valve is used for both tests and it is only necessary to maintain similarity in Re_l, Eq. (2.61).

For example, in a case, with δ=6.6 μm and w_l=100 μm, where the behavior of the valve operation subjected to cryogenic helium conditions and properties would like to be understood, experimental data using alternative room temperature gases to achieve dimensionless similitude can be obtained. For this example Sulfur Hexaflouride, a gas which can have similar properties as cryogenic helium can be used. Shown in Fig. 2.16 is the land Reynolds number, Re_l, as a function of the average operating pressure where the fluid properties are evaluated, for various values of the pressure difference using room temperature sulfur hexafluoride and cryogenic helium.

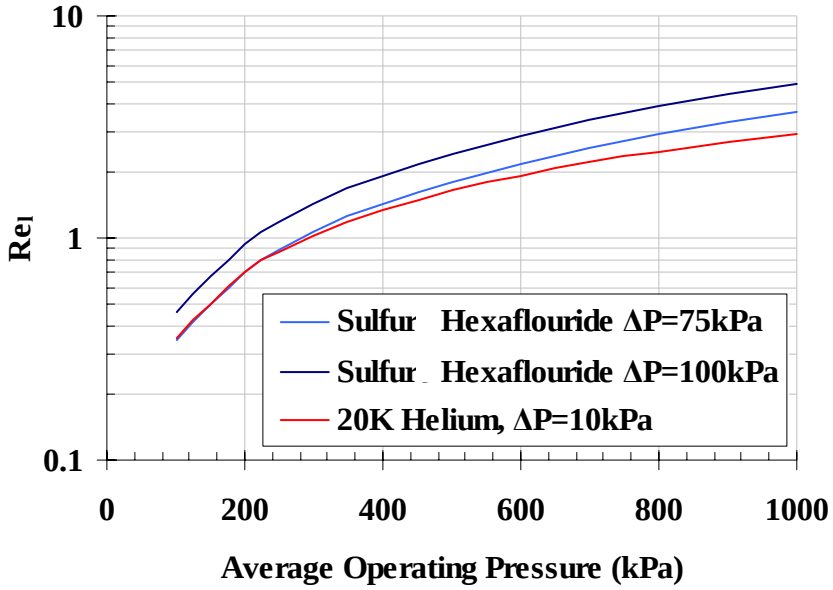

Figure 2.16: Land Reynolds number as a function of average operating pressure for room temperature sulfur hexafluoride and cryogenic helium, for various values of the total pressure drop, ΔP.

From Fig. 2.16 we can see that it would be possible to achieve dimensionless similarity between sulfur hexafluoride and cryogenic helium by varying the pressure drop across the valve for sulfur hexafluoride. This information allows one to determine the characteristics of the valve performance under cryogenic conditions simply by using room temperature sulfur hexafluoride at a different pressure differential

2.6 One and Two Dimensional Comparison

One purpose of this modeling effort is to investigate the effect of the two-dimensionality of the flow over the land. A one dimensional model would neglect all flow in the *x*-axis direction, see Fig. 2.2. Equation (2.12) would become:

$$\frac{\partial^2 p}{\partial y^2} = 0 \qquad (2.64)$$

Equation (2.64) is applied to the discretization process described in section 2.4 to produce the one dimensional model. A comparison between the one and two dimensional model is shown in Fig. 2.17 for F_{geom}=30.0.

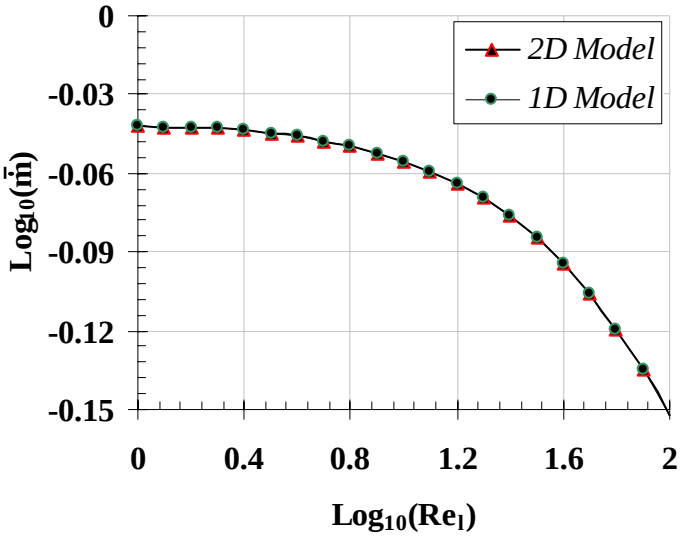

Figure 2.17: Dimensionless mass flow rate as a function of Re_l for one and two dimensional flow over the land, F_{geom}=30.0.

Figure 2.17 demonstrates that a model which assumes one dimensional flow over the land produces near equivalent results, relative error <<1%, when compared to a model which assumes two dimensional flow over the land. As mentioned in section 2.4.3 this result occurs because of the great difference in length scale between the land width and groove length. The direction of flow is primarily directly perpendicular to the groove axes, as demonstrated in Figs. 2.11 and 2.12. Any change in pressure in the *x*-axis direction is governed by the grooves and therefore accounting for a pressure difference in the x-axis direction in the land has little effect on the model results. The one dimensional model nevertheless always underestimates $\bar{\dot{m}}$ when compared to the two dimensional flow model. However the magnitude of the one dimensional model's under prediction remains, as a percent error <<1%, for a very wide range of Re_l and F_{geom}. Therefore we can assume that two dimensional effects over the land are negligible

because we can produce equivalent modeling results by not accounting for flow in the *x*-axis direction when compared to a model which does account for two dimensional flow.

Despite the detail of the models described in this chapter, there are a number of inherent assumptions which may affect the validity of the models described above. Namely, the inertial pressure loss due to flow entering and exiting the valve was characterized by the simple contraction coefficient of Eq. (2.24). A more detailed three dimensional model will be required to better understand the actual flow field occurring in the land and groove. A model of this type will be developed in the following chapters to better understand the land and groove flow field.

2.7 References

Arkilic, E. B., M. A. Schmidt, and K. S. Breuer (2001). J. *Fluid Mech.,* 437**,** p. 29.

Arkilic, E. B., M. A. Schmidt, and K. S. Breuer (1997). J. *Microelectr. Syst.,* 6**,** p. 167.

Forsythe, W.E. (1954;2003). Smithsonian Physical Tables (9th Revised Edition). Knovel.

Incropera, F., Dewitt, D., *Fundamentals of Heat and Mass Transfer, 5th Edition,* John Wiley & Sons, (2001).

Rohsenow, W.M., J. P. Hartnett, and Y. I. Cho, *Handbook of Heat Transfer, 3rd Edition,* McGraw-Hill, New York, NY, pp. 5.68, (1998).

Scheutter, S. (2004). M.S. thesis, The University of Wisconsin, Madison, WI.

Turner, S., Lam, L., Faghri, M. (2004), *J. Heat Transfer*, 126, p. 754

White, F. (2003). Fluid Mechanics, McGraw-Hill, New York

Chapter 3

Three Dimensional Modeling and Correlation of a Single Land-Groove and Manifold

3.1 Problem Discussion

The incompressible model developed in chapter two required assumptions regarding the flow field in a single land and groove. This chapter relaxes these assumptions and uses CFD modeling to provide a more predictive model of the valve.

The first objective of this chapter is to investigate the incompressible no-slip flow behavior of a single land and groove by using a more complicated three dimensional numerical simulation; specifically focusing on the flow behavior of the grooves and flow entrance into the land. The length scales associated with the grooves allow the assumptions of laminar, incompressible, constant viscosity, no-slip, and steady flow to be made. If a large difference between the three dimensional model developed in this chapter and the incompressible, no-slip model developed in chapter two is observed, then suitable correlations for friction factor and head loss will be developed using the results more complicated three dimensional numerical model; these correlations can be integrated with simpler models to provide computational efficiency and accuracy.

The second objective of this chapter is the development of a three dimensional numerical simulation of the flow field in the manifolds. The manifolds have the important role of supplying the high pressure grooves with flow from the valve inlet and to collect flow from the low pressure groove exits to the valve exit. The length scales associated with the manifolds

allow the assumptions of laminar, incompressible, constant viscosity, no-slip, and steady flow to be made. Correlations of the manifold behavior will also be obtained from the three dimensional numerical simulation and incorporated into more simple and computationally efficient models.

3.2 Land and Groove Modeling

A three dimensional, laminar, incompressible, constant viscosity model of a single land and groove has been developed using Fluent© and Gambit©. The great disparity in length scales associated with the land and groove require that a staggered grid be used to define the land and groove geometry. The mesh software Gambit© was used to develop a mesh which conforms to the land and groove geometry, as shown in Fig. 3.1.

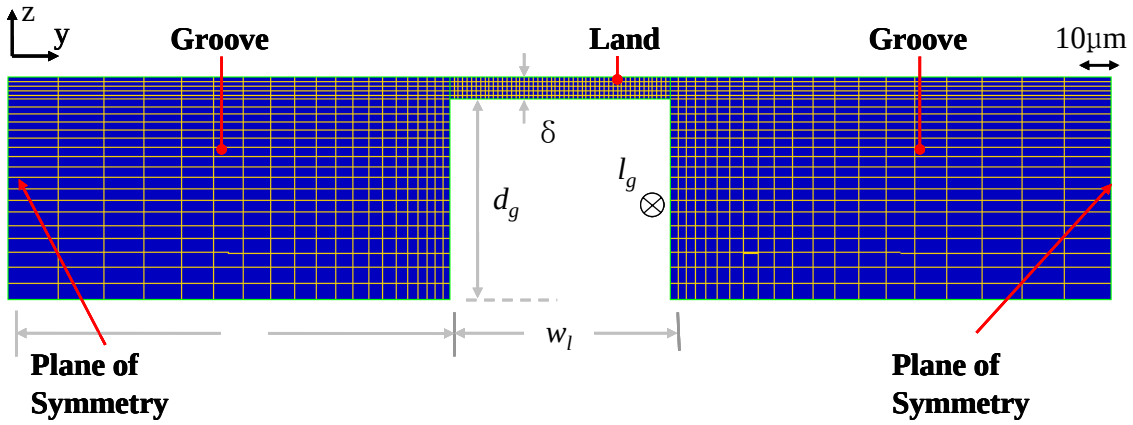

Figure 3.1: Mesh used in the three dimensional Fluent© model of a single land and groove

In Fig. 3.1, w_g is the width of a full groove (only a half-groove is modeled), d_g is the groove depth, l_g is the groove length (perpendicular to the plane of view), δ is the valve seat clearance, and w_l is the land width. The mesh shown in Fig. 3.1 uses hexagon control volumes to define the land and groove geometry. Symmetry boundary conditions were chosen to represent the centerlines of the high and low pressure groove, as shown in Fig. 3.1. A uniform mass flow entrance is used to represent for the high pressure groove inlet face and a constant pressure outlet

is used to represent the low pressure groove outlet face. All other faces were chosen to have a wall boundary condition.

A study of the mesh resolution was required to obtain an accurate model. The grid spacing of the mesh shown in Fig. 3.1 was varied for a constant set of boundary conditions and geometry. The resulting area averaged inlet pressure was recorded and plotted in order to determine when convergence had been reached. The geometry, conditions, and properties chosen for the mesh study are summarized in Table 3.1.

Table 3.1: Mesh study variables

Variable	Value
l_g	2000.0 μm
d_g	50.0 μm
w_g	200.0 μm
δ	5.0 μm
w_l	50.0 μm
μ	2.0e-5 kg-m/s
ρ	0.5 kg/m^3
$\dot{m}_i$	0.5e-6 kg/s
P_{outlet}	0.0 kPa

The equally spaced z-axis nodal spacing in the land was varied while maintaining other grid spacing in Fig. 3.1 constant, as shown in Fig. 3.2.

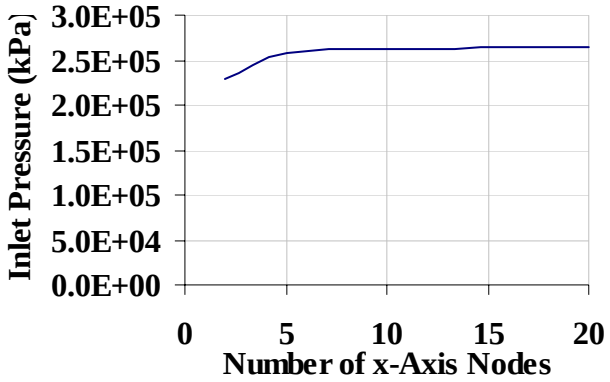

Figure 3.2: Inlet pressure as a function of z-axis nodes in the land

From Fig. 3.2 we can see that approximately five nodes in the z-axis direction will produce convergence for the inlet pressure. With five equally spaced nodes in the z-axis direction for the land, the number equally spaced nodes in the x-axis direction for the grooves and land were varied using the variables from Table 3.1.

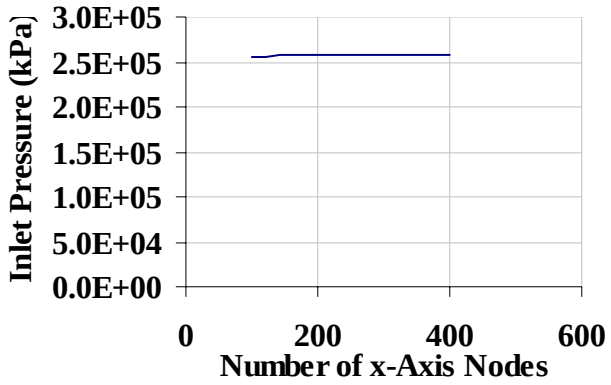

Figure 3.3: Inlet pressure as a function of x-axis nodes

The number of x-axis nodes was found to not have a significant effect on convergence in the inlet pressure. Further studies in chapter five utilized two hundred equally spaced nodes in the x-axis direction. With five equally spaced nodes in the z-axis direction and two hundred equally spaced nodes in the x-axis direction the number equally spaced nodes in the y-axis direction for land was varied using the variables from Table 3.1.

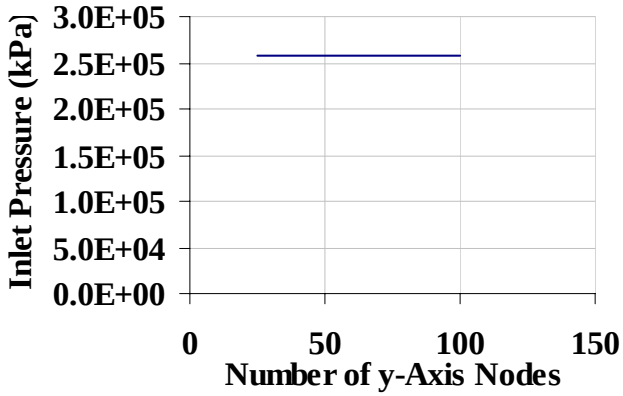

Figure 3.4: Inlet pressure as a function of y-axis nodes in the land

The number of y-axis nodes was found to not have a significant effect on convergence in the inlet pressure. Further studies in chapter five utilized fifty equally spaced nodes in the x-axis direction.

3.2.1 General Three Dimensional Flow Patterns

The qualitative flow patterns in the land and grooves, as predicted by Fluent©, are discussed below. The geometry chosen for this demonstration is summarized in Table 3.2. Figures 3.5 through 3.7 illustrate the *x*, *y*, and *z*-directed (see Fig. 3.1) velocity distributions, at *x*=1000 μm (i.e., half-way along the length of the groove).

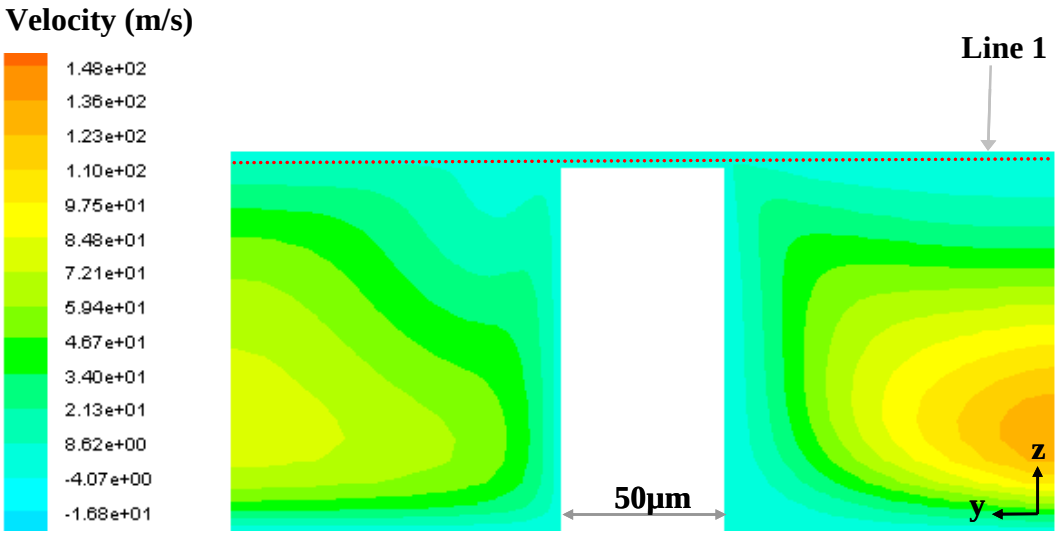

Figure 3.5: Velocity distribution in the *x*-direction (i.e., in the direction of the groove)

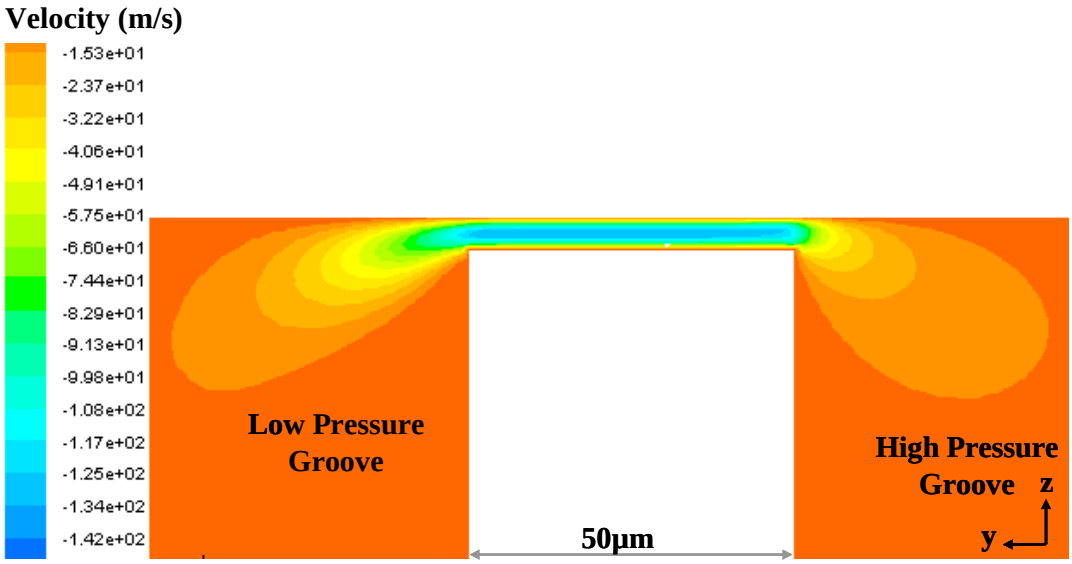

Figure 3.6: Velocity distribution in the *y*-direction (i.e., in the direction across the land).

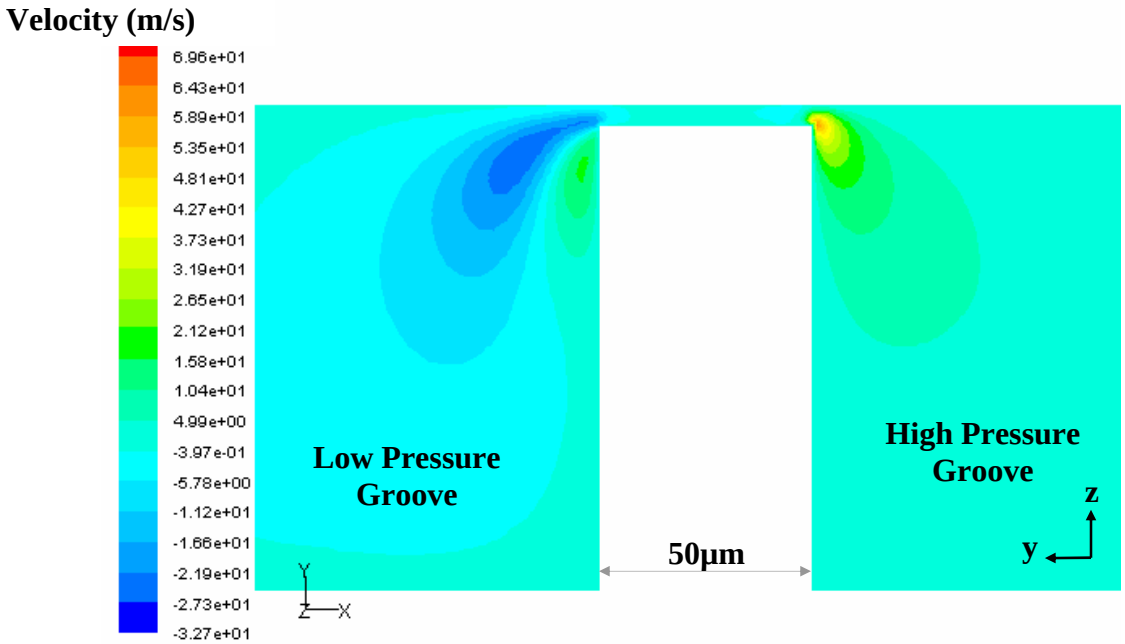

Figure 3.7: Velocity distribution in the *z*-direction (i.e., towards the valve seat).

Table 3.2: Nominal conditions used for Figs. 3.5-3.7

Variable	Value
l_g	2000.0 μm
d_g	100.0 μm
w_g	200.0 μm
δ	6.0 μm
w_l	50.0 μm
μ	2.0e-5 kg-m/s
ρ	0.5 kg/m^3
$\dot{m}_i$	0.5e-6 kg/s
P_{outlet}	0.0 kPa

Well-developed velocity distributions in both the land and grooves can be seen in Figs. 3.5 and 3.3. In Fig. 3.7, sharp gradients in the *z*-axis velocity entering the land from the high pressure groove can be observed. The large gradients in the velocity distribution entering the land are explained through inspection of the static pressure distribution, which is shown in Fig. 3.8 along line 1 (see Fig. 3.5).

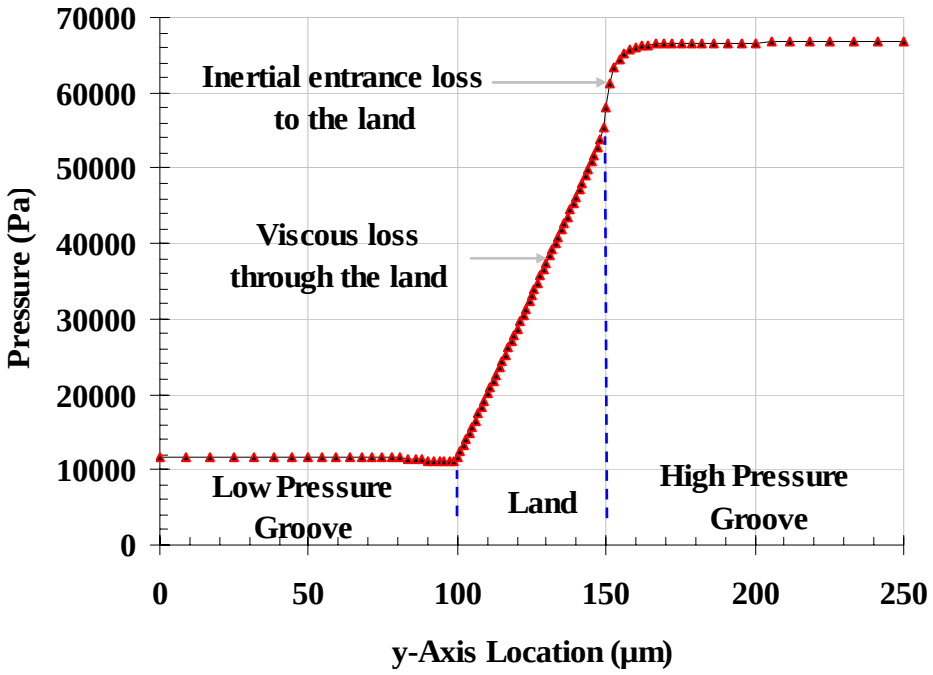

Figure 3.8: Static pressure distribution along line 1 (Fig. 3.5)

Figure 3.8 reveals some interesting behavior in the land. The large inertial entrance loss into the land results in the velocity gradients seen in Fig. 3.7. As expected, there is a linear pressure drop

within the land due to viscous losses. Figure 3.8 shows that we can expect very little inertial pressure loss exiting the land into the low pressure groove. This behavior, which is in contrast to the inertial exit loss coefficient of 1.0 which was assumed in chapter two, foreshadows one source of inconsistency between the existing flow model and three dimensional Fluent© predictions.

3.2.2 CFD Model Comparison with 1-D Model

A quantitative comparison between the one dimensional, incompressible flow model derived in chapter two and the three dimensional Fluent© model discussed in Section 3.1 is shown in Fig. 3.9; the comparison is accomplished using the dimensionless numbers described in chapter 2 and the reader is referred to Section 2.4 for the definition of the variables shown in Fig. 3.9. However, the y-axis represents the mass flow rate and the x-axis the operating condition, as indicated by the Reynolds number in the land. The geometry is held constant as the Reynolds number is changed.

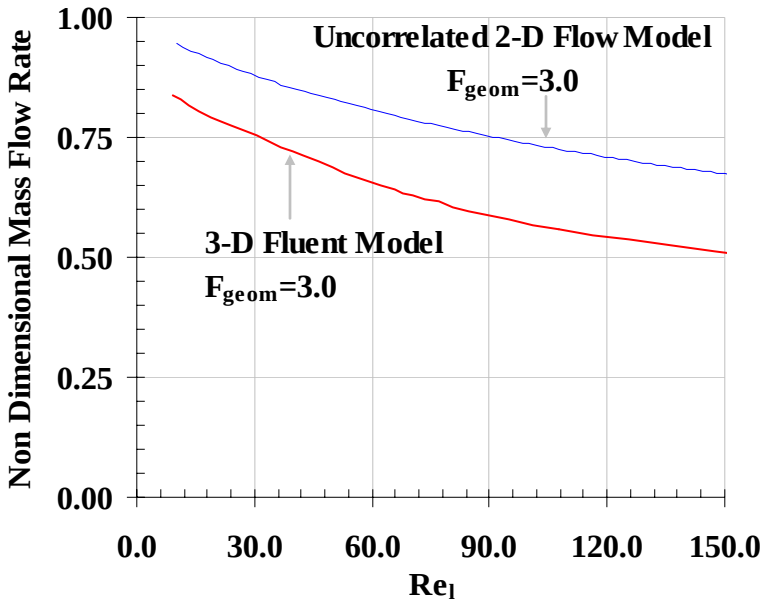

Figure 3.9: Comparison between the two dimensional incompressible no-slip flow model discussed in chapter two and the three dimensional Fluent© model discussed in Section 3.1.

It is evident from Fig. 3.9 that there is a consistent offset between the two dimensional incompressible flow model and the three dimensional Fluent© model exists; the 2-D flow model consistently over-predicts the mass flow rate. Therefore, the following sections discuss the development of more predictive correlations for the groove and land and groove flow behavior.

3.2.3 Groove to Land Inertial Correlation

In order to make the one dimensional flow model more predictive, it is necessary to accurately characterize the inertial pressure loss from the high-pressure groove into the land, as shown in Fig. 3.8. The inertial pressure drop to the land can be expressed, according to White 2003, as:

$$P_{g,x} - P_{l,x} = K_l \frac{1}{2} \rho V_l^2 \tag{3.1}$$

where $P_{g,x}$ is the area averaged pressure in the high pressure groove (at some x-axis location along the groove), $P_{l,x}$ is the pressure in the land after the flow profile has fully developed (at the same x location), K_l is the inertial correlation coefficient, ρ is the density, and V_l is mean flow velocity over the land. It was found that the flow profile within the land becomes fully developed within a few micrometers, as demonstrated in Fig. 3.5. Assuming laminar, incompressible, constant viscosity flow, it is expected that the loss coefficient can be expressed as a function of the Reynolds number based on the valve seat clearance and the ratio of the valve seat clearance to the groove height, as shown in Eq. (3.2).

$$K_l = fxn\left(Re_\delta, \frac{\delta}{h_g} \right) \tag{3.2}$$

by applying the principles of Eqs. (3.1) and (3.2) at the mid point, x=1000 μm, of the land and groove geometry from Table 3.2 while iterating Fluent© over a wide range of inlet mass flow

rate, density and viscosity it can be shown that the calculated value of K_I collapses to smooth curves, as shown in Fig. 3.10.

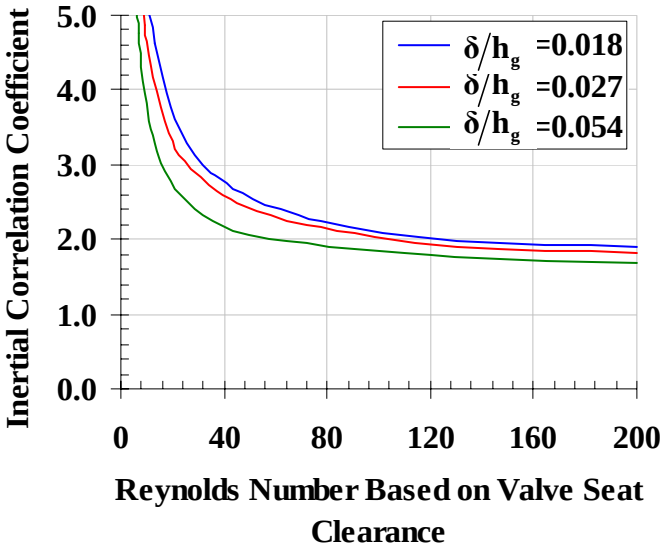

Figure 3.10: Inertial correlation coefficient, K_I, as a function of Reynolds number based on valve seat clearance, Re_δ, for various ratios of valve seat clearance to groove height, δ/h_g

3.2.4 Groove Correlation

An accurate representation of the flow behavior in the grooves is also necessary to make the 2-D model predictive. Figure 3.11 shows the pressure distribution in the high and low pressure grooves for $\dot{m}_i$ =1.0e-6 kg/s and ρ=1.0 kg/m^3 with the remaining properties, conditions, and dimensions as listed in Table 3.2.

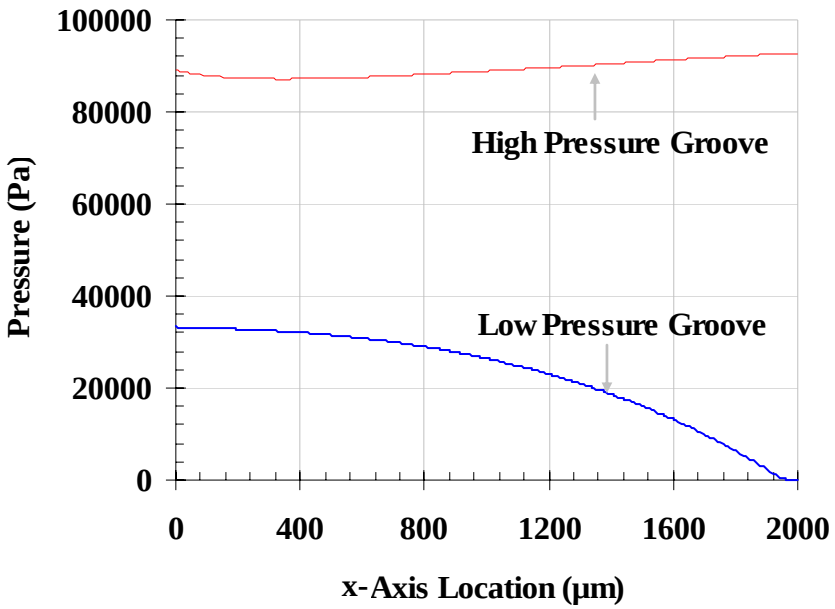

Figure 3.11: Pressure as a function of x-axis location in the high and low pressure groove for the dimensions, conditions, and properties described above

Figure 3.11 reveals some interesting incompressible behavior in the grooves. The pressure in the high pressure groove does, at some point in *x*, begin to ascend and eventually rises above the inlet pressure. In addition, the difference between the maximum and minimum pressure in the low pressure groove is substantially larger than in the high pressure groove. The behavior in the grooves, as demonstrated by Fig. 3.11, can be understood by considering the pressure change associated with decelerating or accelerating the flow; in the high pressure groove the flow velocity is reduced (as flow passes into the land) and thus the flow is decelerating which causes a substantial pressure rise (enough to overwhelm the viscous pressure loss). The flow acceleration in the low pressure groove acts to increase the pressure drop; thus the marked difference in behavior between the two grooves.

Clearly, the 2-D model must account for both viscous pressure loss and momentum changes in the grooves in order to be predictive. The pressure gradient in either the high or low pressure

groove must be re-formulated in terms of a viscous pressure loss, due to shear at the groove boundaries, as well as an inviscid pressure gain or loss related to a change in the mean z-axis velocity for the respective groove, Panton 2005:.

$$-\frac{dP_g}{dx} = \underbrace{\frac{f}{D_h}\frac{\rho}{2}V_g^{\,2}}_{\text{Viscous Term}} + \underbrace{\rho V_g \frac{dV_g}{dx}}_{\text{Inviscid Term}} \tag{3.3}$$

where P_g is the area averaged pressure in either the high or low pressure groove, f is the friction factor that characterizes the viscous pressure loss in the groove, D_h is the hydraulic diameter of the groove as defined in terms of the groove cross-sectional area ($A_{c,g}$) and perimeter (per_g) in Eq. (3.4), V_g is the mean x-axis velocity in the groove, and ρ is the density.

$$D_h = 4\frac{A_{c,g}}{per_g} \tag{3.4}$$

Initially the mean velocity in the high pressure groove is relatively high; therefore the viscous pressure loss is greater than the inviscid pressure gain and the pressure decreases along the z-axis. However, at some point the mean velocity in the high pressure groove reaches a low enough point that the inviscid pressure gain overcomes the viscous pressure loss and the pressure in the high pressure groove begins to increase. This reasoning also explains why the difference between the maximum and minimum pressure in the low pressure groove is substantially larger than the high pressure groove. In the low pressure groove there is a viscous pressure loss and an inviscid pressure loss due to a constant increase in the mean velocity.

The friction factor, f, in Eq. (3.3) can be formulated in terms of the Reynolds number based on the hydraulic diameter for the respective groove, as shown in Eq. (3.5).

$$f = fxn\left(Re_{D_h}\right) \tag{3.5}$$

To obtain the friction factor, the three dimensional Fluent© model is run over a wide range of inlet mass flow rate, density and viscosity while holding the outlet gage pressure constant at 0.0 kPa with all other values as listed in Table 3.2. Area average values of the important terms in Eq. (3.3), specifically the pressure gradient, mean velocity, and mean velocity gradient, are evaluated at the mid-point of both the high- and low-pressure grooves (i.e., at x=1000 μm). The friction factor is then calculated from the CFD result by subtracting the inviscid term from the total pressure gradient, as shown in Eq. (3.6)

$$f = \frac{-2 D_h \left(\frac{dP_g}{dx} - \rho V_g \frac{dV_g}{dx} \right)}{\rho V_g^{\,2}} \tag{3.6}$$

Solutions for the friction factor in the high and low pressure groove collapse onto different, smooth curves, as shown in Fig. 3.12. The difference in high and low pressure groove friction factor is a result of the difference in boundary layer behavior between the high and low pressure groove as seen in Fig. 3.5.

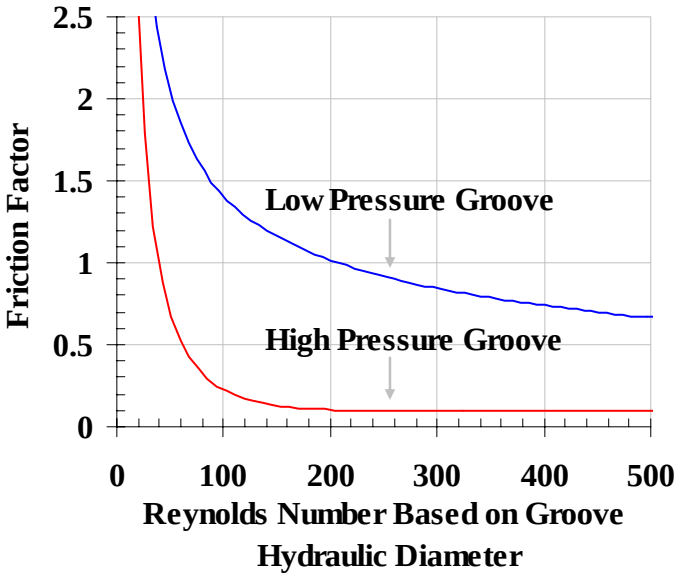

Figure 3.12: Friction factor, *f*, in the high and low pressure groove as a function of the Reynolds number based on the hydraulic diameter, Re_{D_h}

3.3 Manifold Modeling

In order develop a predictive model of the entire valve that is also computationally efficient and therefore useful for design and optimization it is necessary to characterize the flow in both manifold regions using appropriate correlations that are based on more rigorous, 3-D CFD models of these areas. The purpose of this section is to generate a set of non-dimensional relations that govern the inlet and outlet manifolds; thus making the complete valve model more predictive. The manifold volume is shown in Figure 3.14.

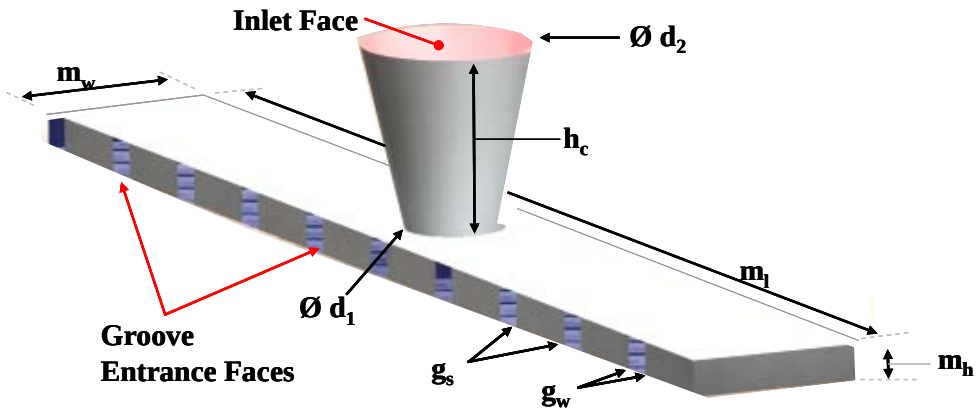

Figure 3.14: Manifold volume

In Fig. 3.14, d_2 is the inlet diameter, d_1 is the exit cone throat diameter, m_h is the manifold height, m_w is the manifold width, m_l is the manifold length, g_s is the groove entrance spacing, h_c is the inlet cone height, and g_w is the groove entrance width. Assuming steady, laminar, constant viscosity, constant density flow it is expected that the pressure drop in a manifold may be represented in terms of a traditional, inertial pressure loss expression, Eqs. (3.7) and (3.8):

$$\Delta P_h = \frac{1}{2} K_l \rho_h V_c^2 \tag{3.7}$$

$$V_c = \frac{\dot{m}_h}{\rho_h \frac{\pi}{4} d_2^2} \tag{3.8}$$

where ΔP_h is the total pressure drop through the manifold, ρ_h is the fluid density in the manifold, V_c is a characteristic velocity that is defined in Eq. (3.8) as mean velocity through d_2, $\dot{m}_h$ is the total mass flow rate through the manifold, and K_l is the inertial loss coefficient. The objective of this study is to correlate the factor K_l against the Reynolds number based on diameter d_2 and the geometry group d_1/m_w. Manufacturing limitations fix many of the dimensions shown in Fig. 3.14; the dimensions which remain constant in the modeling process are summarized in Table 3.3.

Table 3.3: Fixed Variables used in Manifold Modeling

Variable	Value
g_s	300 μm
g_w	100 μm
D_1	500 μm
h_c	500 μm
m_h	100 μm
m_w	500 μm
m_l	4000 μm

The conical entrance hole shown in Fig. 3.14 is fabricated by pressing a fine needle through the Pyrex substrate; as a result of this poorly controlled process, the diameter d_2 will vary slightly from valve to valve. Therefore the diameter d_2 will be allowed to vary in the model. The conical entrance hole axis is centered in the manifold. The three dimensional geometry was developed using hex/wedge cells in Gambit, as shown in Fig. 3.15.

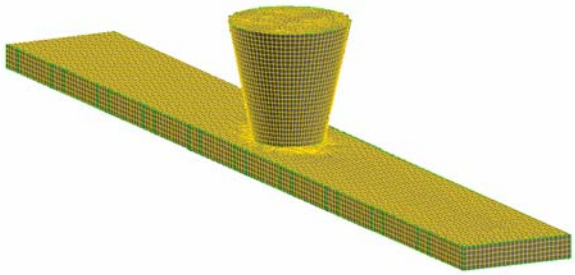

Figure 3.15: Mesh geometry of the manifold volume

The boundary conditions can be imposed on the model shown in Figure 3.15 in several different ways. Because the flow must ultimately pass through a gap of only a few micrometers in the land and groove region, the resistance to flow through the land and groove area is much greater than the resistance to flow through the manifolds. This observation suggests that the mass flow rate through each of the groove entrance faces, shown in Fig. 3.14, will be nearly equal. Therefore a suitable choice of boundary conditions for the groove entrance faces would be either a mass flow inlet or outflow; in either case the mass flow rate should be equally distributed. The inlet face may be chosen to be either a mass flow inlet, outflow, or constant pressure outlet. All other faces were assumed to be walls.

To generate a large set of model predictions that can subsequently be used to develop the correlation, the CFD model must be run over a range of conditions that fully defines the K_l vs. *Re* curves. Therefore, it is desirable to use a relatively coarse mesh size in order to reduce computational time. An initial study was conducted in order to identify a proper grid size. For this preliminary study, the inlet face was assumed to be uniformly distributed mass flow inlet and the outlet faces were assumed to be equally distributed outflows. The study used fluid properties consistent with air at room temperature and pressure. Figure 3.16 illustrates one characteristic of the solution, the *x*-velocity as a function of axial position at the manifold centerline, for various values of the mesh size (*dx*, the grid step size); the ripples in the velocity are related to fluid entering the grooves.

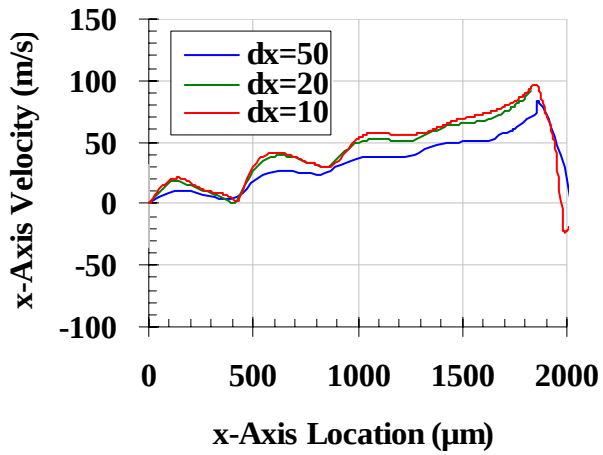

Figure 3.16: Convergence analysis using various values of the grid spacing in the high pressure manifold

Figure 3.16 shows that a mesh size of approximately 20 µm is nearly converged and suggests that a mesh size of 20 µm would be acceptable.

3.3.1 High Pressure Manifold

The inertial loss coefficient, K_l, shown in Eq. (3.7), is based on the total pressure drop across the manifold, which is a somewhat ambiguous quantity. However, the model of the groove and land area includes, as a boundary condition, the inlet and exit pressures associated with the grooves; therefore it is appropriate to define the pressure drop as the difference between the manifold inlet face and groove entrance face pressures.

The calculation was carried out using two sets of boundary conditions; first, a constant pressure outlet was assumed for the groove entrance faces. This is an unrealistic boundary condition as it does not guarantee the mass flow rate will be equally distributed across the grooves. In fact, careful examination of the results reveals that those grooves in close proximity with the conical inlet hole receive most of the flow. Therefore, the calculations were also accomplished assuming an equally distributed outflow boundary condition across the groove faces; in this case, the

pressure difference in the inertial loss coefficient, K_I, calculation was taken to be the difference between the inlet pressure and the area averaged pressure across all of the groove faces. Figure 3.17 illustrates the results of both calculations in the form of K_I vs. *Re* curves; notice that the very different set of boundary conditions produce nearly equivalent K_I vs. *Re* curves. This result, is, at first, surprising; however, the result is consistent with the dominant fluid resistance being related to the conical hole exit plane with very little additional pressure drop resulting from fluid flow in the manifold itself.

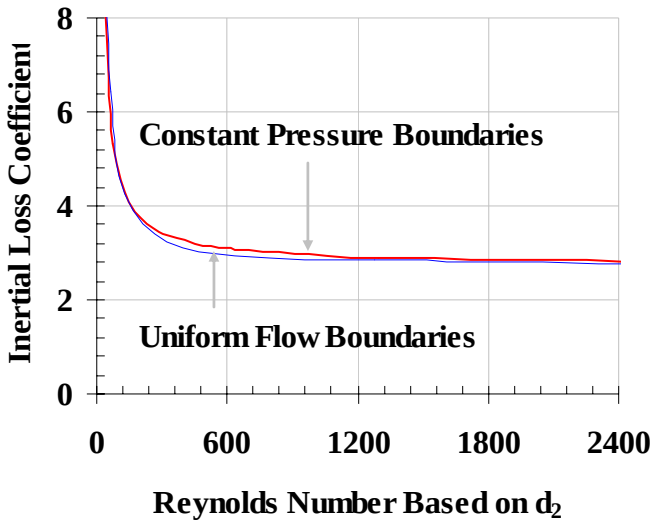

Figure 3.17: Boundary condition comparison

Figure 3.17 suggests that it might be possible to assume that the pressure in the groove entrances and exits are at a uniform value for this particular geometry where the pressure drop between the end of the conical hole and the groove faces is small, which is a helpful assumption when constructing a model of the entire valve. However, for the purpose of determining K_I as a function *Re*, the groove entrances are assumed to have equally distributed outflow boundary conditions as this is the more rigorously correct boundary condition and the methodology may be applied to alternative manifold configurations in the future. A typical flow pattern and pressure

distribution is shown in Figs. 3.18 and 3.19, respectively. The conditions associated with Figs. 3.18 through 3.21 are summarized in Table 3.4.

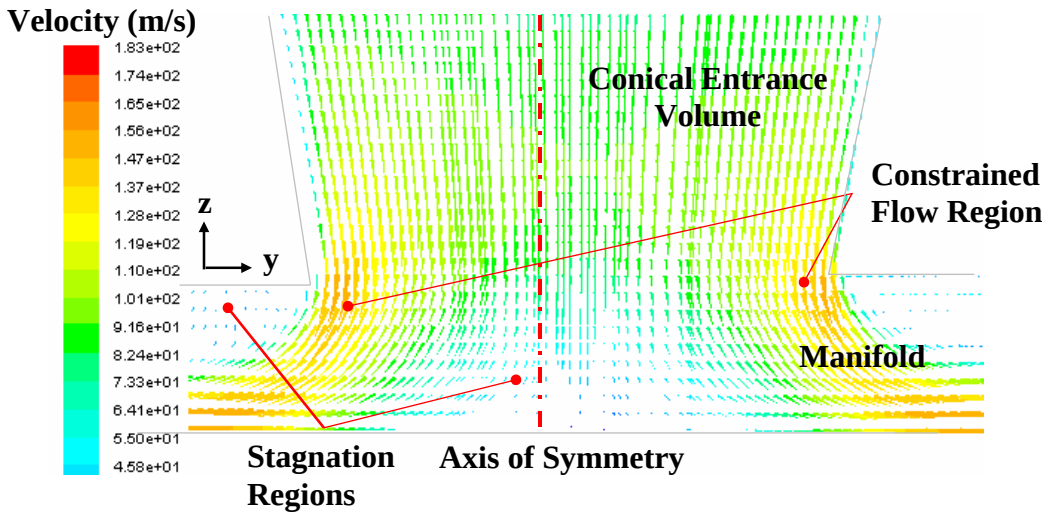

Figure 3.18: Typical velocity distribution in the conical entrance volume for the high pressure manifold with the dimensions, properties, and conditions shown in Table 3.4

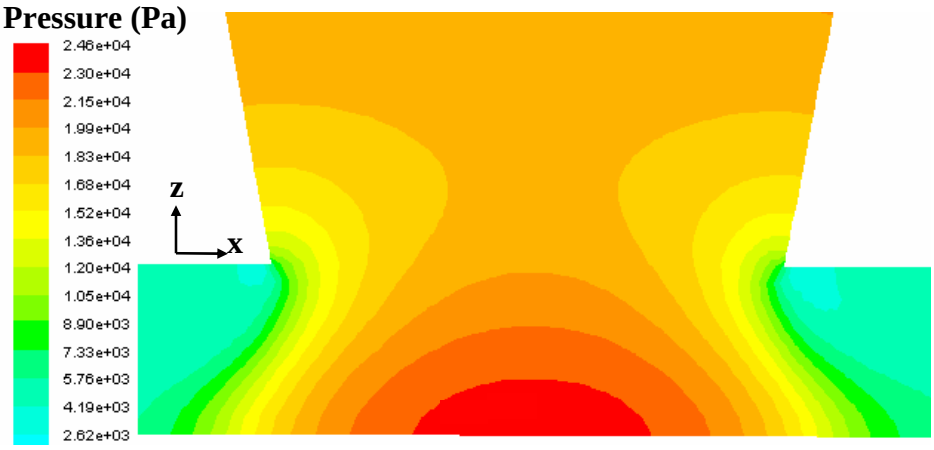

Figure 3.19: Typical pressure distribution in the conical entrance volume for the high pressure manifold with the dimensions, properties, and conditions shown in Table 3.4

Table 3.4: Conditions used to generate Figs. 3.18 through 3.21

Variable	Value
$\dot{m}_h$	1.0e-5 kg/s
ρ_h	1.2 kg/m^3 0.6 kg/m^3…Fig. 3.21
μ_h	2.0e-5 kg-m/s 2.0e-4 kg-m/s…Fig. 3.21
d_1	300.0 μm

Figures 3.20 and 3.21 illustrate the pressure in the manifold region as a function of position for two very different cases; Fig. 3.20 is an inertially dominated condition (high density and low viscosity) while Fig. 3.21 is viscous dominated (low density, high viscosity).

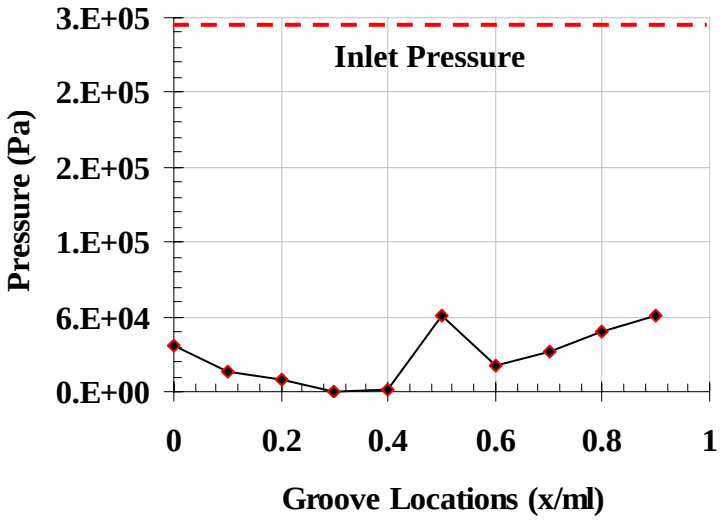

Figure 3.20: Typical pressure distribution in the groove entrances for the high pressure manifold with inertial dominated flow, with the dimensions, properties, and conditions shown in Table 3.4

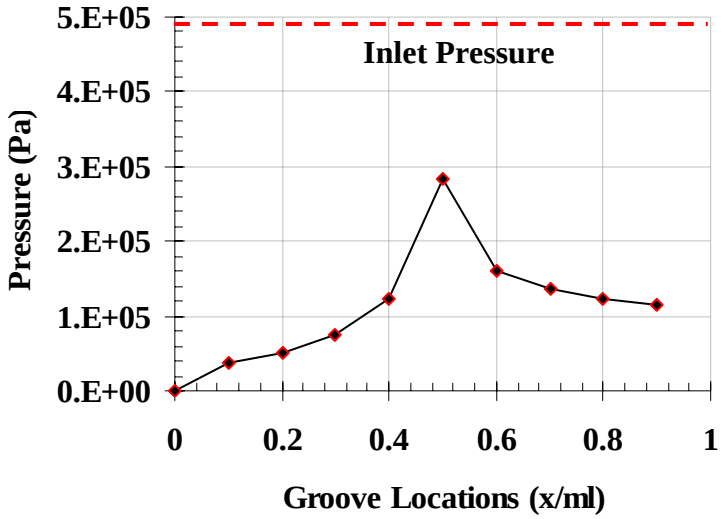

Figure 3.21: Typical pressure distribution in the groove entrances for the high pressure manifold with viscous dominated flow, with the dimensions, properties, and conditions shown in Table 3.4

Figures 3.20 and 3.21 demonstrate that very different behavior can occur in the manifolds depending on whether viscous or inertial terms are dominating. In Fig. 3.20 the viscous losses that occur as the fluid flows toward the outer groove entrances is overcome by the inertial gain from to the fluid slowing down; therefore the pressure increases toward the outer grooves. In Fig. 3.21 viscous losses dominate and therefore the pressure decreases toward the outer groove entrances. The valve design will be used in cryogenic applications and therefore the pressure distribution in the manifold will typically resemble Fig. 3.20.

The inertial loss coefficient, K_l, as a function of Reynolds number based on diameter two, Re_{d2}, is shown in Fig. 3.22 for the high pressure manifold. To generate the curves shown in Fig. 3.22 the viscosity, density, and mass flow rate into the manifold were all allowed to vary.

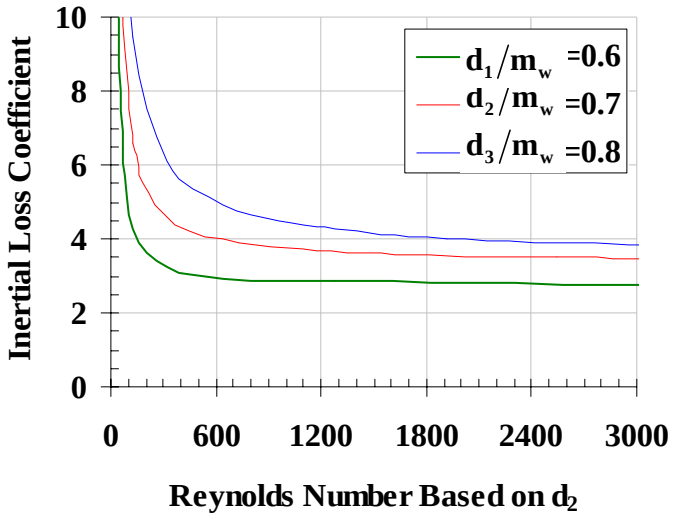

Figure 3.22.a: Inertial loss coefficient as a function of Reynolds number based on diameter two for the high pressure manifold with ten grooves and w_q=100 µm

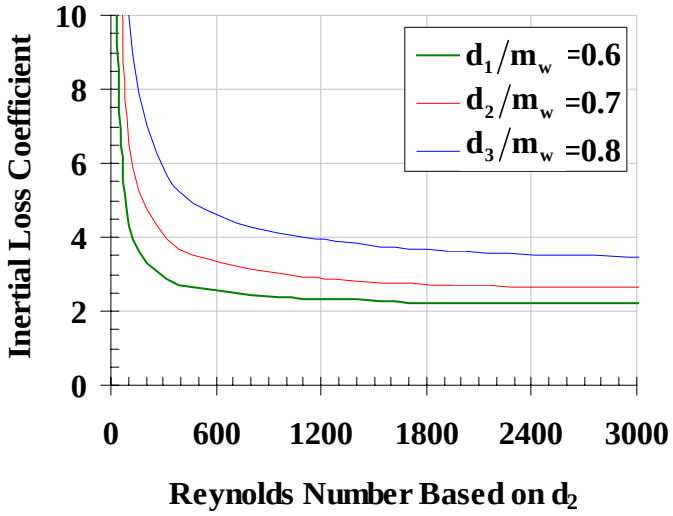

Figure 3.22.b: Inertial loss coefficient as a function of Reynolds number based on diameter two for the high pressure manifold with twenty grooves and w_g=50 µm

3.3.2 Low Pressure Manifold

The flow pattern for the low pressure manifold was found to be substantially different then the high pressure manifold. Recirculation was observed in the rectangular manifold and conical volume which tends to compromise the assumption of laminar flow; therefore a more complex

handling of the viscous terms is required. The full Reynolds stress equations were chosen to handle the viscous terms within Fluent©; this turbulence model tends to smooth out the flow although recirculation patterns were still observed in these regions. Figures 3.23 and 3.24 illustrate the typical recirculation and flow patterns for the low pressure manifold. Table 3.5 summarizes the parameters used to generate Figs 3.23 and 3.24.

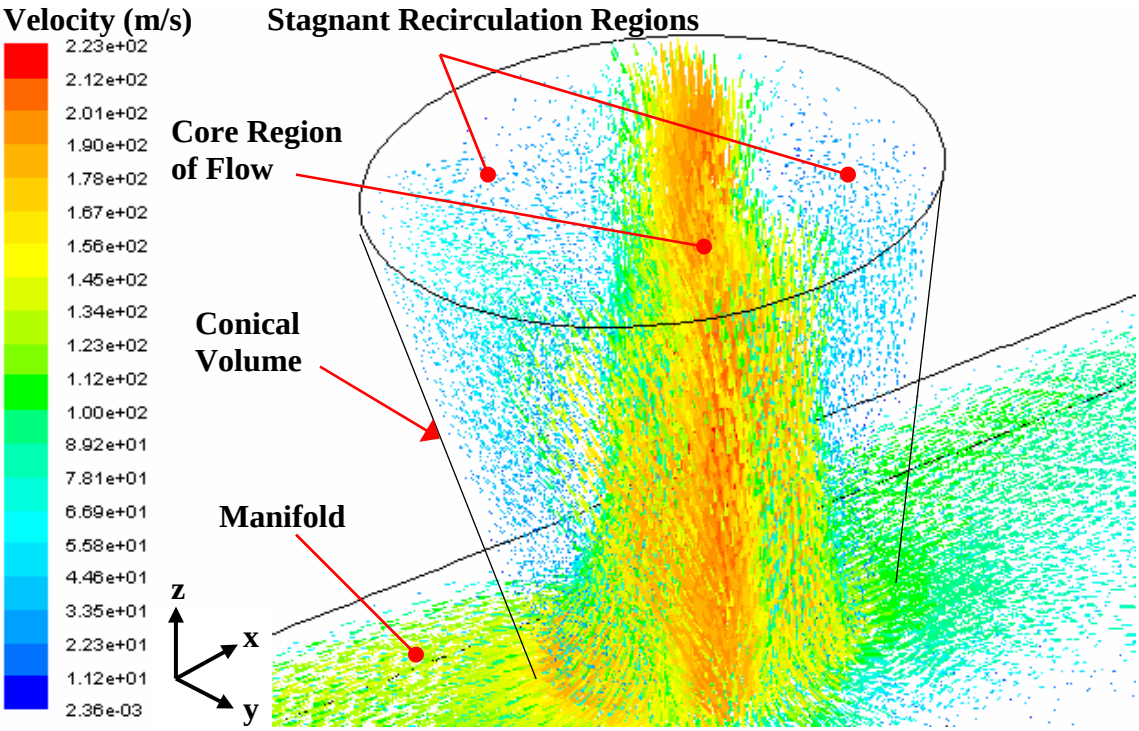

Figure 3.23: Typical velocity distribution in the conical entrance volume for the low pressure manifold using the properties, conditions, and geometry from Table 3.5.

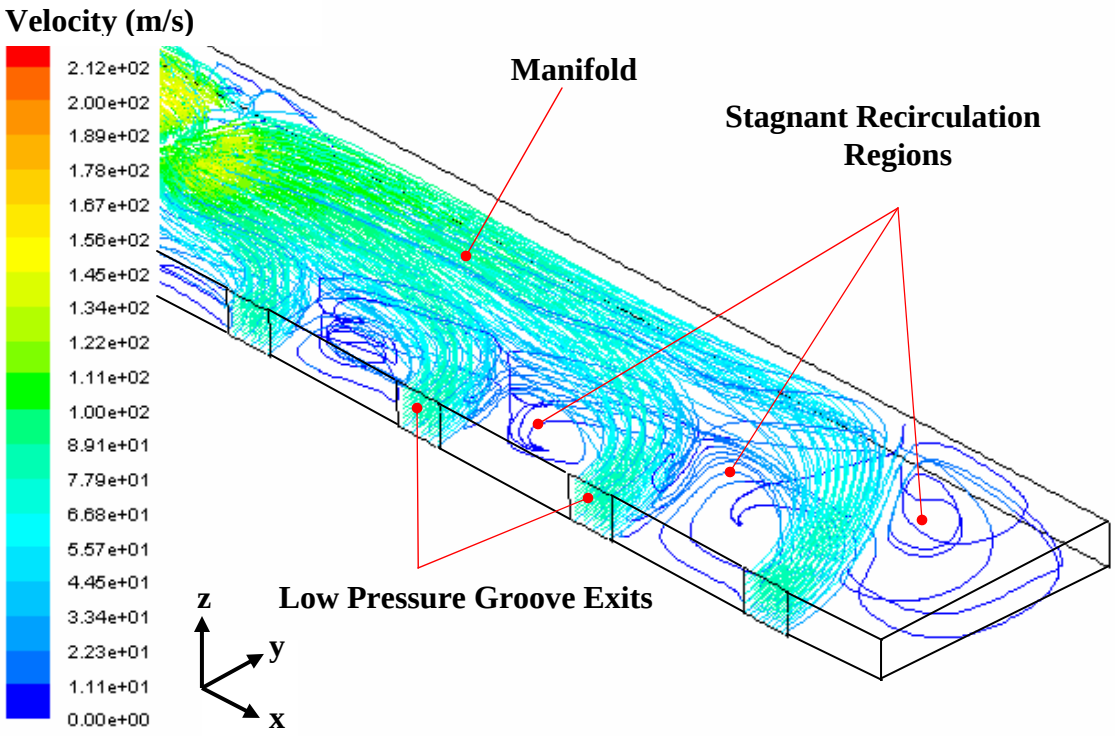

Figure 3.24: Typical streamlines in the low pressure manifold using the properties, conditions, and geometry from Table 3.5

Table 3.5 Parameters for Fig.'s 3.23 and 3.24

Variable	Value
$\dot{m}$	1.0e-5 kg/s
ρ	1.3 kg/m^3
μ	1.8e-5 kg-m/s
d_1	300.0 μm
d_2	350.0 μm
d_3	400.0 μm

Values of the inertial loss coefficient, K_l, that characterize the low pressure grooves were obtained in the same way and were also found to collapse to smooth curves, as shown in Fig. 3.25. These curves vary slightly from those shown in Fig. 3.22.

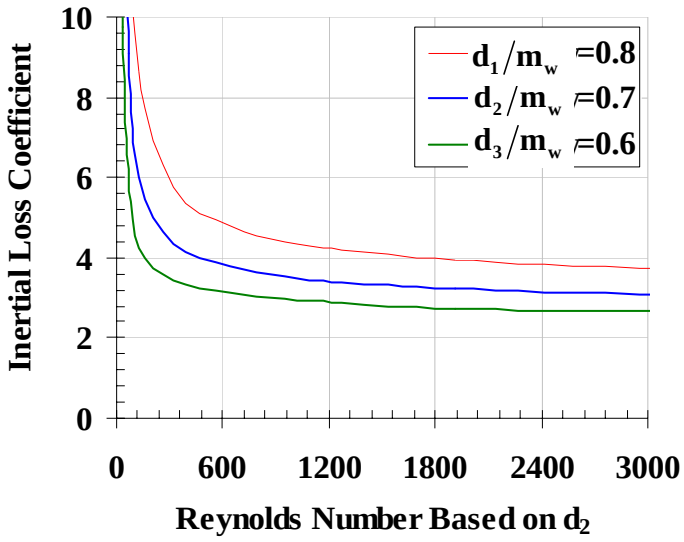

Figure 3.25: Inertial loss coefficient as a function of Reynolds number based on diameter two for the low pressure manifold with twenty grooves and w_g=50 µm, also for ten grooves with w_g=100 µm

3.3.3 Manifold Optimization Studies

Additional studies were carried out to investigate the effects of changing the placement of a single conical inlet to the manifold as well as explore the effects of adding additional conical inlets. Initial studies kept all of the fluid properties and geometric values constant; the *x*-axis location of the conical inlet was varied in order to determine the optimal location for the inlet in order to minimizing the pressure drop associated with a manifold fed by a single inlet hole. Figure 3.26 illustrates the inertial loss coefficient (which is proportional to the pressure loss) for an inlet manifold of diameter d_1=300 µm operating at conditions consistent with Re_{d2}=225. Note that it is most efficient to place the conical inlet at the centerline of the manifold (although this may not be optimal from a flow distribution standpoint).

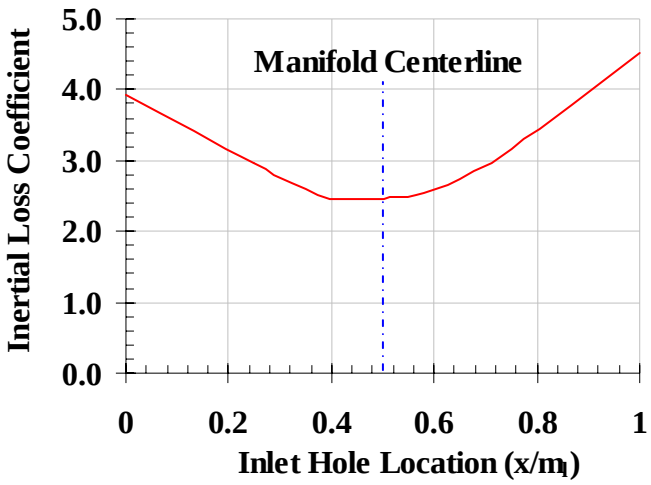

Figure 3.26: Inertial loss coefficient as a function of *x*-axis location of a single conical entrance in the high pressure manifold

Additional equally spaced conical inlets were added to the high manifold model in an attempt to determine the magnitude of the pressure drop reduction that could be achieved using a multi-inlet manifold design as compared to a single-inlet manifold. The figure of merit that is used to characterize the influence of adding additional conical entrance volumes is the pressure ratio, defined as

$$\text{Pressure Ratio} = \left.\frac{\Delta P_h \text{ with multiple conical inlets}}{\Delta P_h \text{ with one conical inlet}}\right|_{\text{holding } \dot{m},\ \rho,\ \mu,\ \text{and } d_1 \text{ constant}} \tag{3.9}$$

Figure 3.27 illustrates the pressure ratio as a function of the number of conical entrance volumes for the high pressure groove, with $\dot{m}_h$ = 1.0e-6 kg/s, ρ=0.5 kg/m^3, μ=2.0e-5 kg-m/s, and d_1=300 μm.

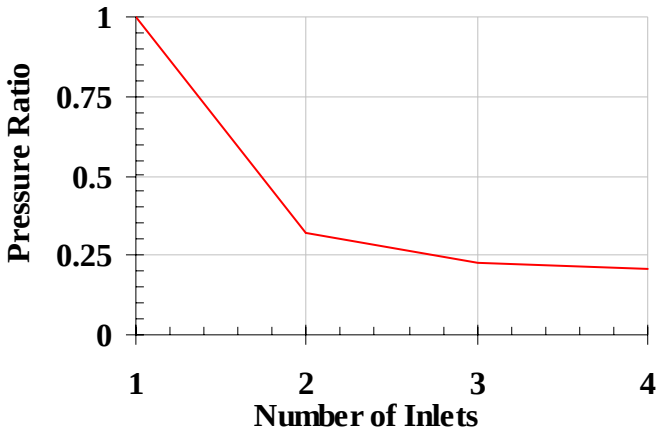

Figure 3.27: Pressure ratio as a function of the number of evenly spaced conical inlets for the high pressure manifold

Figure 3.27 shows the benefit of adding even just one additional inlet to the manifold; this would decrease the relative pressure drop by a factor of three. However as well shall see in chapter six, the manifolds in general play a lesser role in the total pressure drop of the valve.

3.4 Conclusion

In this chapter a 3-D CFD model was generated and showed that the two dimensional incompressible model developed in chapter two was, as derived, not predictive. As a result of this discrepancy, a series of correlations characterizing the inertial pressure terms that characterize flow within a single land and groove were generated. Also, the inviscid effects associated with flow deceleration and acceleration were found to be important and therefore included in the 2-D model. In addition, correlations that characterize the behavior of the high and low pressure manifolds were developed; these correlations can be easily integrated with simple models of the groove/land to obtain a complete valve model.

3.5 **References**

F.W. White, 2003, “Fluid Mechanics,” 5th ed., McGraw-Hill Higher Education

R.L. Panton, 2005, “Incompressible Flow,” 3rd ed., John Wiley & Sons

Chapter 4

Experimental and Analytical Structural Displacement Results

4.1 Problem Discussion

In chapter two it was determined that there is a strong relationship between the valve seat clearance and the mass flow rate. Figure 4.1 demonstrates this strong relationship by showing the incompressible one dimensional mass flow rate from the model developed in chapter two for a single land and groove as a function of the valve seat clearance for the dimensions, properties, and conditions summarized in Table 4.1.

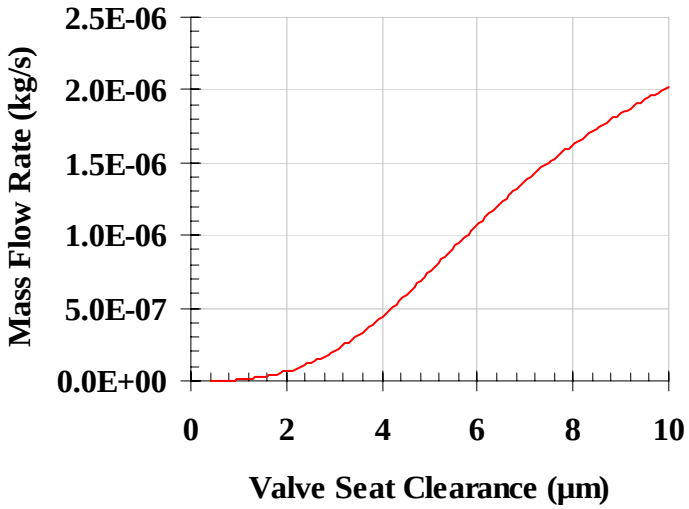

Figure 4.1: The mass flow rate through a single land and groove as a function of valve seat clearance for the dimensions, properties, and conditions shown in Table 4.1

Table 4.1: Variables for Fig. 4.1

Variable	Value	
ρ	0.5	kg/m^3
μ	2.0e-5	kg-m/s
w_g	100.0	µm
w_l	50.0	µm
l_g	2.0	mm
h_g	100.0	µm

Table 4.1 cont.

P_{inlet}	100.0	kPa
P_{outlet}	0.0	kPa

The need for an accurate model combined with the sensitivity of the mass flow rate to micron-scale changes in the valve seat clearance, as seen in Fig. 4.1, requires that the response of the valve seat clearance to various structural loadings be well understood. This chapter presents a structural model of the valve that is supported through experimental measurements. The first section discusses how the epoxy joint characteristics were determined using experimental data and a finite element analysis model. The remainder of the chapter discusses the model used to determine the valve seat clearance from the displacement of the entire valve assembly given the structural loading. The results of this analysis will become a part of the full valve model.

4.2 Epoxy Joint Characterization Experiment

The valve structure is a composite of materials that are connected through both epoxy joints and anodic bonds (silicon to Pyrex©). The structural properties of the valve materials are well understood with the exception of the epoxy joint. It is likely that the epoxy joint will play a role in seat clearance displacement as it is ubiquitous within the valve structure and therefore we would like to better understand the epoxy's response to structural loading. This section will discuss experimental data that is combined with a structural model in order to isolate the epoxy response and therefore quantify the epoxy joint material properties.

To carry out the experiment, the structural test piece shown in Fig. 4.2 was constructed to allow the displacement of a Pyrex© surface to be measured in the test assembly shown in Fig. 4.3. The

Pyrex© was anodically bonded to a silicon substrate which was subsequently attached to a hollow Macor© cap using Stycast© epoxy. The dimensions of the test pieces are consistent with those used in the micro-valve design.

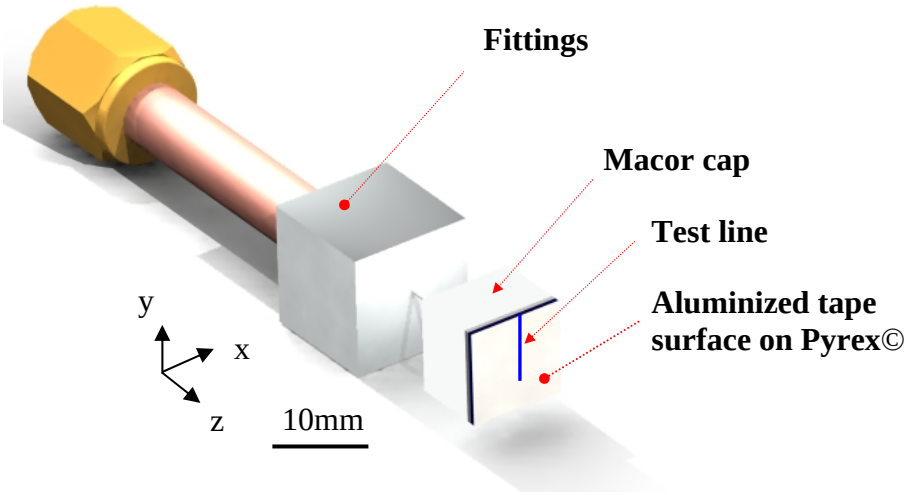

Figure 4.2: Structural test piece

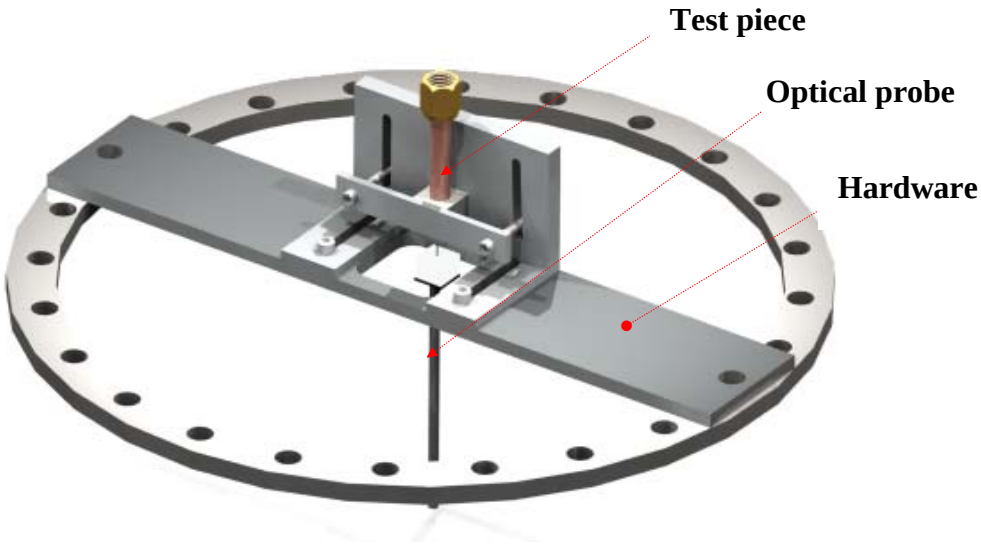

Figure 4.3: Structural test assembly

The displacement of the Pyrex© surface was measured using an optical probe that could be positioned along the test line (see Fig. 4.2) in order to measure the structural displacement in response to the internal pressure. A micrometer was used to adjust and record the location of the optical probe along the test line. The results of the experiment allowed the *z*-axis displacement

(i.e., the displacement along the coordinate of the PZT displacer) of the composite structure made up of the Macor© cap, Pyrex© base plate, and epoxy joint to be measured; the results of the test are shown in Fig. 4.4, with P_i being the gage pressure in the Macor© cap.

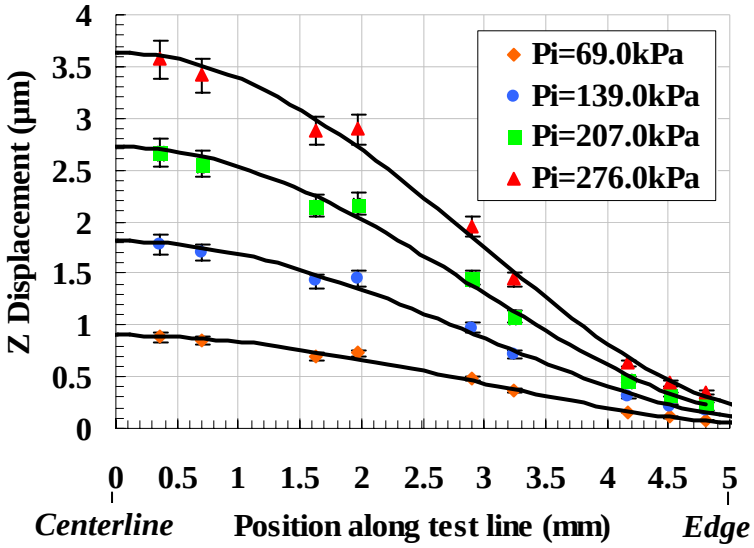

Figure 4.4: Measured *z*-axis displacement as a function of position along the test line for various internal pressures

Using the displacement results of Fig. 4.4, the structural response of the epoxy joint can be isolated from the compliance of the remainder of the structure. A finite element (FE) model of the Macor© cap and Pyrex©/silicon assembly was generated using CosmosWorks© software; the geometry was consistent with the test piece used in the experiment and the structural constraints, as shown in Fig. 4.5. The model neglects any compliance between the Macor© cap and silicon surfaces by assuming that they are rigidly attached (i.e., the epoxy joint is assumed to be infinitely thin and perfect).

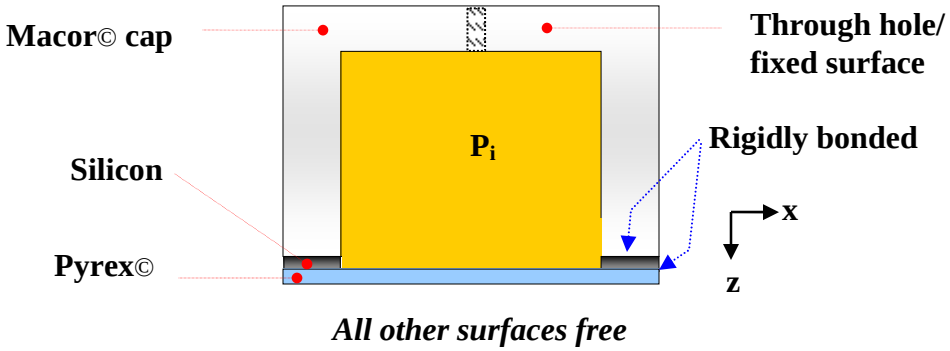

Figure 4.5: Cross-sectional view of the FE model of the test piece with constraints

Figure 4.6 shows the grid generated for the geometry shown in Fig. 4.5.

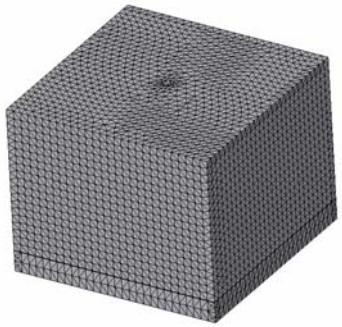

Figure 4.6: FE structural model mesh of the test piece

The experimental data and FE model predictions are overlaid in Fig. 4.7 for a particular internal gage pressure (270.0 kPa). Note that the experimentally measured displacement is larger than the FE model and the slope at the edge is increased; these trends are consistent with an imperfect epoxy joint and therefore the effect of the epoxy is related to the difference in these results, which is shown in Fig. 4.8.

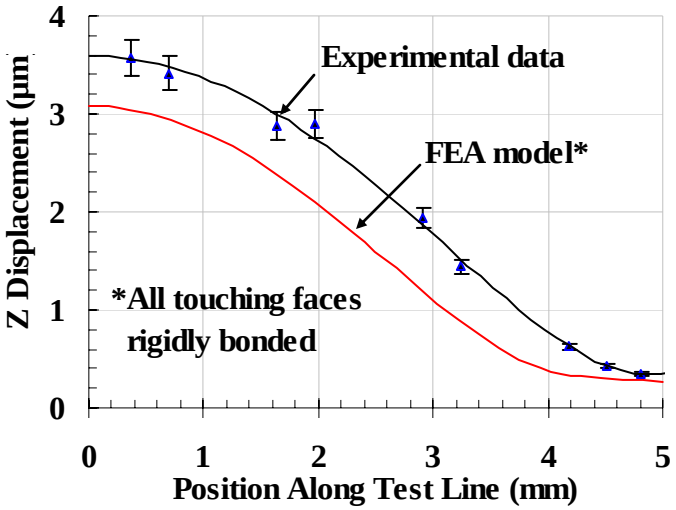

Figure 4.7: Measured and predicted *z*-axis displacement as a function of position along the test line for an internal gage pressure of 270.0 kPa

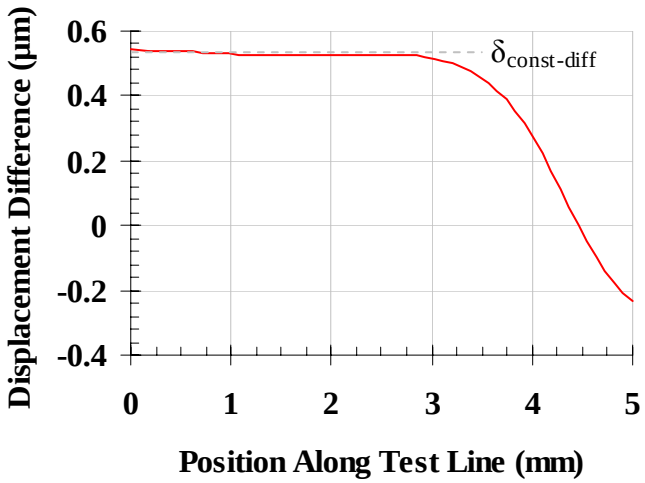

Figure 4.8: Difference in measured and rigidly bonded FE model *z*-axis displacement at 270.0 kPa gage pressure

Figure 4.8 is a revealing plot in that beyond about one millimeter from the epoxy bond, the difference between the experimental data and FE model is approximately constant ($\delta_{const\text{-}diff}$). The source of the constant offset is likely related to the compliance of the epoxy joint. If the epoxy joint thickness (t_{epoxy}) can be estimated then the elastic modulus of the epoxy joint (E_{epoxy}) can be calculated approximately assuming that the constant offset is related to a simple stretching

of the epoxy joint. The elastic modulus required to produce the observed deformation is therefore given by:

$$E_{epoxy} = \frac{P_i \frac{A_{applied}}{A_{epoxy}}}{\delta_{cont-diff} / t_{epoxy}} \tag{4.1}$$

where $A_{applied}$ is the area which is pressurized on the Pyrex© face and A_{epoxy} is the area of the epoxy normal to the Pyrex© face. It was estimated (visually) that the epoxy thickness is 380.0 µm which results in an elastic modulus of 3.6e08 Pa. Assuming a Poisson ratio of 0.2 yields a shear modulus of 1.44e08 Pa.

These values for the estimated elastic and shear modulus allow a finite thickness layer of epoxy to be inserted into otherwise the same FE structural model shown in Fig. 4.6; the predicted and measured displacement along the test line for 270.0 kPa are shown in Fig. 4.9. The error bars in Fig. 4.9 are calculated from the error of the optical probe.

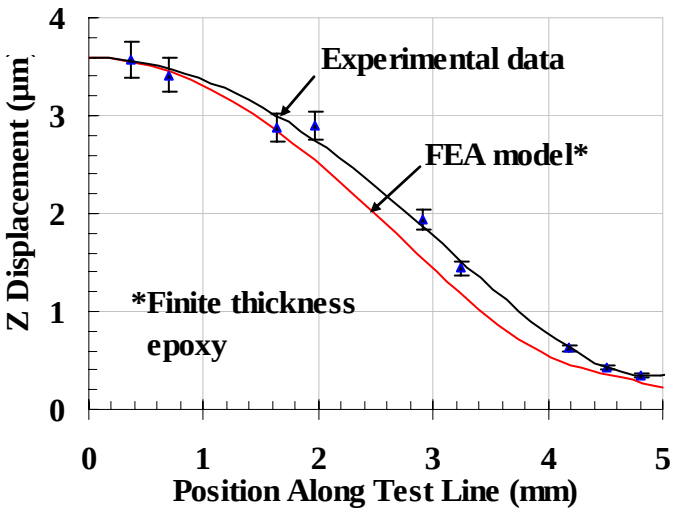

Figure 4.9: Measured and predicted displacement (using an FE model that accounts for the epoxy compliance) as a function of position along the test line for an internal gage pressure of 270.0 kPa.

Figure 4.9 shows good agreement between the predicted and measured maximum *z*-axis displacement; however, the complex loading and boundary conditions near the epoxy leads to deviation between the FEA model and experimental results near the edge. For the purpose of this exercise, the total agreement can be considered adequate using the derived elastic and shear modulus.

4.3 Estimation of the Valve Seat Clearance Displacement from Structural Loading

The structural properties of Stycast© epoxy at room temperature were estimated in section 4.1,. Using the results of the previous analysis it is possible to estimate the valve seat clearance displacement given the structural loading for the entire valve assembly. The valve assembly is shown in Fig. 4.10; the valve is composed of a PZT stack, Macor© cap, Pyrex©/silicon assembly, Macor© header, and various epoxy joints.

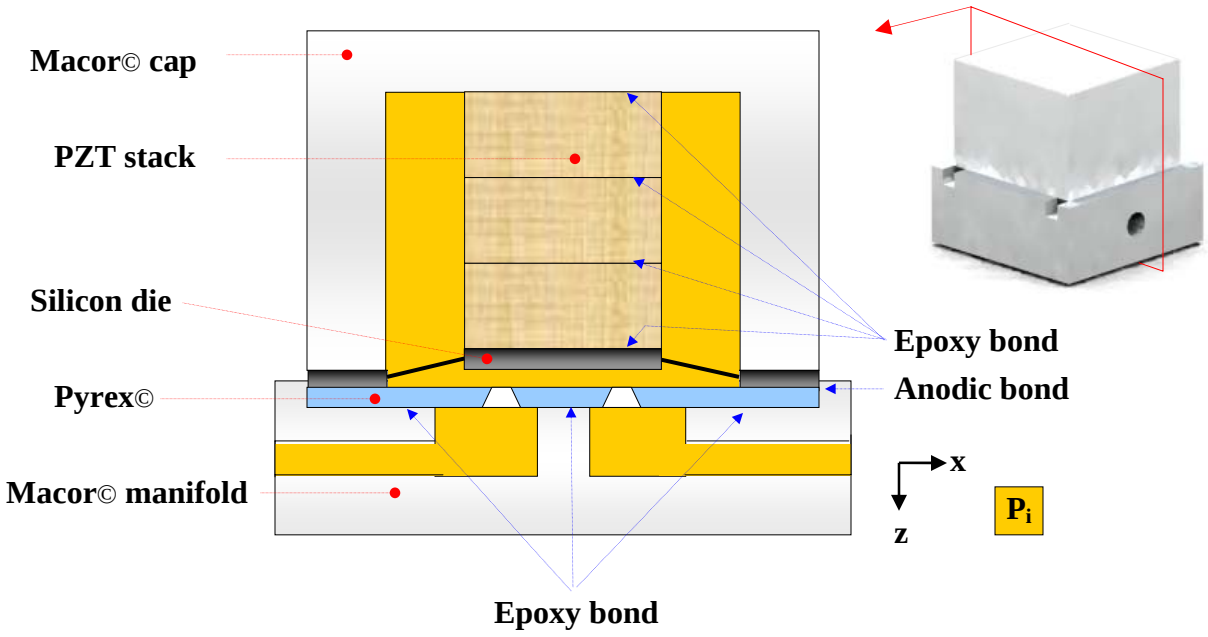

Figure 4.10: The micro valve assembly

A dimensioned drawing of Fig. 4.10 can be found in Appendix B. A finite element model of the valve assembly geometry shown in Fig. 4.10 was defined using CosmosWorks© software.

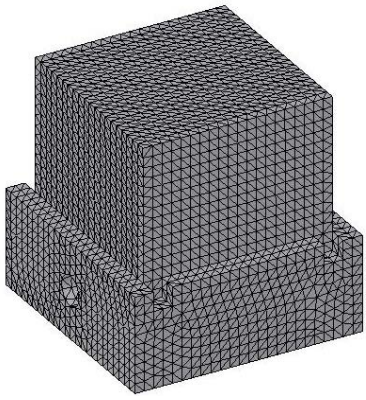

Figure 4.11: FE structural model mesh of the micro valve assembly

All of the epoxy bonds were assumed to have a thickness of 380.0 μm and the material properties derived in section 4.1. The room temperature material properties that were used to model the other materials in the valve assembly are summarized in Table 4.2.

Table 4.2: Structural properties for the valve materials

	Elastic Modulus (Pa)			**Poisson's Ratio**			**Shear Modulus (Pa)**		
	x	**y**	**z**	**xy**	**yz**	**xz**	**xy**	**yz**	**xz**
Macor©	6.69E10	n/a	n/a	0.29	n/a	n/a	2.55E10	n/a	n/a
Pyrex©	6.2E10	n/a	n/a	0.20	n/a	n/a	2.58E10	n/a	n/a
PZT	6.10E10	6.10E10	5.32E10	0.2	0.2	0.2	1.74E11	1.38E11	1.38E11
Silicon	1.3E11	n/a	n/a	0.28	n/a	n/a	5.09E11	n/a	n/a

All material properties for Table 4.2 were found at Efunda 2006. Macor© and Pyrex© are linear isotropic materials while the piezoelectric, Lead-Zirconate, is a linear orthotropic material. The bottom surface of the Macor© header was assumed to be rigidly fixed; all other boundaries were assumed free or bonded through the already specified epoxy or anodic bonds. A sample contour plot of the displacement distribution is shown in Figs. 4.12 and 4.13 for P_i=500.0 kPa.

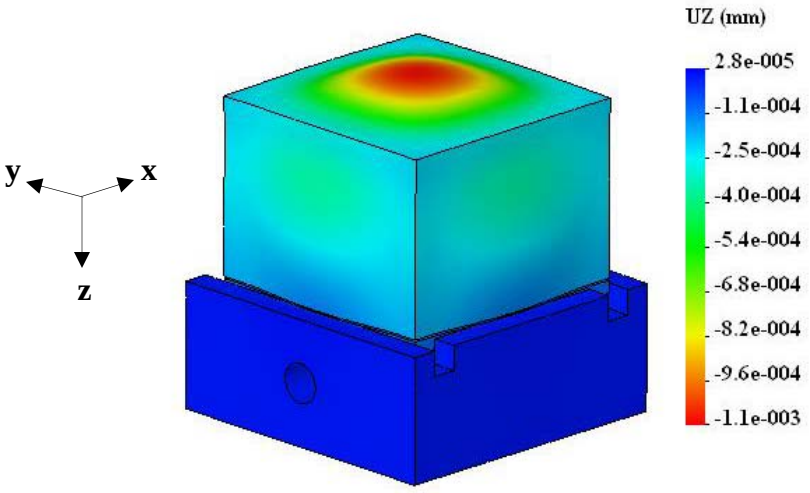

Figure 4.12: Exterior displacement distribution of the micro valve assembly with P_i=500.0 kPa

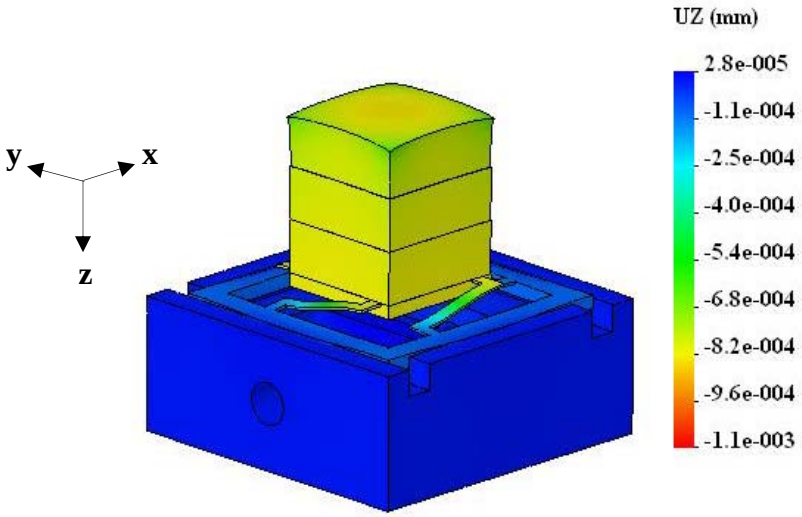

Figure 4.13: Interior displacement distribution of the micro valve assembly with P_i=500.0 kPa

The elemental grid size shown in Fig. 4.11 was selected by running the FE model for various grid sizes while holding the interior gage pressure constant. For each case the valve seat displacement was recorded and plotted to determine when convergence in the displacement had occurred; see Fig. 4.14 for the structural valve seat displacement as a function of average global element size for P_i=500.0 kPa

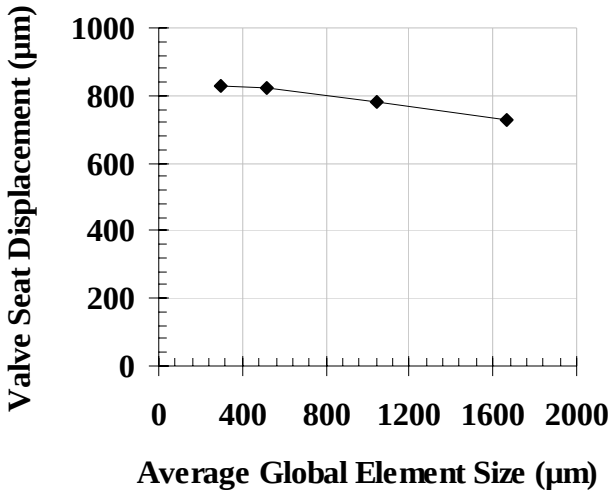

Figure 4.14: Structural valve seat displacement as a function of average global element size for P_i=500.0 kPa

The results from Fig. 14 suggest that an average global element size of 500 µm would allow convergence in the structural valve seat displacement. Using an average global element size of 500 µm, the full structural model was iterated over a wide range of the interior pressure, P_i. For each case the valve seat clearance was recorded. The room temperature structural analysis is summarized in Fig. 4.15.

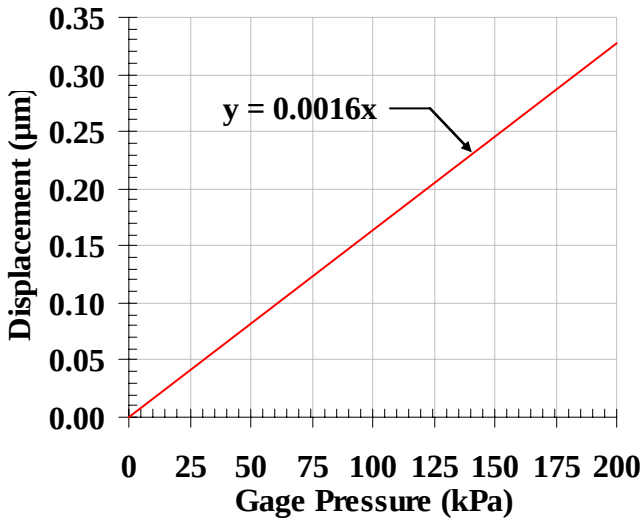

Figure 4.15: Valve seat clearance displacement from structural loading

The results of Fig. 4.15 are limited to the dimensions summarized in Appendix B, the materials listed above, and room temperature conditions. Figure 4.15 shows that an interior pressure, P_i, of 625.0 kPa is required to lift the valve seat by 1.0 μm which is sufficient to substantially affect the operation of the valve. However at lower pressure the structural displacement should have a limited effect on the valve seat clearance displacement.

4.4 Conclusion

The valve seat clearance structural displacement due to structural loading has been estimated using a finite element model. The properties of the numerous epoxy joints were estimated using the results of an experimental test coupled to an FE model. The results derived in the chapter are limited to a specific set of geometric values and room temperature operating conditions. However a method for determining the micro valve seat clearance structural displacement has been demonstrated which may be helpful for future studies.

4.5 References

http://www.efunda.com, 2006

Chapter 5

System Level Flow Modeling of the Micro Valve

5.1 Introduction

In preceding chapters, the governing equations and correlations required to model the individual components within the micro valve flow network were derived. It is useful at this point to summarize the individual components that make up the micro valve network and indicate the intended integration between these components that is required to create a complete system model. This integrated network is shown schematically in Fig. 5.1.

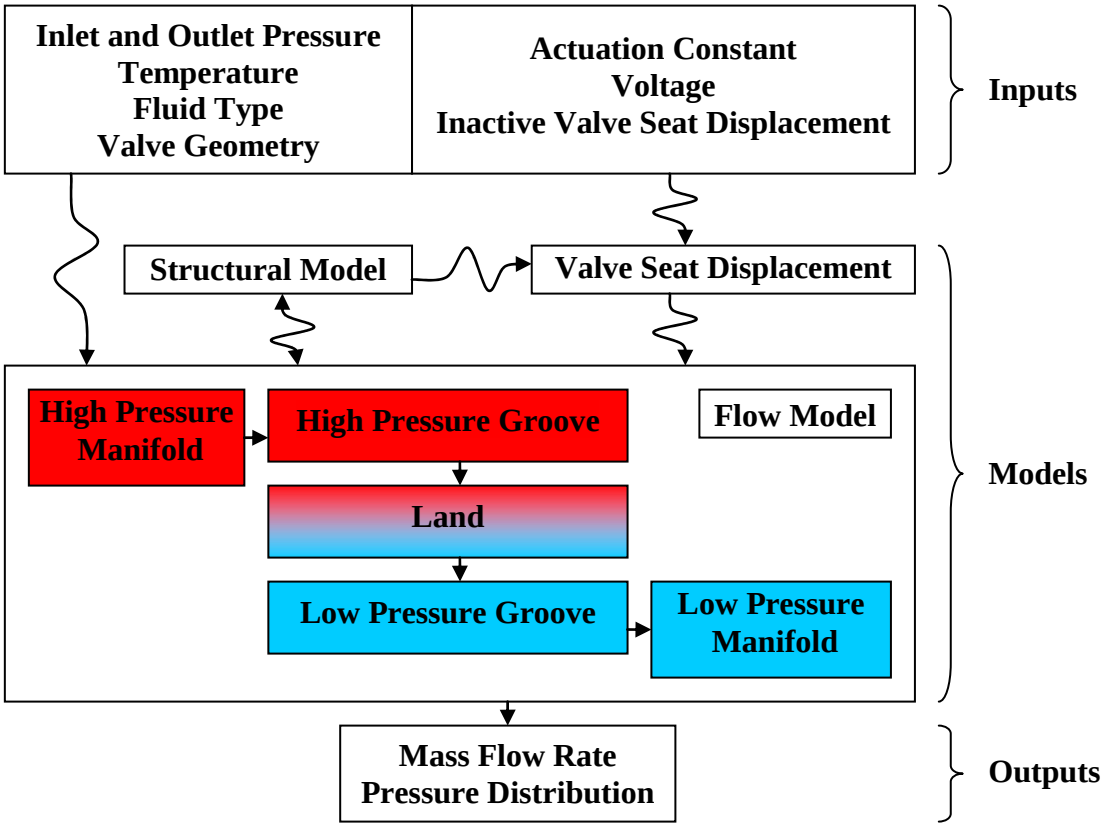

Figure 5.1: Schematic of the micro valve model

The application of the correlations for the groove and land require a new series of discretized equations because the form of the equations are different then those presented

in Chapter 2. In addition, a technique for coupling the manifolds and land-groove region discussed. With these modifications, it is possible to provide a complete model of the micro valve flow network. The model is implemented using the Engineering Equation Solver program (EES).

5.2 Discretized Form of the Land and Groove Correlations

The model is based on continuity applied to a differential control volume in the groove. The flows for the control volume are driven by pressure differences. A control volume over a differential segment of the high pressure groove is shown in Fig. 5.2 and leads to the continuity equation given by Eq. (5.1).

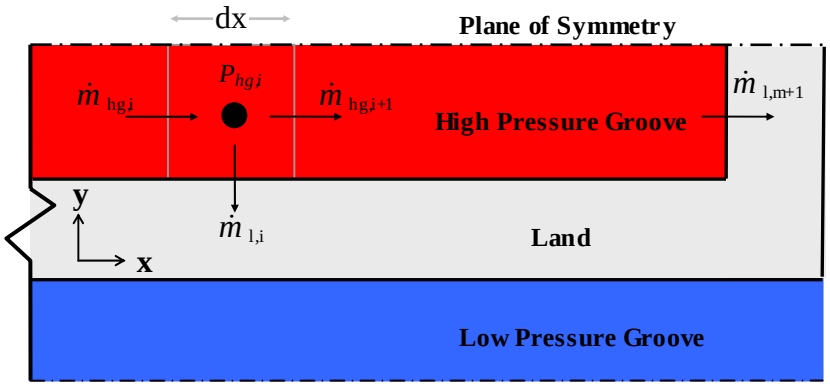

Figure 5.2: Mass balance terms for a differential control volume located in the high pressure groove

$$\dot{m}_{hg,i} = \dot{m}_{l,i} + \dot{m}_{hg,i+1} \tag{5.1}$$

The governing equation for the flow in the groove expresses the pressure drop in terms of a viscous loss and an inertial term, as discussed in Chapter 3. The governing equation is discretized according to:

$$\frac{P_{hg,i-1} - P_{hg,i}}{dx} = \frac{f_{hg,i}}{D_{h,hg}} \frac{\rho_{hg}}{2} V_{hg,i}^{\ 2} + \rho_{hg} V_{hg,i} \frac{dV_{hg,i}}{dx} \tag{5.2}$$

where the velocity, $V_{hg,i}$, is related to the mass flow rate according to:

$$V_{hg,i} = \frac{2\dot{m}_{hg,i}}{\rho_{hg} A_{c,hg}} \tag{5.3}$$

and the velocity gradient is discretized using a 3rd order upwind scheme:

$$\frac{dV_{hg,i}}{dx} = \frac{1}{dx}\left(-\frac{1}{6}V_{hg,i+1} + V_{hg,i} - \frac{1}{2}V_{hg,i-1} - \frac{1}{3}V_{hg,i-2} \right) \tag{5.4}$$

In Eqs. (5.2) through (5.4) the subscript *i* refers to position of the node and the subscript *hg* refers to the fact that the control volume is located in the high pressure groove. It was found, by trial and error, that lower order discretizations of the velocity gradient in the inertial term (e.g., first order downwind, second order central difference, etc.) did not result in numerically stable results. The friction factor, $f_{i,hg}$, in Eq. (5.2) was discussed in Chapter 3 and is calculated using correlations that were developed with the CFD model of the groove. The friction factor is evaluated by interpolating from a lookup table integrated with EES; the independent variable is the local Reynolds number based on hydraulic diameter at the nodal location *i*. The fluid properties required in Eqs. (5.2) through (5.4) are evaluated at the average of the maximum and minimum pressure for the high pressure groove.

There is an equivalent set of equations that characterize the low pressure groove. The flow across the land (i.e., the term $\dot{m}_{i,l}$ in Eq. (5.1)) is driven by a pressure difference between the high pressure groove ($P_{hg,i}$) and the pressure just inboard of the land ($P_{l,i}$); these pressure are different due an inertial loss associated with the contraction of the flow into the land. The inertial loss is assumed to occur over a negligibly small spatial extent and is represented by:

$$P_{hg,i} - P_{l,i} = K_{l,i} \frac{1}{2} \rho_{hg} V_{l,i}^{\ 2} \tag{5.5}$$

where $V_{l,i}$ is the mean flow velocity at the inlet to the land evaluated at the nodal location i:

$$V_{l,i} = \frac{\dot{m}_{i,l}}{\rho_{hg}\, \delta\, dx} \tag{5.6}$$

where δ is the gap height. The inertial coefficient, $K_{l,i}$, in Eq. (5.5) is based on correlating the CFD modeling results as discussed in Chapter 3. The inertial coefficient is evaluated in the system model by interpolating from a 2-D lookup table using the Reynolds number based on the local valve seat clearance and the ratio of valve seat clearance to groove height at the nodal location i. The lookup scheme uses two dimensional, second order interpolations for both variables. The lookup table is populated from the data obtained via the CFD simulation of the entrance effect.

It was shown in Chapter 2 that the two-dimensionality of the flow over the land has a small effect on its overall performance; however, the impact of slip and compressibility are quite important. Therefore, the flow across the land is assumed to be 1-D (perpendicular to the groove); therefore, the flow across the land at a nodal location i is driven by the pressure difference across the land at that same nodal location. The relationship between the mass flow rate and the pressure difference across the land includes the impact of slip and compressibility as developed in Chapter 2:

$$\dot{m}_{l,i} = \frac{\delta^3 \rho_{lg,i} P_{lg,i}\, dx}{24\, \mu_{lg,i}\, w_l} \left[\left(\frac{P_{l,i}}{P_{lg,i}} \right)^2 - 1 + 12 \sigma Kn_{lg,i} \left(\frac{P_{l,i}}{P_{lg,i}} - 1 \right) \right] \tag{5.7}$$

where the density and viscosity are evaluated at the low pressure groove nodal location *i* pressure and at the valve temperature, *T*. The Knudsen number, $Kn_{lg,i}$, is evaluated in the land using the low pressure groove nodal location *i* properties. In Eq. (5.7), *R* is the ideal gas constant of the fluid. Note in Eq. (5.7) that the pressure after the entrance inertial loss ($P_{l,i}$) is taken to be the high pressure while the pressure in the low pressure groove ($P_{lg,i}$) is taken to be the low pressure; therefore, the inertial pressure change associated with the expansion of the fluid into the low pressure groove is ignored. This method is consistent with the CFD modeling results discussed in Chapter 3.

The incompressible, no-slip form of Eqn. (5.7) is shown in Eq. (5.8) and can be used to investigate the effect of the compressibility and slip on the valve behavior.

$$\frac{P_{l,i} - P_{lg,i}}{w_l} = \frac{12\mu_{lg,i}\,\dot{m}_{l,i}}{\delta^3 \rho_{lg,i}\,dx} \tag{5.8}$$

The mass flow rate entering the high pressure groove, $\dot{m}_{hg,0}$, is evaluated using Eq. (5.2) expressed at node 1. Node 1 is longer than the other nodes within the groove because it includes w_{tip} (the tip width) as well as a half-node, *dx*/2.

$$\frac{P_{high} - P_{hg,1}}{w_{tip} + dx/2} = \frac{f_{hg,1}}{D_{h,hg}} \frac{\rho_{hg}}{2} V_{hg,1}{}^2 + \rho_{hg} V_{hg,1} \frac{dV_{hg,1}}{dx} \tag{5.9}$$

$$V_{hg,1} = \frac{2\,\dot{m}_{hg,1}}{\rho_{hg}\,A_{c,hg}} \tag{5.10}$$

$$\frac{dV_{hg,1}}{dx} = \frac{1}{dx}\left(V_{hg,2} - V_{hg,1}\right) \tag{5.11}$$

The term P_{high} is the pressure at the inlet to the high pressure groove. Note that P_{high} is not equivalent to the high pressure provided to the valve due to the additional pressure loss associated with the flow through the high pressure manifold.

The mass flow rate from the high pressure groove across the tip (i.e., the extent of the land that separates the high pressure groove from the low pressure manifold) is labeled $\dot{m}_{l,m+1}$ in Fig. 5.2 and is modeled using flow relations that are consistent with the flow across the land between the high and low pressure grooves. The inertial entrance loss is incurred between the pressure at the end of the high pressure groove ($P_{hg,,m}$) and the pressure just inboard of the tip ($P_{l,m+1}$).

$$P_{hg,m} - P_{l,m+1} = K_{l,m+1} \frac{1}{2} \rho_{hg} V_{l,m+1}^{\ 2} \tag{5.12}$$

$$V_{l,m+1} = \frac{2\dot{m}_{l,m+1}}{\rho_{hg}\ \delta\, w_g} \tag{5.13}$$

The flow across the tip is related to the pressures at either end of the tip according to:

$$\dot{m}_{l,m+1} = \frac{\delta^3 \rho_{low} P_{low}\, w_g}{48\,\mu_{low}\, w_{tip}} \left[\left(\frac{P_{l,m+1}}{P_{low}} \right)^2 - 1 + 12\sigma Kn_{low} \left(\frac{P_{l,m+1}}{P_{low}} - 1 \right) \right] \tag{5.14}$$

The incompressible, no slip form of Eq. (5.14) is shown in Eq. (5.15)

$$\frac{P_{l,m+1} - P_{low}}{w_{tip}} = \frac{12\mu_{low}\,\dot{m}_{l,m+1}}{\delta^3\, dx\, \rho_{low}} \tag{5.15}$$

All properties in Eq. (5.14) are evaluated at the pressure in the low pressure manifold, P_{low}, which, like P_{high}, is the pressure at the exit of the low pressure grooves. The low pressure applied to the valve is somewhat less that P_{low} due to losses within the low

pressure manifold. The boundary conditions for the low pressure groove have an equivalent form as those for the high pressure groove.

Figure 5.3 illustrates the flow (in terms of the non-dimensional mass flow rate) as a function of the Reynolds number in the land for the three dimensional Fluent© model (labeled 3-D Fluent model) discussed in Chapter 3 as well as the incompressible one dimensional model of a single land and groove developed above (labeled correlated 1-D flow model) and the uncorrelated two dimensional model developed in Chapter 2. In order to generate Fig. 5.3, the tip was assumed to be ideal in that it occupied a negligibly small width (and therefore $P_{high}=P_{hg,1}$ and $P_{low}=P_{lg,m}$) yet completely eliminated the mass flow rate over the tips (therefore, $\dot{m}_{l,m+1}$ and $\dot{m}_{l,0}$ are assumed zero); this was necessary to provide a consistent operating condition among the models because the fluent model did not include the effects of the tip. Also, fluid properties were assumed to be spatially constant.

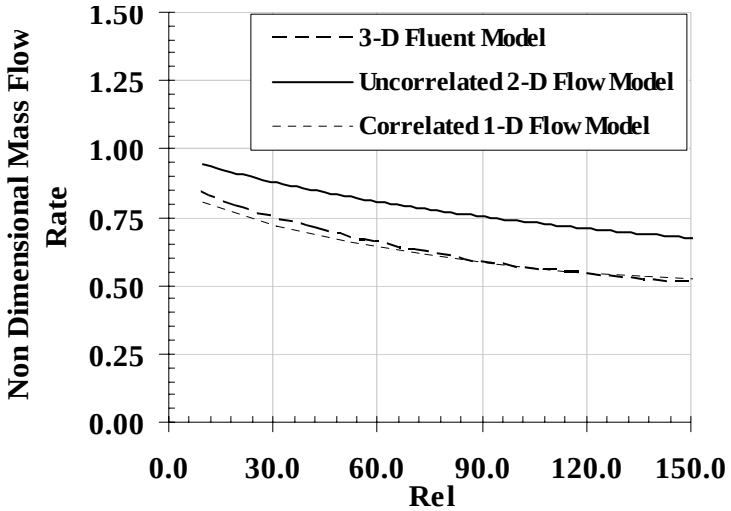

Figure 5.3: Comparison between the 2-D incompressible no-slip flow model, 1-D incompressible correlated model, and the 3-D Fluent© model for F_{geom}=3.0, and the input parameters from Table 5.1

Table 5.1: Nominal conditions used for Fig. 5.3

Variable	Value	Dimension
l_g	2000.0	μm
d_g	115.0	μm
w_g	200.0	μm
δ	5.0	μm
w_l	50.0	μm
μ	2.0e-5	kg-m/s
ρ	1.0	kg/m^3
P_{low}	0.0	kPa
m	30.0	

Figure 5.3 shows that it is possible to produce nearly equivalent results as the three dimensional fluent model, which can require thirty minutes to run, using the correlated one dimensional model, which requires seconds to run.

5.3 Coupling of the Manifolds to the Land/Groove Region

This section describes the coupling between the manifolds and the discretized form of the governing equations for the land and grooves, derived in the previous section. Chapter 3 presented CFD models of the manifolds and it was shown that the pressure drop in the high pressure manifold (ΔP_h) can be expressed using the functional form:

$$\Delta P_h = \frac{1}{2} K_h \rho_h V_h^2 \tag{5.16}$$

$$V_h = \frac{\dot{m}_h}{\rho_h \frac{\pi}{4} d_2^2} \tag{5.17}$$

See Chapter 3 for definition of the variables in Eqs. (5.16) and (5.17). For an inertially dominated flow regime, which is expected for operation at cryogenic temperatures, the pressure variation through the rectangular manifold section is small compared to the total pressure drop in the manifold. In addition, we saw that solutions for the inertial loss

coefficient K_h obtained using a constant pressure boundary condition applied at the groove entrances were equivalent to the solutions obtained using the more realistic boundary condition where a uniform distribution of flow is applied to the groove entrance. These observations combine to allow the assumption that the inlet pressure to the high pressure grooves and exit pressure from the low pressure grooves are single uniform values in the manifold (P_{high} and P_{low}). Therefore the term ΔP_h can be written as:

$$\Delta P_h = P_{inlet} - P_{high} \tag{5.18}$$

In Eq. (5.18) the term P_{inlet} represents the inlet pressure into the valve. The term, $\dot{m}_h$, in Eq. (5.17) represents the mass flow rate for the entire valve and can therefore be related to the mass flow rate in the land and groove region as follows:

$$\dot{m}_h = N_l \left(\dot{m}_{hg,0} + \dot{m}_{l,0} \right) \tag{5.19}$$

where N_l is the number of lands in the valve. The fluid properties for Eqs. (5.16) and (5.17) are evaluated at the average of P_{inlet} and P_{high}. To further justify Eqs. (5.18) and (5.19), it will be shown in chapter six that the manifolds represent a small fraction of the total pressure drop across the valve. The integration of the low pressure manifold with the system model is accomplished using an equivalent process.

The structural model described in Chapter 4 is coupled to the system model by assuming the input pressure to the model as the average of P_{high} and P_{low}. The structural model calculates the increase in the seat displacement using the average pressure and the solution presented in Chapter 4. The seat displacement is then calculated as the sum of the initial seat displacement, increase due to structural loading, position due to acuation:

$$\delta = \delta_o + \delta_s - \delta_v \tag{5.20}$$

where:

$$\delta_v = V\left(A_c\right) \tag{5.21}$$

In Eq. (5.20) δ is the seat displacement, δ_o is the initial seat displacement, δ_s is the structural seat displacement, and δ_v is the seat displacement from voltage actuation. In Eq. (5.21) V is the voltage, and A_c is the actuation constant.

5.4 Conclusion

By using the correlations and governing equations developed in Chapters 2 and 3, a flow model that includes the effects of all of the components within the valve has been developed. The incompressible, no-slip form of the model has been shown to predict results that are consistent with an incompressible, three dimensional Fluent© model. The incompressible form of the model for a single land and groove has a run time of approximately 15.0 seconds using EES, while the incompressible three dimensional Fluent© model requires approximately 30.0 minutes to obtain convergence on a single processor, P4 3.8GHZ, computer. The model developed in chapter five will be useful for design and optimization purposes because of its fast run time and accuracy. A listing of the compressible code is given in Appendix C. To better validate the accuracy of the model developed in chapter five, experimental data from a prototype micro valve will be presented and compared with the model predictions in Chapter 6.

Chapter 6

Experimental Results and Model Comparison

6.1 Introduction

Previous chapters have focused on developing the micro valve flow model. This effort concluded in Chapter 5 with the presentation of a system level model that incorporates the governing equation for compressible, slip flow across the land with correlations based on CFD models for the flow through the groove and the inertial losses at the inlet to the land and across the manifolds. Chapter 6 will digress from the modeling and will instead focus on experimental results obtained using prototype micro valves. The measurements taken at room temperature and cryogenic temperature will be presented. The experimental flow measurements are compared with the model predictions to verify the modeling work that was the primary objective of this thesis.

6.2 Micro Valve Fabrication

The actively controlled micro machined cryogenic valve project is a joint effort involving the Solid-State Engineering Lab (SSEL) at the University of Michigan-Ann Arbor, the Solar Energy Lab at the University of Wisconsin-Madison, and the Cryogenics Group at NASA-Ames. The SSEL at the University of Michigan-Ann Arbor is responsible for the manufacturing work associated with the project.

At the SSEL, micro machining of the silicon wafer containing the grooves and manifold is accomplished through deep reactive ion etching, as described by Park et al. (2006).

The micro machined silicon wafers are joined with the Pyrex substrate through an anodic bonding process. The manufacturing process results in a consistent and precise geometry for the land and groove region; see Fig. 6.1.

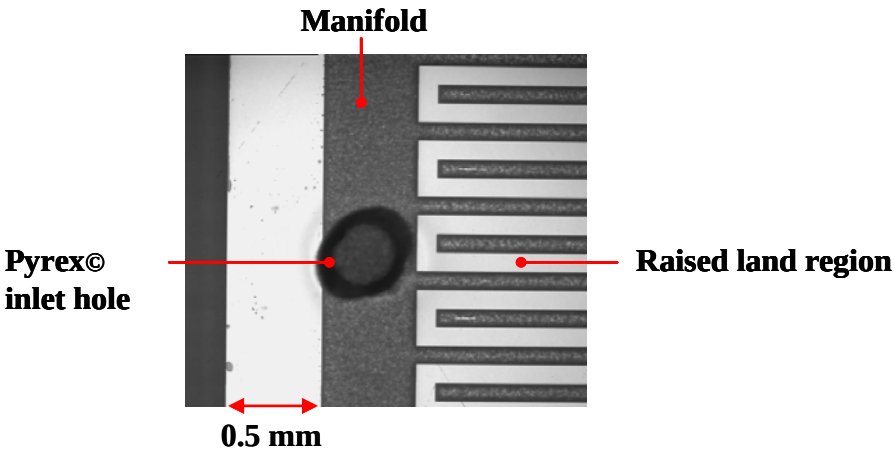

Figure 6.1: Top view a micro machined silicon/Pyrex© assembly

The silicon and Pyrex© assembly is epoxied to the Macor cap, PZT stack, and Macor manifold using Stycast© 2850 FT epoxy in a manual assembly process. Figure 6.2 illustrates the finished assembly of a prototype micro valve.

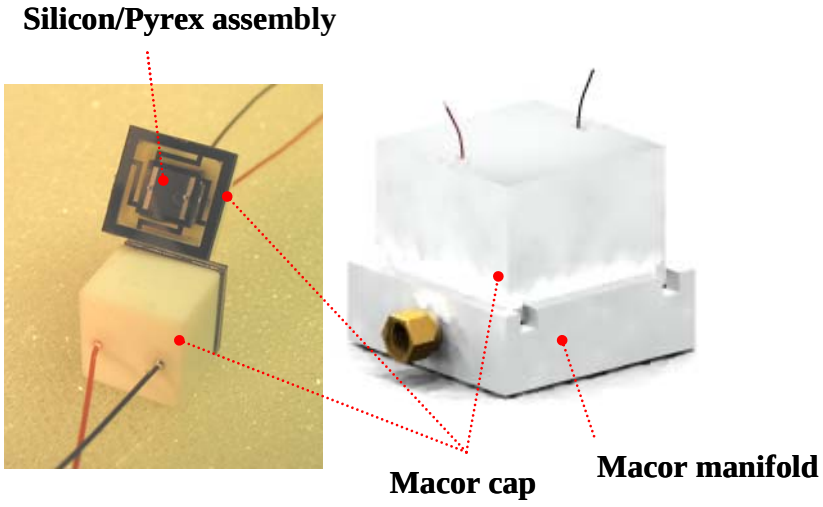

Figure 6.2: Micro valve assembly

A Swagelok© fitting is joined to the Macor manifold, see Fig. 6.2, for ease of plumbing. One can also see in Fig. 6.2 that the electrical leads required to energize the PZTs pass through the Macor cap and are sealed by an epoxy joint. The micro valve is assembled with the PZTs actuated at 100 Vdc and the valve plate pressed firmly against the valve seat. Therefore, the valve is normally open as reducing the voltage will cause the PZTs to contract and allow the valve plate to move away from the seat. The manual assembly process does not, at this point, produce repeatable results in that the zero-voltage valve clearance is not consistent between valves.

6.3 Experimental Flow Measurement

6.3.1 Room Temperature Flow Measurement

The relative simplicity of testing a micro valve under room temperature conditions made it an attractive option to obtain experimental flow data. Also, room temperature testing removed the distortions associated with thermally induced motion of the structure and PZTs; as these distortions are not completely understood (they have been modeled at a 1^{st} order level but not precisely, see Taylor (2005)) the cryogenic testing introduces an additional level of uncertainty to the results and makes it more difficult to compare the measurements to modeling results.

A simple test setup was constructed to allow room temperature flow measurements to be taken over a range of inlet pressures and actuation voltages. The test setup, shown schematically in Fig. 6.3, provided a constant outlet pressure of 0.0 kPa.

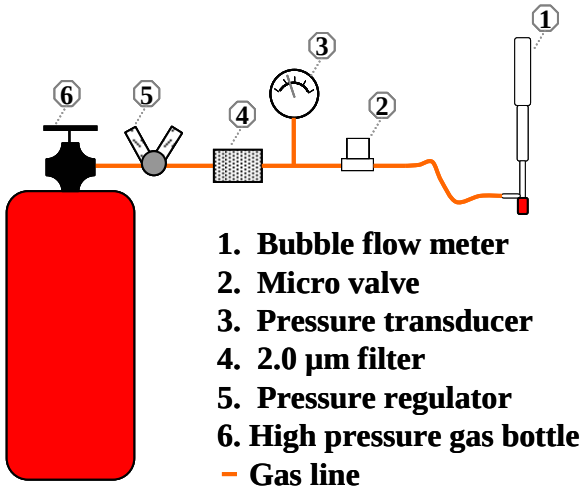

Figure 6.3: Room temperature flow testing schematic

A triple stage (1.0 ml, 10.0 ml, 100.0 ml) manual bubble flow meter, shown in Fig. 6.4, was used to measure flow because of its high accuracy over a wide range of flow rates. One disadvantage of using the bubble flow meter is the difficulty in quantifying error. This is because the flow measurement error is dependent upon the skill and attentiveness of the operator taking the measurement.

Figure 6.4: Bubble flow meter used for flow measurement

Room temperature flow measurements were obtained for four prototype micro valves; in some cases the valve operation was not adequate for comparison with the model. For brevity, room temperature flow measurements will be presented for the valve which had the highest degree of flow modulation capability; valve -00. In contrast to the standard micro valve design, see Fig. 6.5, valve -00 was mounted on a large aluminum manifold, and many of the epoxy joints were made using Devcon© epoxy.

Figure 6.5: Side and top view of valve -00, used for room temperature flow measurement

Valve -00 has the nominal dimensions shown in Table 6.1.

Table 6.1: Dimensions of Valve -00

Variable	Description	Value
l_g	Groove length	2000.0 μm
d_g	Groove depth	110.0 μm
w_g	Groove width	50.0 μm
w_l	Land width	50.0 μm
$A_{c,g}$	Groove cross sectional area	5.5e-8 m^2
per_g	Groove perimeter	320.0 μm
N_l	Number of lands	39

Because Devcon© epoxy was used, the lower temperature limit of valve -00 is approximately 230.0 K; therefore, it was not possible to obtain flow measurements at cryogenic temperature.

Several gases were used to test valve -00 in order to obtain the largest possible range of flow conditions and therefore demonstrate the fidelity of the model; these gases include helium, argon, nitrogen, and sulfur hexafluoride. For each test gas, the inlet flow from a high pressure bottle was throttled to a pressure of between 0.0 and 100.0 kPa and measurements were taken over a range of actuation voltage; see Fig. 6.6 for an example of the data taken using helium.

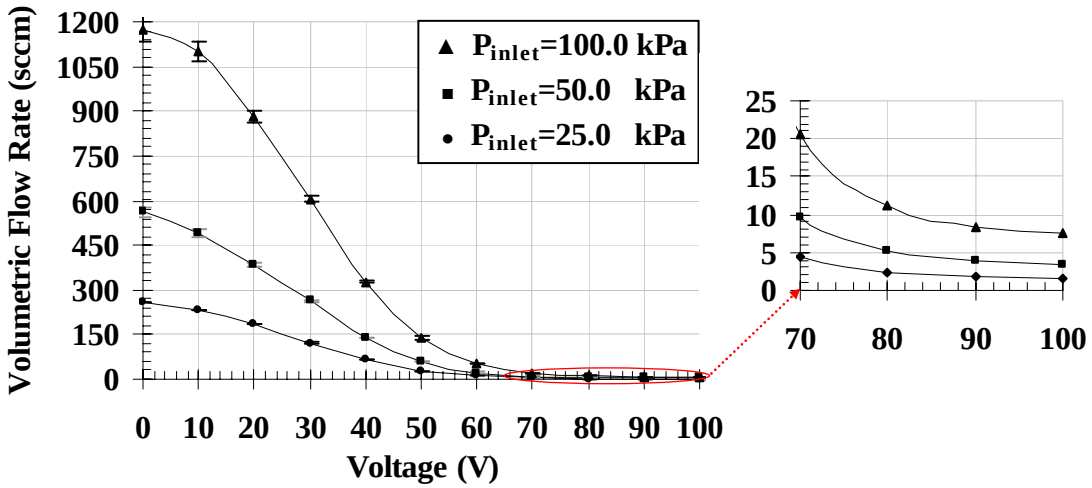

Figure 6.6: Experimental helium flow data of valve -00

The error bars reported in Fig. 6.6 are calculated by assuming an error in the recorded bubble flow meter time of ±0.2 seconds, which is nominally consistent with the reaction time of an operator. The error in the recorded pressure was ±2.0 kPa and the error in actuation voltage was negligible. One interesting aspect of the data shown in Fig. 6.6 is that the flow rate is a nearly linear function of the pressure drop for a given actuation voltage, as shown in Fig. 6.7; this suggests that the bulk of the pressure drop occurs across the lands and is related to a viscous shear.

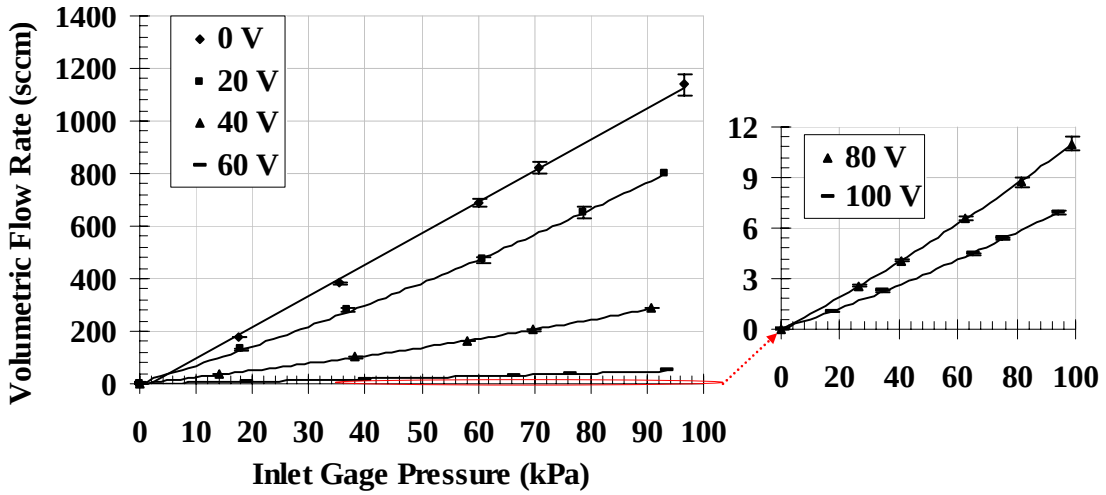

Figure 6.7: Experimental helium flow data of valve -00

Room temperature results for other test gases are shown in Figs. 6.8-6.10.

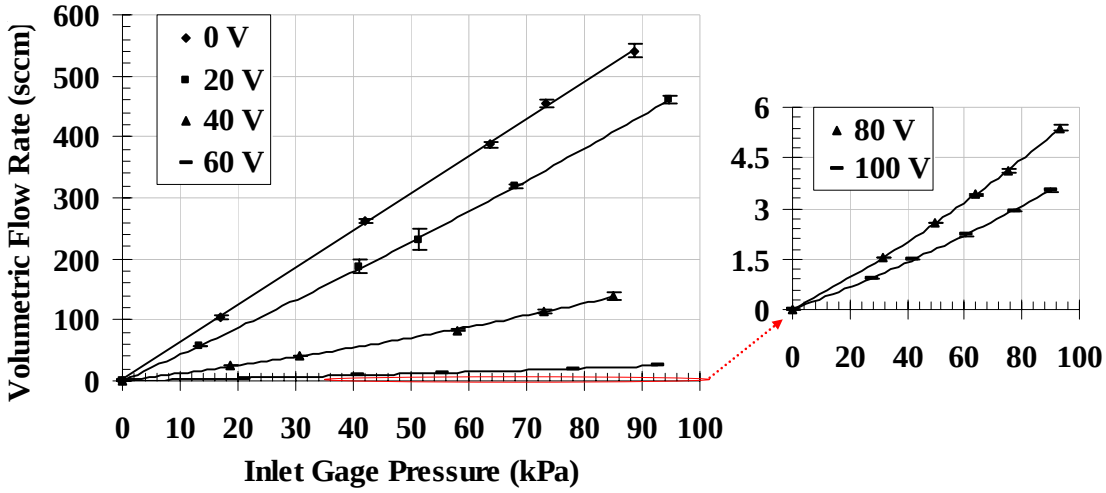

Figure 6.8: Experimental argon flow data of valve -00

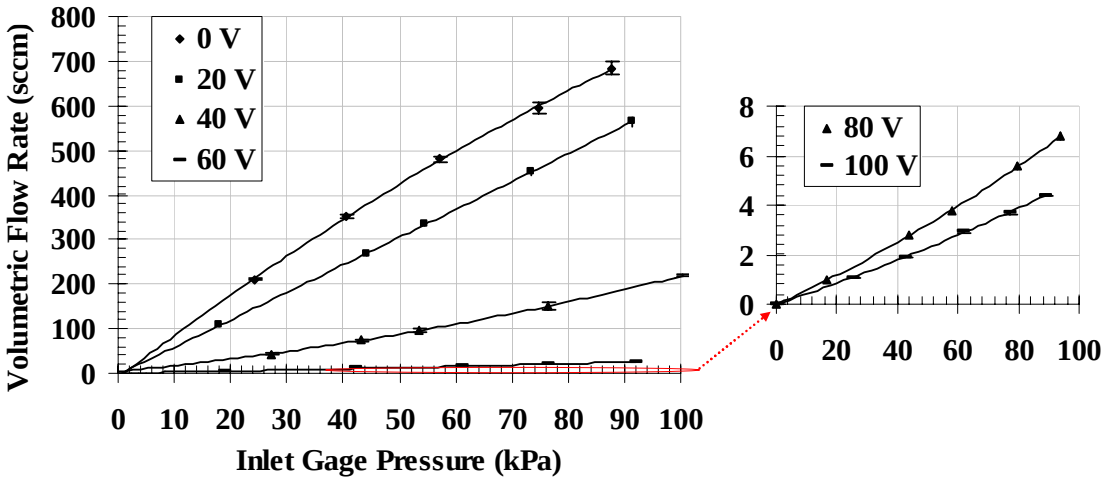

Figure 6.9: Experimental nitrogen flow data of valve -00

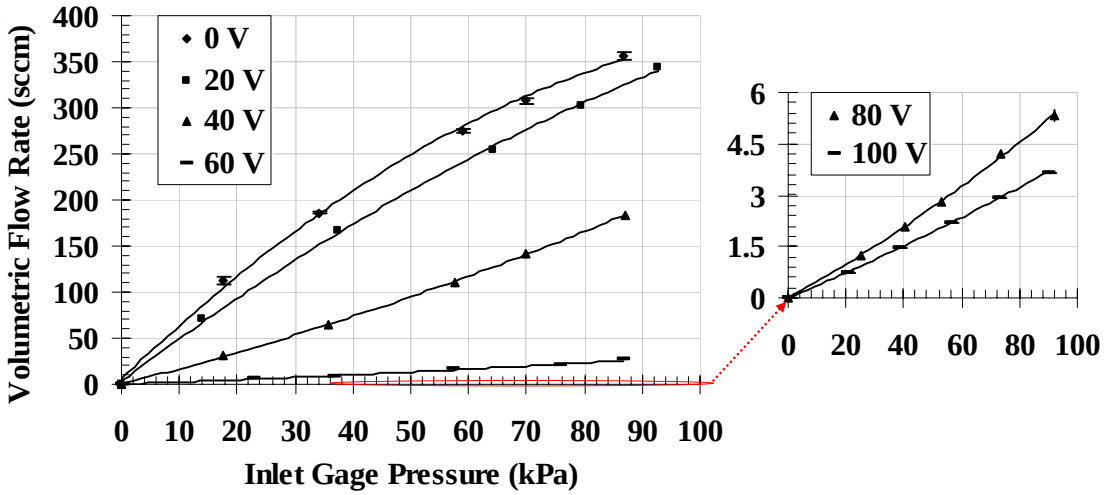

Figure 6.10: Experimental sulfur hexafluoride flow data of valve -00

6.3.2 Non Dimensional Room Temperature Flow Measurement Data

In Chapter 2, a set of non-dimensional numbers were presented in an attempt to characterize the flow in a single land and groove using a minimal set of parameters. Using the experimental room temperature data presented above, the success of the non dimensional parameters can be directly evaluated. The non dimensional numbers derived

in Chapter 2 are repeated in Eqs. (6.1) through (6.4). In this analysis the mass flow rate term in Eqn. (6.3) is assumed to be total mass flow rate measured for the micro valve.

$$Re_{land} = \frac{(P_{high} - P_{low})\delta^4 \rho}{\mu^2 w_l^2} \tag{6.1}$$

$$F_{geom} = \frac{l_g^2 \, K \, per_g^2 \, \delta^3}{w_l \, A_{c,g}^2} \tag{6.2}$$

$$\bar{\dot{m}} = \frac{\dot{m}}{N_g \; \dot{m}_{characteristic}} \tag{6.3}$$

$$\dot{m}_{characteristic} = \frac{\left(P_{high} - P_{low}\right)\delta^3 \, l_g \, \rho}{12 \, \mu \, w_l} \tag{6.4}$$

The non-dimensional numbers were derived using a characteristic mass flow rate that is based on incompressible, no-slip flow in the land and ignores inertial losses; this is a simplification relative to the more realistic compressible and slip behavior in the land, which was described in Chapter 2, and the significant inertial terms discussed in Chapter 3. Because of these inconsistencies, it is expected that the non dimensional numbers will not provide a perfect correlation for the experimental data.

To non-dimensionalize the experimental flow data, all three of the non-dimensional numbers, Eqs. (6.1) through (6.3), require that the seat clearance, δ, be known. However, it is not possible to measure the seat clearance during the experimental flow tests; the seat clearance can only be inferred based on the experimental data, as discussed in subsequent sections. For valve -00 it was found that an appropriate estimate for the 0 V valve seat clearance is 3.80 μm. Using this result together with an estimated actuation constant of 0.0525 μm/V (which is within the range of the manufacturer's specifications for the PZT actuators), the valve seat clearance can be expressed approximately as:

$$\delta(V) = 3.80 - .0525(V) \ (\mu m) \qquad (6.5)$$

where the pressure induced distortion of the valve has been ignored.

By using Eqn. (6.5), and evaluating the fluid properties for Eqs. (6.1) through (6.4) at the average of the valve inlet and exit (101.0 kPa) pressure, the experimental flow data for valve -00 can be presented in non-dimensional form. With an actuation voltage of 0.0 V, the non-dimensional form of the experimental data collapses quite well to a single curve for all of the test gases as shown in Fig. 6.11.

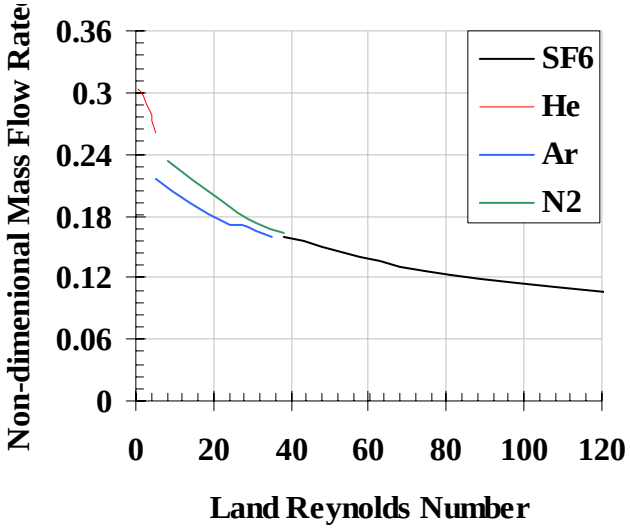

Figure 6.11: Non-dimensional mass flow rate as a function of the land Reynolds number using the experimental room temperature flow data from valve-00 at 0.0 V.

At higher applied voltages, which correspond to smaller valve clearances and therefore lower flow rates, the non-dimensional helium data begins to separate from the other gas data which form a flat curve, as shown in Fig. 6.12 and 6.13

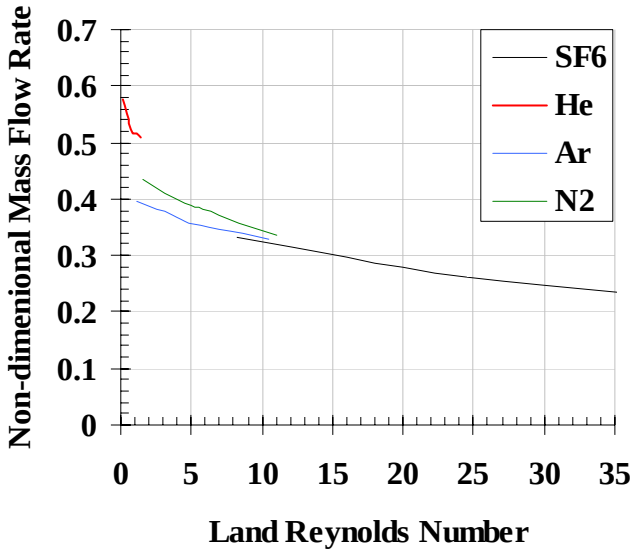

Figure 6.12: Non-dimensional mass flow rate as a function of the land Reynolds number using the experimental room temperature flow data from valve-00 at 20.0 V.

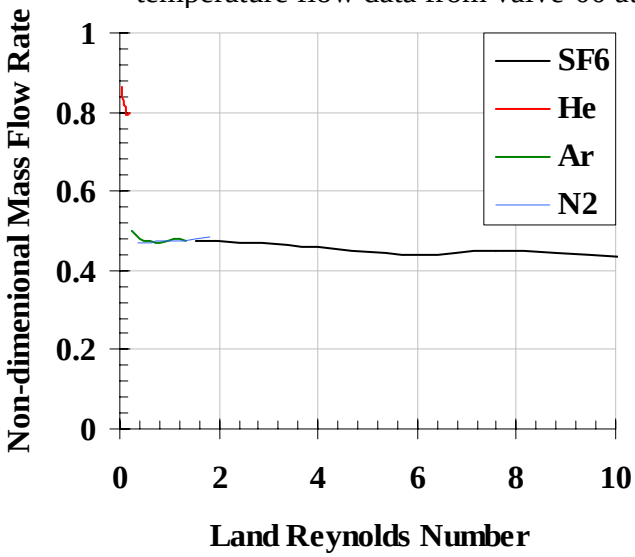

Figure 6.13: Non-dimensional mass flow rate as a function of the land Reynolds number using the experimental room temperature flow data from valve-00 at 40.0 V.

The relationship demonstrated in Fig. 6.13 is consistent with the data obtained at even higher applied voltages; the separation between the helium curve and the remaining flat curve continues to increase with higher voltages. It is likely that the non-dimensional helium curve departs from the other non-dimensional curve with increasing voltage

because with an increasing voltage compressible and slip-effects become ever more increasingly important and these effects have a substantially greater effect in the micro valve when using helium as the test gas. Further, it is likely that leakage around the valve becomes a more significant effect at higher voltages; helium is likely to leak more significantly than the other gases.

The fact that the remaining non-dimensional curves collapse to a single flat curve suggests that at high actuation voltages the total pressure drop is being governed entirely by viscous loss in land, which is what one would expect.

6.3.3 Cryogenic Temperature Flow Measurement

The micro valve design is required to operate at cryogenic temperatures and it is therefore important to conduct flow tests at reduced temperatures. This section will establish the low temperature capability of a prototype micro valve operating at liquid nitrogen temperatures.

A test setup similar to the room temperature schematic shown in Fig. 6.2 was constructed in order to allow low temperature flow measurements of helium gas to be taken over a range of inlet pressures and actuation voltages. The test setup, shown schematically in Fig. 6.14, provided a constant outlet pressure of 0.0 kPa.

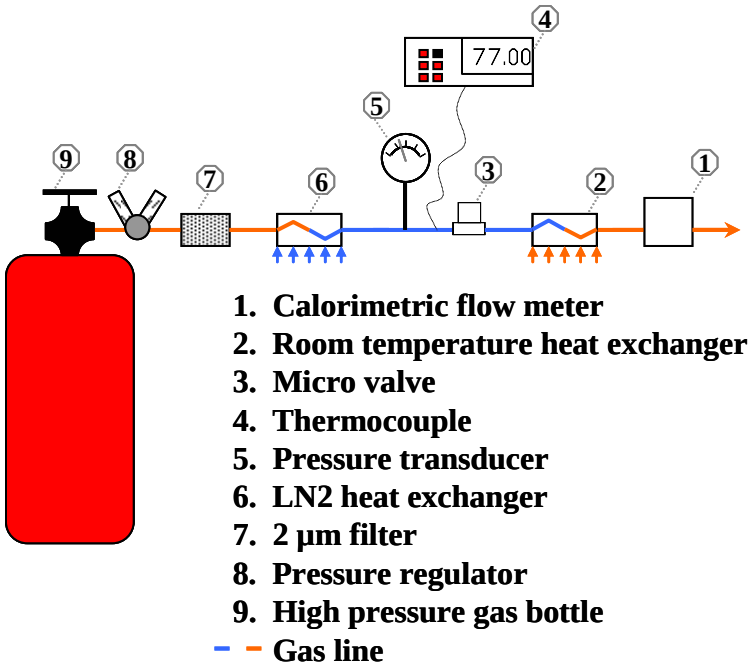

Figure 6.14: Low temperature flow testing schematic

The micro valve was thermally isolated from the room temperature environment by placing it in a dewar at a position that is just above the surface of a pool of liquid nitrogen, see Fig. 6.15.

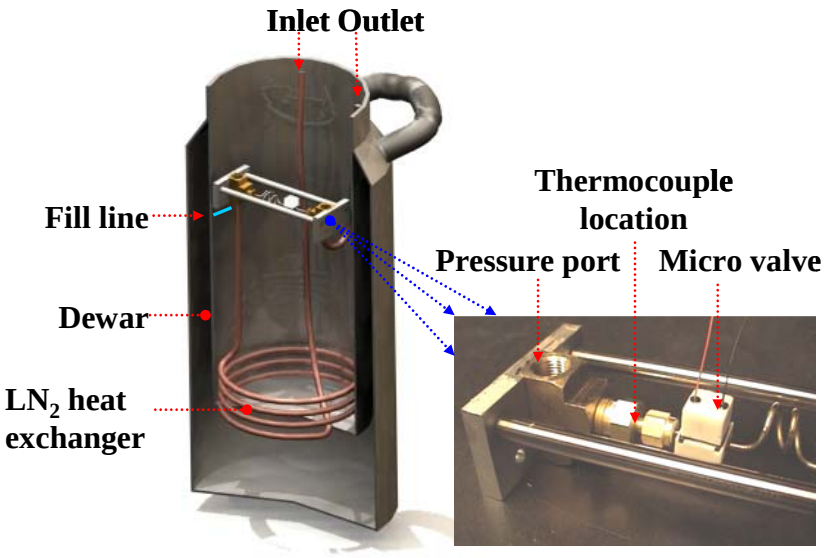

Figure 6.15: Cut away view of the low temperature flow testing hardware

A prototype micro valve, valve -03, was constructed using Stycast© epoxy and a macor manifold; therefore, valve -03 was capable of operating at cryogenic temperatures. Valve -03 is shown in Fig. 6.16; the coiled portion of the tube extending from the right side of the valve is meant to reduce the mechanical stresses imposed on the valve due to structural distortions of the mounting hardware.

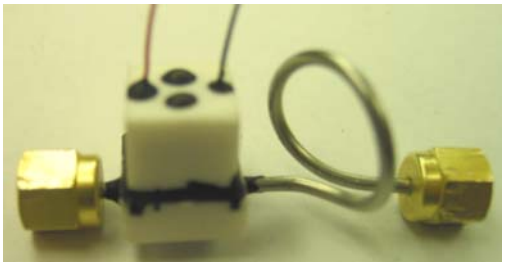

Figure 6.16: Valve -03, used for low temperature flow measurement

The dimensions of valve -03 are summarized in Table 6.2 and are slightly different from the dimensions of valve -00.

Table 6.2: Dimensions of Valve -03

Variable	Description	Value
l_g	Groove length	2000.0 µm
d_g	Groove depth	110.0 µm
w_g	Groove width	50.0 µm
w_l	Land width	100.0 µm
$A_{c,g}$	Groove cross sectional area	5.5e-8 m^2
per_g	Groove perimeter	320.0 µm
N_l	Number of lands	26

Using helium gas, the inlet flow was throttled from a high pressure bottle to a pressure between 0.0 and 100.0 kPa; measurements were taken over a range of actuation voltage as shown in Fig. 6.17.

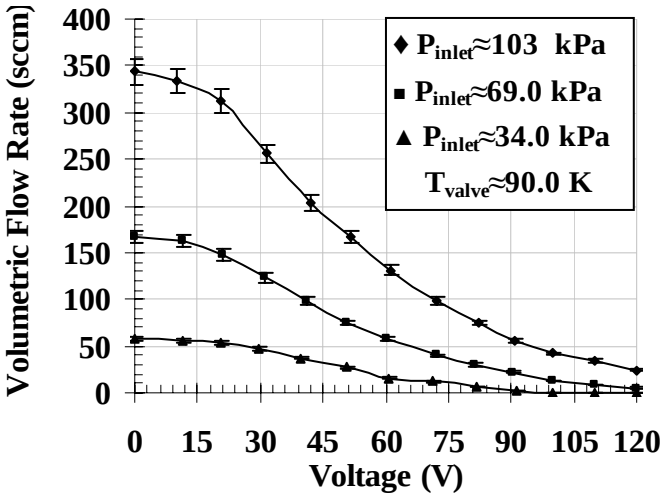

Figure 6.17: Experimental low temperature helium flow data of valve -03

Figure 6.17 shows that the micro valve is capable of modulating the flow rate at reduced temperature. The relationship between voltage and flow rate for the cryogenic test data has a similar relationship as the room temperature data; see Fig. 6.6. However, the relationship between pressure drop and flow rate for the cryogenic test data is not as linear as for the room temperature testing, see Fig. 6.18. This is because the viscous effects are reduced (viscosity drops at the lower temperature) while the inertial effects are increased (density increases at the lower temperature).

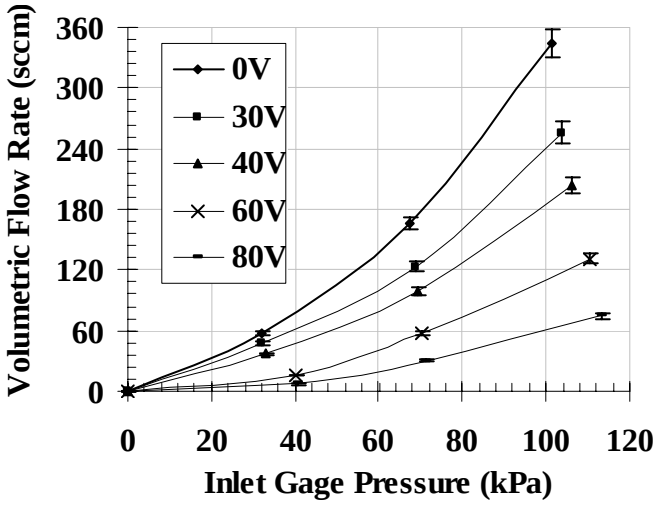

Figure 6.18: Experimental low temperature helium flow data of valve -03

The room temperature experimental helium results of valve -03 are shown in Fig. 6.19.

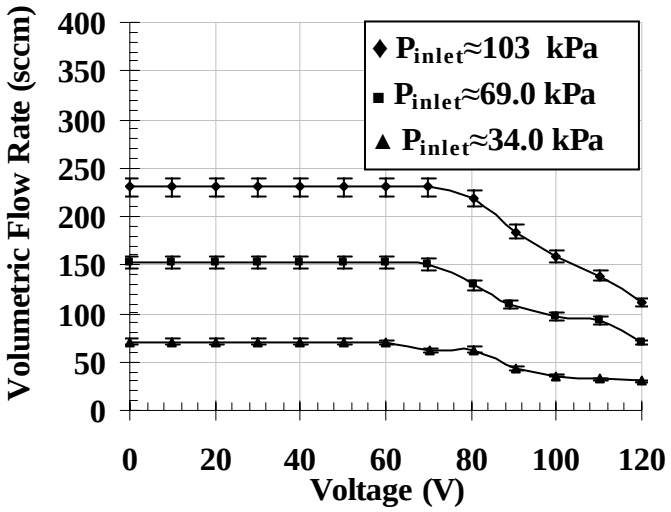

Figure 6.19: Experimental room temperature helium flow data of valve -03

Figure 6.19 shows that valve -03 was largely incapable of flow modulation at room temperatures even though it performed adequately at cryogenic temperatures. It is believed that thermal contraction of the valve structure reduced the initial valve seat clearance to a value in which flow modulation in valve -03 was possible at low temperatures. The discrepancy between the performance of valves -00 and -03 demonstrate the manual assembly process must be improved in order to obtain a consistent behavior from valve-to-valve.

6.4 Comparison of Experimental and Predicted Data

6.4.1 Room Temperature Data Comparison

Using the large amount of room temperature flow data presented in the preceding section allows the accuracy of the flow model to be evaluated. As mentioned above, the initial valve seat clearance and actuation constant cannot be known exactly for any valve after assembly. However, suitable values can be obtained using an iterative process in which

these constants are changed and the resulting model predictions are compared to the experimental data. In effect, this corresponds to fitting the results using two undetermined constants. However, the results obtained using single values of the initial clearance and actuation constant are accurate over a wide range of operating conditions. This process resulted in estimation for the initial valve seat clearance to be 3.80 μm and the actuation constant to be 0.0525 μm/V. These estimated constants are within the range of the manufacturer's specifications and realistic values. Figure 6.20 demonstrates the flow models prediction of the data from Fig. 6.6 using the estimated parameters.

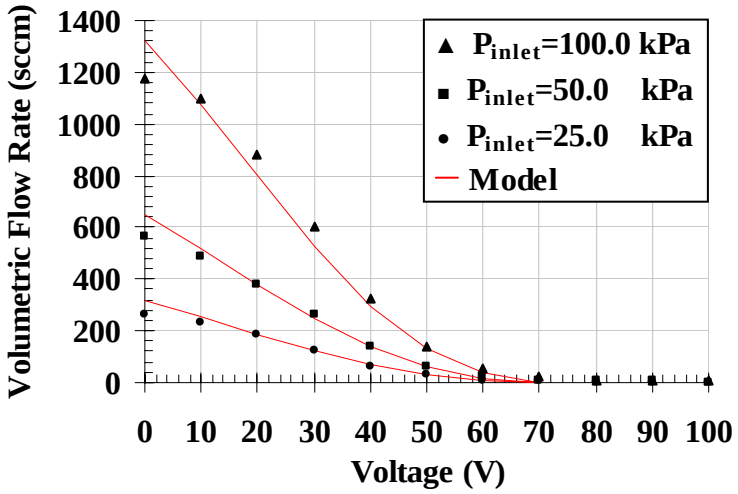

Figure 6.20: Model predictions of Fig. 6.5 data

Figures 6.21 and 6.22 illustrate the predicted flow rate as a function of the measured flow rate for each experimental data points that were taken with valve -00 in the range of 0-60 V; Fig. 6.22 focuses on the lower flow rate data from Fig. 6.21.

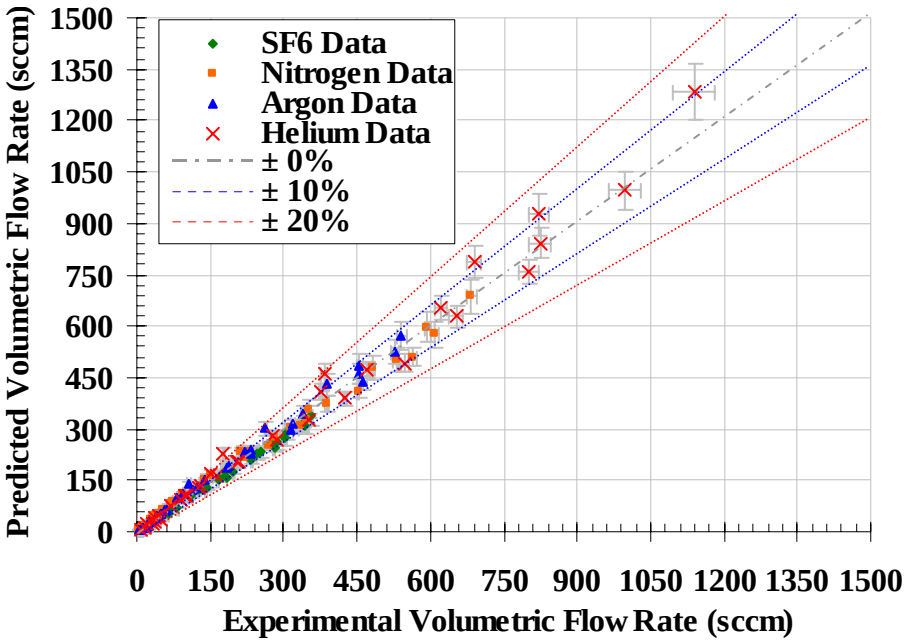

Figure 6.21: Predicted vs. experimental data for valve -00

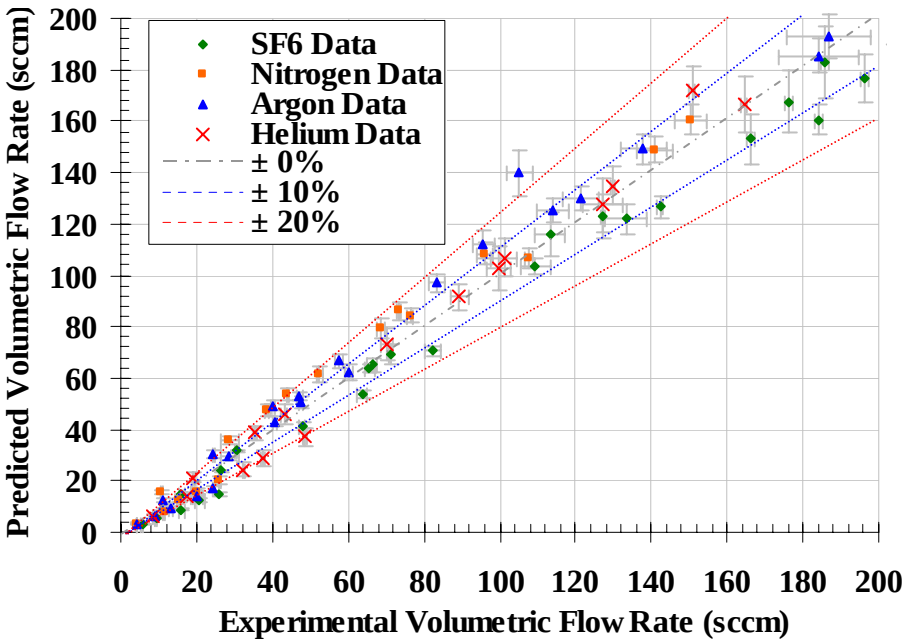

Figure 6.22: Predicted vs. experimental data for valve -00 at the low flow rates.

The y-error bars shown in Figs. 6.21 and 6.22 are calculated by assuming an uncertainty in the nominal values of the variables that are shown in Table 6.3 and applying this

uncertainty to the model in order to evaluate the associated change in the predicted flow rate.

Table 6.3: Sources of predicted error

Variable	Description	Nominal Value	Error
σ	Tangential momentum coefficient	0.825	±0.125
d_q	Groove depth	110 μm	±10.0 μm
P_{inlet}	Inlet pressure	n/a	±1.0%

The x-error bars are calculated assuming an error of ±0.2 seconds in the recorded bubble flow meter time. At higher voltages and lower flow rates it becomes more difficult to predict the data with a low relative uncertainty. Figure 6.23 illustrates the the percentage of the total data shown in Figs. 6.21 and 6.22 that lie within a given relative uncertainty range; the 0-40 V data can be predicted more accurately than the 0-60 V because of the higher flow rates.

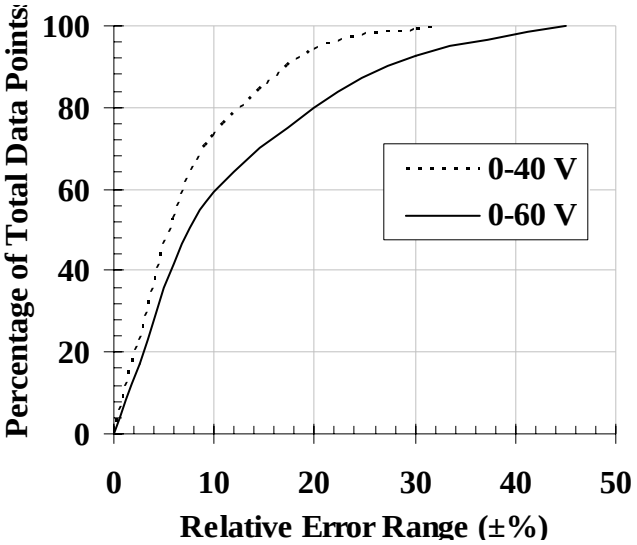

Figure 6.23: Percentage of the total data points from Figs. 6.21 and 6.22 which lie within a given relative error range.

6.4.2 Low Temperature Data Comparison

The performance of valve -03 (which was used to obtain low temperature flow data) at room temperature, see Fig. 6.19, suggests the experimental results may be questionable. It is not understood why the valve was unable to modulate the flow from 0-60V at room temperature. Nevertheless, reasonable agreement between the low temperature experimental data and incompressible model predictions can be obtained by assuming an initial valve seat clearance of 1.03 μm, and an actuation constant of 0.0060 μm/V. The compressible model requires the assumption of ideal gas behavior, therefore the incompressible form of the model must be used. Figure 6.24 demonstrates the flow models prediction of the data from Fig. 6.14 using these estimated parameters.

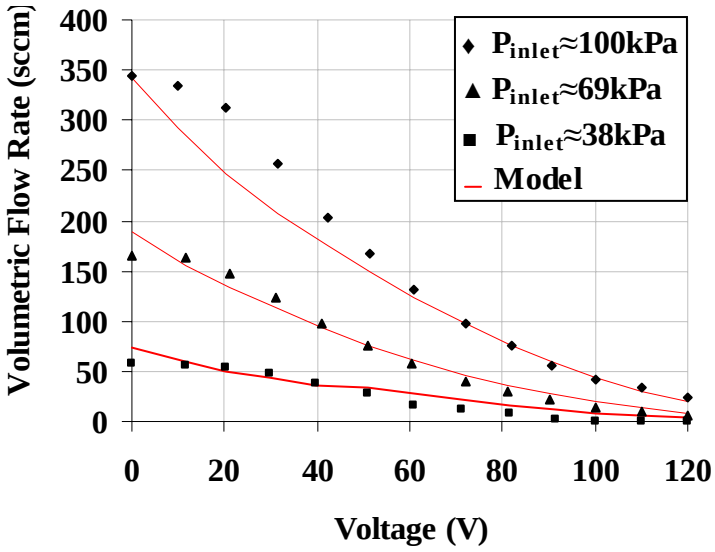

Figure 6.24: Model predictions of Fig. 6.17 data

Poor agreement between the model prediction and experimental data is experienced for the data taken with an inlet pressure of 38.0 kPa. One possible explanation is the fact that the accuracy of a calorimetric flow meter is reduced at low flow rates.

Figure 6.25 shows the predicted flow rate as a function of the measured flow rate for each experimental data points taken with valve -03 at inlet pressures of 100 kPa and 69.0 kPa.

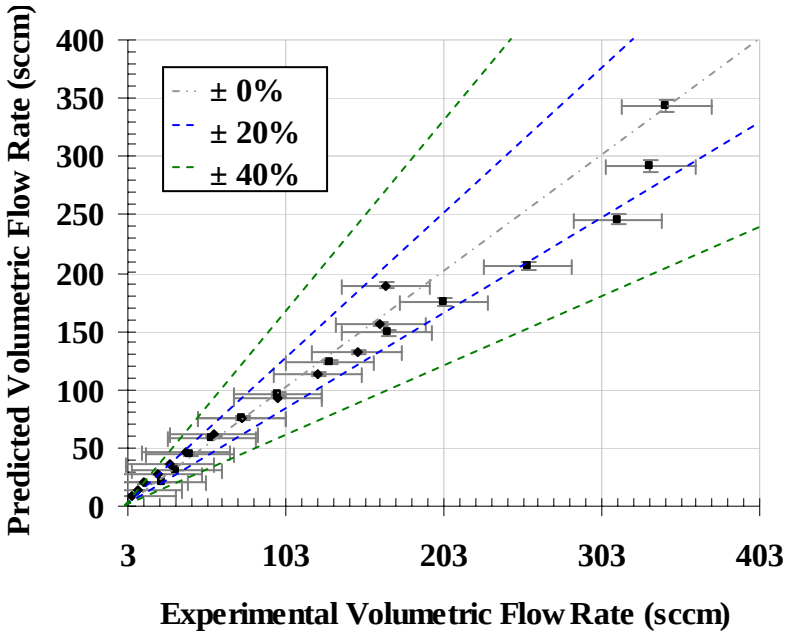

Figure 6.25: Predicted vs. experimental data for valve -03

The predicted error bars shown in Fig. 6.25 are calculated from the uncertainties in the variables listed in Table 6.3. The experimental error bars shown in 6.25 are calculated from the calorimetric flow meter's specification of ±4.0% full scale, which equates to approximately ±28 sccm.

6.5 Conclusion

Reasonable agreement was found between the model predictions and experimental room temperature flow data for valve -00. Some possible sources of modeling error that might explain the differences observed in Figs. 6.21 and 6.22 are listed below.

- The friction factor correlation for the high and low pressure grooves was conducted using a single value of the valve seat clearance. It is possible that

other values of the valve seat clearance would change the correlation curve behavior.

- The assumption that all of the high pressure groove inlets and low pressure groove exits are exposed to the same manifold pressure.
- The assumption that the Pyrex and land surface are exactly parallel to one another.
- The range of correlations used to represent the inertial losses in the manifolds, the grooves, and the land inlet were not large enough for some data and therefore extrapolation was required.

In addition to the possible sources of modeling error listed above, it was found that experimental data was not repeatable to within the accuracy of the measurement equipment. For example consider the difference between the data in Fig. 6.6 and the data from an equivalent experiment taken on valve -00 only a week before the data from Fig. 6.6, see Fig. 6.26.

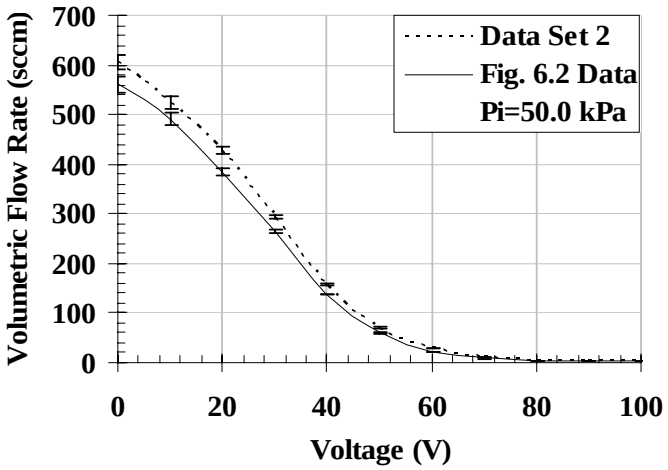

Figure 6.26: Comparing the experimental flow rate from valve -00 from two separate experiments conducted a week apart, P_i=50.0 kPa.

The repeatability error is most likely related to the hysteresis exhibited by the PZT, as observed by Taylor (2005). The repeatability is less of an issue than it might at first appear since the valve clearance and actuation constant are computed based on a set of data taken over a relatively short time. Further, the operation of the valve in practice is likely to be within a closed loop control system rather than through a mapping of voltage with flow. However, further study will be needed to better understand the reasons behind the lack of repeatability of the flow measurement results. Nevertheless, the room temperature data comparison proved the model to be acceptable for design and optimization purposes; as will be discussed in Chapter 7.

6.6 References

J.M. Park, et. al, *"A Piezoelectrically Actuated Ceramic-Si-Glass Micro valve for Distributed Cooling Systems,"* Hilton Head 2006

R.P. Taylor, G.F. Nellis, S.A. Klein, D.W. Hoch, J. Fellers, P. Roach, J.M. Park, Y. Gianchandani, "*Measurements of the Material Properties of a Laminated Piezoelectric Stack at Cryogenic Temperatures,*" International Cryogenic Materials Conference, 2005, in press.

Chapter 7

Conclusions

7.1 Micro Valve Flow Model for Design and Optimization

In this thesis, a flow model was developed and demonstrated to produce results that agree with experimental data measured for prototype micro valves. The validation of the flow model against experimental measurements suggests that the model is useful for, among other things, design and optimization of future micro valves.

One of the intentions of the micro valve design is to provide a large flow modulation while using PZT actuators with a relatively limited stroke. Experimental data showed that the existing prototype valves to successfully modulate flow; however, it is likely that significant improvement in the valve performance can be achieved through optimization of the land and groove geometry. The implementation of the flow model using the EES software makes it relatively easy to accomplish the optimization task. A chronological design process which can be used to optimize the flow modulation is suggested below.

- Estimate the initial seat clearance at design conditions.
- Select the thinnest possible land that can be manufactured.
- Select the deepest possible groove using a structural model of the land which accounts for the differential pressure between the high and low pressure grooves. Manufacturing limitations should be accounted for as well during this step.
- Maximize the mass flow rate per unit area of a single land and groove using the flow model and optimization functions integral to EES. Use the estimated initial seat clearance, selected land width, and groove depth at the design conditions with

the high and low pressure groove widths, and tip width as the unknown variables to be optimized.

- Use as many conical entrance holes in the manifolds as possible.

In the design process discussed above, the groove length is assumed to be governed by manufacturing decisions. It should be noted that, depending upon the design conditions and given parameters, the optimal high and low pressure groove widths can assume different values. This non-intuitive result is a product of the pressure distribution in the grooves having separate combinations of an inertial pressure gain or loss and a viscous loss. Even more advanced valve designs may utilize many rows of interleaved grooves in order to reduce the individual groove length while taking advantage of the complete land area.

7.2 Conclusion

The main focus of this thesis has been the development of a flow model for a specific type of perimeter augmented micro valve. The model was verified at room temperature by comparing its predictions to experimental measurements from prototype micro valves. Despite the fact that the model was developed for a specific type of perimeter augmented geometry, the methodology and techniques used for the modeling (specifically the use of compressible, slip flow governing equations and the integration of CFD models with lower order system level models) will be useful for future efforts in the field of micro valves. An additional important element of this thesis was the development of non-dimensional numbers in Chapter 2 which were found to adequately characterize the valve

and can be used to understand the valve's operating regimes as well as obtain a quick estimate of its performance. The non-dimensional numbers may be additionally useful for future efforts related to the development of optimal control strategies or control methods using feed-forward control algorithms. In addition to these efforts, this thesis has presented experimental data which has demonstrated that the actively controlled micro valve design is capable of functioning at cryogenic temperatures.

Appendix A

```
%   Two Dimensional Incompressible Model Code for a Single Land and Groove


%+++++++++++++++++++++++++++Input Variables++++++++++++++++++++++++++++++

clear all
h=4*10^-6;                      %Seat clearance
L=.0020;                        %Groove length
P_high=100000;                  %High pressure groove inlet pressure
P_low=0;                        %Low pressure groove exit Pressure
P_atm=(P_high+P_low)/2000;      %Pressure inside Macor cap
mue=2e-5;                       %Viscosity
rho=.5;                         %Density
n=50;                           %y-Axid node number
m=300;                          %x-Axis node number
w=50*10^-6;                     %Land width
w_tip=50*10^-6;                 %Tip width
w_g=25*10^-6;                   %Groove half width
h_g=50*10^-6;                   %Groove height

%+++++++++++++++++++++++Calculated Variables++++++++++++++++++++++++++++

per_g=w_g*4+2*(h_g+h);          %Groove perimeter
A_g=2*w_g*(h_g+h);              %Groove cross sectional area
dy=w/n;                         %y-Axis groove spacing
sigma=h/(h+h_g);                %Inertial correlation variable
K_e=(1-sigma)^2;                %Land exit inertial correlation coeff.
K_c=.42*(1-sigma^2);            %Land inlet inertial correlaton coeff.
dp=P_high-P_low;                %Total pressure difference
sigma_g=(.5*A_g)/(h+h_g)*(2*w_g+w); %Groove inertial correlation variable
K_cg=.42*(1-sigma_g^2);         %Inlet inertial correlation coeff.
K_eg=(1-sigma_g)^2;             %Exit inertial correlation coeff.


alpha=min(h+h_g,2*w_g)/             %Groove calculation variable
max(h+h_g,2*w_g);

K=24*(1-1.3553*alpha+1.9467*alpha^2   %Groove equation variable
-1.7012*alpha^3+.9564*alpha^4-.2537*alpha^5);

C_1=K*mue*(per_g^2)/(32*rho*A_g^3);4  %Constant used in calculations below



%+++++++++++++++++++++++++++++Setup Matrices++++++++++++++++++++++++++++


A=spalloc((m+1)*(n+2),(m+1)*(n+2),5);
B=spalloc((m+1)*(n+2),1,1);
dx=L/m;

%Interior of the land
```

```
for i=1:m-1
    for j=2:n-1
        A(i+1+j*(m+1),i+1+j*(m+1))=-2*(h^3)/(dx^2)-2*(h^3)/(dy^2);
        A(i+1+j*(m+1),i+1+1+j*(m+1))=(h^3)/dx^2;
        A(i+1+j*(m+1),i+1-1+j*(m+1))=(h^3)/dx^2;
        A(i+1+j*(m+1),i+1+(j+1)*(m+1))=(h^3)/dy^2;
        A(i+1+j*(m+1),i+1+(j-1)*(m+1))=(h^3)/dy^2;
        B(i+1+j*(m+1))=0;
    end
end

%Left hand side of the land

for i=0
    for j=2:n-1
        A(i+1+j*(m+1),i+1+j*(m+1))=-2*(1/dx^2+1/dy^2);
        A(i+1+j*(m+1),i+1+1+j*(m+1))=2/dx^2;
        A(i+1+j*(m+1),i+1+(j+1)*(m+1))=1/dy^2;
        A(i+1+j*(m+1),i+1+(j-1)*(m+1))=1/dy^2;
        B(i+1+j*(m+1))=0;
    end
end

%Left lower corner of the land

for i=0
    for j=1
        A(i+1+j*(m+1),i+1+j*(m+1))=-1;
        A(i+1+j*(m+1),i+1+1+j*(m+1))=1;
        B(i+1+j*(m+1))=0;
    end
end

%Left upper corner of the land

for i=0
    for j=n
        A(i+1+j*(m+1),i+1+j*(m+1))=-1;
        A(i+1+j*(m+1),i+1+1+j*(m+1))=1;
        B(i+1+j*(m+1))=0;
    end
end

%Right lower corner of the land

for i=m
    for j=1
        A(i+1+j*(m+1),i+1+j*(m+1))=-1;
        A(i+1+j*(m+1),i+1-1+j*(m+1))=1;
        B(i+1+j*(m+1))=0;
    end
```

```
end

%Right upper corner of the land

for i=m
    for j=n
        A(i+1+j*(m+1),i+1+j*(m+1))=-1;
        A(i+1+j*(m+1),i+1-1+j*(m+1))=1;
        B(i+1+j*(m+1))=0;
    end
end

%Right side of the land

for i=m
    for j=2:n-1
        A(i+1+j*(m+1),i+1+j*(m+1))=-2*(1/dx^2+1/dy^2);
        A(i+1+j*(m+1),i+1-1+j*(m+1))=2/dx^2;
        A(i+1+j*(m+1),i+1+(j+1)*(m+1))=1/dy^2;
        A(i+1+j*(m+1),i+1+(j-1)*(m+1))=1/dy^2;
        B(i+1+j*(m+1))=0;
    end
end

%+++++++++++++++++Guess Values for Linearization Constants++++++++++++++++++

E=10000000;
for i=1:2*(m-1)
    C_2(i)=4.1002e-010;
end
   C_2(2*m-1)=1.9039e+010;
   C_2(2*m)=C_2(2*m-1);
   C_2(2*m+1)=C_2(1);
   C_2(2*m+2)=2.6881e+011;
   C_2(2*m+3)=C_2(1);
   C_2(2*m+4)=2.6881e+011;
cnt=0;

%++++++++++++++++++++Setup Iterative Solution++++++++++++++++++++++++++++++

while E>=.0000001
    Beta=w_tip*K*mue*per_g^2/(16*rho*A_g^3);    %Constant
    E_b=E;

%High pressure groove inlet node

    for i=0
        for j=n+1
        A(i+1+j*(m+1),i+1+j*(m+1))=-1*.5/(C_1*dx)-1/(Beta+C_2(2*m-1));
        A(i+1+j*(m+1),i+1+1+j*(m+1))=1*.5/(C_1*dx);
        B(i+1+j*(m+1))=-P_high/(Beta+C_2(2*m-1));
        end
```

```
    end

%Low pressure groove exit node

    for i=m
        for j=0
        A(i+1+j*(m+1),i+1+j*(m+1))=-1*.5/(C_1*dx)-1/(Beta+C_2(2*m));
        A(i+1+j*(m+1),i+1-1+j*(m+1))=1*.5/(C_1*dx);
        B(i+1+j*(m+1))=-P_low/(Beta+C_2(2*m));
        end
    end

    Beta_2=12*mue*w_tip/(h^2*rho*w_g*h);   %Constant

%Left hand side low pressure node

    for i=0
        for j=0
        A(i+1+j*(m+1),i+1+j*(m+1))=-1*.5/(C_1*dx)-1/
        (Beta_2+C_2(2*m+2))-C_2(2*m+1);
        A(i+1+j*(m+1),i+1+1+j*(m+1))=1*.5/(C_1*dx);
        A(i+1+j*(m+1),i+1+(j+1)*(m+1))=C_2(2*m+1);
        B(i+1+j*(m+1))=-P_high/(Beta_2+C_2(2*m+2));
        end
    end

%Right hand side high pressure groove

    for i=m
        for j=n+1
        A(i+1+j*(m+1),i+1+j*(m+1))=-1*.5/(C_1*dx)-1/
        (Beta_2+C_2(2*m+4))-C_2(2*m+3);
        A(i+1+j*(m+1),i+1-1+j*(m+1))=1*.5/(C_1*dx);
        A(i+1+j*(m+1),i+1+(j-1)*(m+1))=C_2(2*m+3);
        B(i+1+j*(m+1))=-P_low/(Beta_2+C_2(2*m+4));
        end
    end

%High pressure groove nodes

    for j=n+1
        for i=1:m-1
            A(i+1+j*(m+1),i+1+j*(m+1))=-2*.5/(C_1*dx)-C_2(i+m-1);
            A(i+1+j*(m+1),i+1+1+j*(m+1))=1*.5/(C_1*dx);
            A(i+1+j*(m+1),i+1-1+j*(m+1))=1*.5/(C_1*dx);
            A(i+1+j*(m+1),i+1+(j-1)*(m+1))=C_2(i+m-1);
            B(i+1+j*(m+1))=0;
        end
    end

%Low pressure groove nodes
```

```
    for j=0
        for i=1:m-1
            A(i+1+j*(m+1),i+1+j*(m+1))=.5*(-2/(C_1*dx))-C_2(i);
            A(i+1+j*(m+1),i+1+1+j*(m+1))=1*.5/(C_1*dx);
            A(i+1+j*(m+1),i+1-1+j*(m+1))=1*.5/(C_1*dx);
            A(i+1+j*(m+1),i+1+(j+1)*(m+1))=C_2(i);
            B(i+1+j*(m+1))=0;
        end
    end

%High pressure land nodes adjacent to groove

    for j=n
        for i=1:m-1
            A(i+1+j*(m+1),i+1+j*(m+1))=-C_2(i+m-1)-2*dy*rho*h^3/
            (12*mue*dx)-rho*dx*h^3/(12*mue*dy);
            A(i+1+j*(m+1),i+1+1+j*(m+1))=dy*rho*h^3/(12*mue*dx);
            A(i+1+j*(m+1),i+1-1+j*(m+1))=dy*rho*h^3/(12*mue*dx);
            A(i+1+j*(m+1),i+1+(j+1)*(m+1))=C_2(i+m-1);
            A(i+1+j*(m+1),i+1+(j-1)*(m+1))=rho*dx*h^3/(12*mue*dy);
            B(i+1+j*(m+1))=0;
        end
    end

%Low pressure land nodes adjacent to groove

    for j=1
        for i=1:m-1
            A(i+1+j*(m+1),i+1+j*(m+1))=-C_2(i)-2*dy*rho*h^3/(12*mue*dx)-
            rho*dx*h^3/(12*mue*dy);
            A(i+1+j*(m+1),i+1+1+j*(m+1))=dy*rho*h^3/(12*mue*dx);
            A(i+1+j*(m+1),i+1-1+j*(m+1))=dy*rho*h^3/(12*mue*dx);
            A(i+1+j*(m+1),i+1+(j-1)*(m+1))=C_2(i);
            A(i+1+j*(m+1),i+1+(j+1)*(m+1))=rho*dx*h^3/(12*mue*dy);
            B(i+1+j*(m+1))=0;
        end
    end

%++++++++++++++++++++++++++++++Solve Setup Matrices++++++++++++++++++++++++

    P=A\B;

%++++++++++++++++++++++++++Update Linearization Constants++++++++++++++++++++

%+++Calculate estimated mass flow rates from linerized constants

    for i=1:m-1
        for j=0
            m_dot_est(i)=C_2(i)*(P(i+1+(j+1)*(m+1))-P(i+1+j*(m+1)));
        end
        for j=n
            m_dot_est(i+m-1)=C_2(i+m-1)*(P(i+1+(j+1)*(m+1))-
```

```
            P(i+1+(j)*(m+1)));
        end
    end
    for i=0
        for j=0
            m_dot_est(2*m+1)=C_2(2*m+1)*(P(i+1+(j+1)*(m+1))-
            P(i+1+j*(m+1)));
        end
    end
    for i=0
        for j=0
            m_dot_est(2*m+2)=(P_high-P(i+1+j*(m+1)))/(C_2(2*m+2)+Beta_2);
        end
    end
    for i=m
        for j=n+1
            m_dot_est(2*m+3)=C_2(2*m+3)*(P(i+1+j*(m+1))-
            P(i+1+(j-1)*(m+1)));
        end
    end
    for i=m
        for j=n+1
            m_dot_est(2*m+4)=(-P_low+P(i+1+j*(m+1)))/(C_2(2*m+4)+Beta_2);
        end
    end
    for i=0
        for j=n+1
            m_dot_est(2*m-1)=(P_high-P(i+1+(j)*(m+1)))/(Beta+C_2(2*m-1));
        end
    end
    for i=m
        for j=0
            m_dot_est(2*m)=(-P_low+P(i+1+(j)*(m+1)))/(Beta+C_2(2*m));
        end
    end

%+++Calculate actual mass flow rates

    for i=1:m-1
        for j=0
            m_dot(i)=sqrt((1/K_e)*2*rho*(dx*h)^2*(P(i+1+(j+1)*(m+1))
            -P(i+1+j*(m+1))));
        end
        for j=n
            m_dot(i+m-1)=sqrt((1/K_c)*2*rho*(dx*h)^2*(P(i+1+(j+1)*(m+1))
            -P(i+1+(j)*(m+1))));
        end
    end
    delta=.5*K_cg/(((.5*A_g)^2)*rho);
    for i=0
        for j=n+1
            m_dot(2*m-1)=(-Beta+sqrt(Beta^2+4*delta*(P_high-P(i+1+(j)*
```

```
            (m+1)))))/(2*delta);
        end
    end
    for i=m
        for j=0
            m_dot(2*m)=(-Beta+sqrt(Beta^2+4*delta*(-P_low+P(i+1+(j)*
            (m+1)))))/(2*delta);
        end
    end

    delta_2=.5*rho*(K_c+K_e)/(((w_g*h)^2)*rho^2);

    for i=0
        for j=0
            m_dot(2*m+1)=sqrt((1/K_e)*2*rho*(dx*h)^2*(P(i+1+(j+1)*(m+1))-
            P(i+1+(j)*(m+1))));
        end
    end
    for i=0
        for j=0
            m_dot(2*m+2)=(-Beta_2+sqrt(Beta_2^2+4*delta_2*(P_high-
            P(i+1+(j)*(m+1)))))/(2*delta_2);
        end
    end
    for i=m
        for j=n+1
            m_dot(2*m+3)=sqrt((1/K_e)*2*rho*(dx*h)^2*(P(i+1+(j)*(m+1))-
            P(i+1+(j-1)*(m+1))));
        end
    end
    for i=m
        for j=n+1
            m_dot(2*m+4)=(-Beta_2+sqrt(Beta_2^2+4*delta_2*(P(i+1+(j)*
            (m+1))-P_low)))/(2*delta_2);
        end
    end
    for i=1:2*(m)+4
        Error(i)=abs(m_dot(i)-m_dot_est(i))/m_dot(i);
    end
    E=max(Error);

%+++Update linearization coefficients

    for i=1:m-1
        for j=0
            C_2(i)=(1*m_dot(i)+0*m_dot_est(i))/(P(i+1+(j+1)*(m+1))-
            P(i+1+j*(m+1)));
        end
        for j=n
            C_2(i+m-1)=(1*m_dot(i+m-1)+0*m_dot_est(i+m-1))/
            (P(i+1+(j+1)*(m+1))-P(i+1+j*(m+1)));
        end
```

```
    end
    for i=0
        for j=n+1
            C_2(2*m-1)=(P_high-P(i+1+j*(m+1)))/(m_dot(2*m-1)+
            0*m_dot(2*m-1))-Beta;
        end
    end
    for i=m
        for j=0
            C_2(2*m)=(P(i+1+j*(m+1))-P_low)/(m_dot(2*m)+
            0*m_dot(2*m))-Beta;
        end
    end
    for i=0
        for j=0
            C_2(2*m+1)=(1*m_dot(2*m+1)+0*m_dot_est(2*m+1))/
            (P(i+1+(j+1)*(m+1))-P(i+1+j*(m+1)));
        end
    end
    for i=0
        for j=0
            C_2(2*m+2)=(P_high-P(i+1+j*(m+1)))/(1*m_dot(2*m+2)+
            0*m_dot(2*m+2))-Beta_2;
        end
    end
    for i=m
        for j=n+1
            C_2(2*m+3)=(1*m_dot(2*m+3)+0*m_dot_est(2*m+3))/
            (P(i+1+(j)*(m+1))-P(i+1+(j-1)*(m+1)));
        end
    end
    for i=m
        for j=n+1
            C_2(2*m+4)=(P(i+1+j*(m+1))-P_low)/(1*m_dot(2*m+4)+
            0*m_dot(2*m+4))-Beta_2;
        end
    end
end

%++++++++++++++++++++++++++End of Iterative Solution++++++++++++++++++++++++


%++++++++++++Calculate Velocity and Pressure Distribution+++++++++++++++++++

for i=1:m
    for j=1:n-1
        vm(j+1,i+1)=(h^2/(12*mue))*(P(i+1+(j+1)*(m+1))-
        P(i+1+j*(m+1)))/dy;
    end
end

for i=1:m
```

```
    for j=1:n-1
        um(j+1,i+1)=(h^2/(12*mue))*(P(i+1-1+(j)*(m+1))-
        P(i+1+j*(m+1)))/dx;
    end
end

for i=0:m
    for j=0:n+1
        Press(j+1,i+1)=P(i+1+(j)*(m+1));
    end
end
```

Appendix B

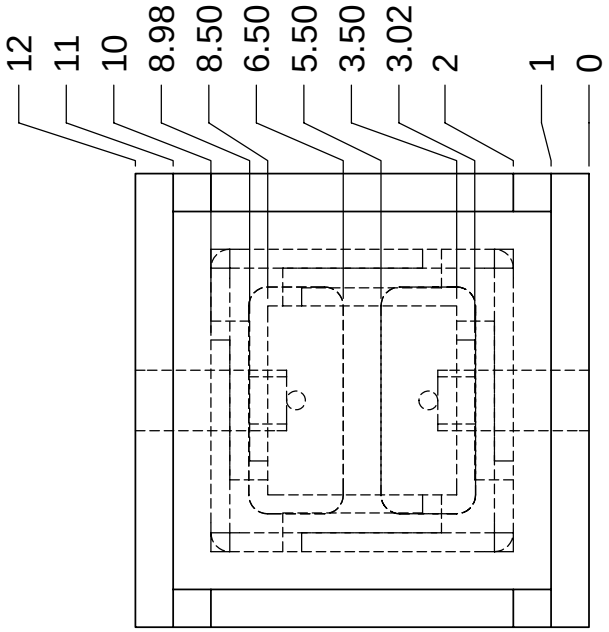

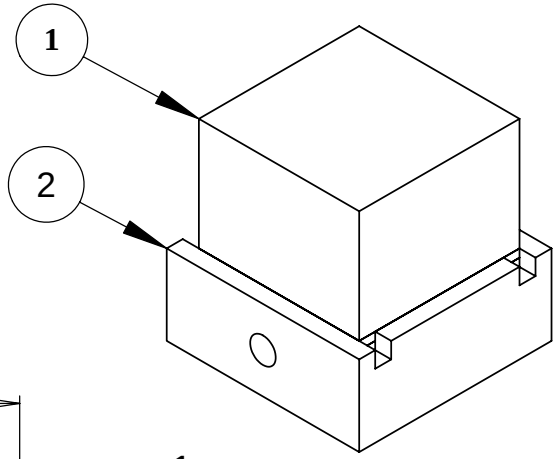

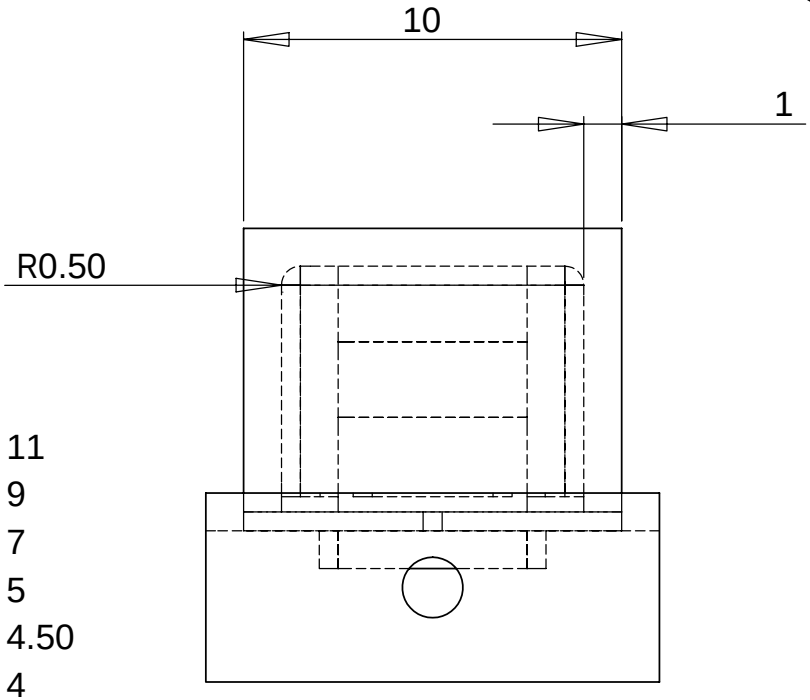

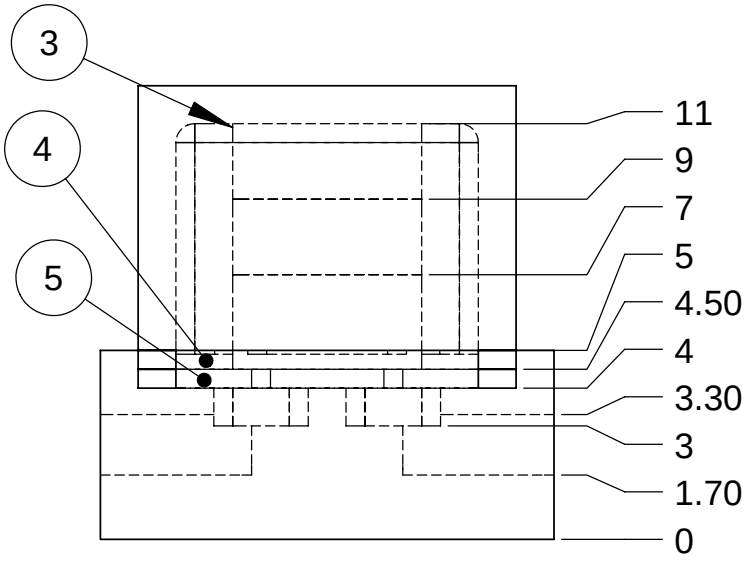

1. Macor cap
2. Macor manifold
3. PZT stack
4. Silicon die
5. Pyrex substrate

TITLE:

Appendix B
Valve Assembly Structural Model

SIZE **A**

Tyler Brosten, MS Thesis

All Dims. (mm)

5 4 3 2 1

Appendix C

EES Code of Micro Valve Flow Model

Universal Variables

$P_i = [b + 14.7] \cdot \left| 6894.76 \cdot \frac{Pa}{psi} \right|$ *Inlet Pressure to Valve*

$P_o = 101000$ [Pa] *Outlet Pressure from Valve*

$T = 83$ [K] *Temperature*

Gas$ = 'Helium'

$\delta = \delta_0 - \delta_V + \delta_P$ *Valve Seat Clearance*

$w_{tip} = 0.0001$ [m] *Width of the Tip*

$w_l = 0.0001$ [m] *Width of the Land*

$L_g = 0.0028$ [m] *Groove Length*

$w_g = 0.00005$ [m] *Full Width of the Groove*

$d_g = 0.00011$ [m] *Depth of the Groove*

M = **MolarMass** [Gas$] *Molecular Weight of the gas*

$\sigma = 0.825$ *Tangential Momentum Coeff.*

Voltage = 0 *Voltage*

Displacement Calculations

$\delta_V = \text{Voltage} \cdot \frac{8.9 \times 10^{-7}}{100 \quad [m]}$ *Displacement reduction due to voltage*

$\delta_0 = 0.00000145$ [m] *Initial seat displacement*

$\delta_P = [P_{avg} - 101] \cdot 1.6 \times 10^{-9}$ [m] *Displacement addition from internal pressure*

$P_{avg} = \frac{P_o + P_i}{2000}$

Volumetric Flow Rate Calculation

$\dot{V} = \frac{\dot{m}_{lp,header}}{\rho[\text{Gas\$}, T = 293.5, P = P_o]} \cdot \left| 6 \times 10^7 \cdot \frac{mL/min}{m^3/s} \right|$

Header Variables

$w_h = 0.0005$ [m] *Width of the Manifold*

$N_{hg} = 26$ *Number of Half Grooves inside the valve*

$D_1 = 0.0005$ [m] *Larger Diameter of Header Cone*

$D_2 = 0.000333$ [m] *Smaller Diameter of Header Cone*

$Area_1 = \pi \cdot 0.25 \cdot D_1^2$

$Area_2 = \pi \cdot 0.25 \cdot D_2^2$

$c_1 = \frac{0.0003}{0.0005}$

$c_2 = \frac{0.00035}{0.0005}$

$c_3 = \frac{0.0004}{0.0005}$

$r_i = \frac{D_2}{w_h}$

$rz = \left[\frac{0.0001}{\delta + d_g}\right]^2$ *Scaling Factor for change in groove depth*

Header Mass Balances

$N_{hg} \cdot [\dot{m}_{h,1} + \dot{m}_{gl,32}] = \dot{m}_{hp,header}$

$N_{hg} \cdot [\dot{m}_{l,30} + \dot{m}_{gl,31}] = \dot{m}_{lp,header}$

High Pressure Header Equations

$\rho_{hp} = \rho\left[Gas\$, T = T, P = \frac{P_i + P_{high}}{2}\right]$

$mue_{hp} = \mathbf{Visc}\left[Gas\$, T = T, P = \frac{P_i + P_{high}}{2}\right]$

$V_{d1} = \frac{\dot{m}_{hp,header}}{\rho_{hp} \cdot Area_1}$

$V_{d2} = \frac{\dot{m}_{hp,header}}{\rho_{hp} \cdot Area_2}$

$Re_{d1} = \rho_{hp} \cdot V_{d1} \cdot \frac{D_1}{mue_{hp}}$

$K_{hp1} = \mathbf{Interpolate}['300i', 'Re', 'K_h', 'Re' = Re_{d1}]$

$K_{hp2} = \mathbf{Interpolate}['350i', 'Re', 'K_h', 'Re' = Re_{d1}]$

$K_{hp3} = \mathbf{Interpolate}['400i', 'Re', 'K_h', 'Re' = Re_{d1}]$

Second Order Polynomial Fit to Lookup Table

$K_{hp3} + K_{hp2} + K_{hp1} = 3 \cdot a_{i1} + [c_1 + c_2 + c_3] \cdot a_{i2} + [c_1^2 + c_2^2 + c_3^2] \cdot a_{i3}$

$$c_1 \cdot K_{hp1} + c_2 \cdot K_{hp2} + c_3 \cdot K_{hp3} = [c_1 + c_2 + c_3] \cdot a_{i1} + [c_1^2 + c_2^2 + c_3^2] \cdot a_{i2} + [c_1^3 + c_2^3 + c_3^3] \cdot a_{i3}$$

$$c_1^2 \cdot K_{hp1} + c_2^2 \cdot K_{hp2} + c_3^2 \cdot K_{hp3} = [c_1^2 + c_2^2 + c_3^2] \cdot a_{i1} + [c_1^3 + c_2^3 + c_3^3] \cdot a_{i2} + [c_1^4 + c_2^4 + c_3^4] \cdot a_{i3}$$

$$K_{hp} = [a_{i1} + a_{i2} \cdot r_i + a_{i3} \cdot r_i^2] \cdot rz$$

$$P_i - P_{high} = K_{hp} \cdot 0.5 \cdot \rho_{hp} \cdot V_{d2}^2$$

Low Pressure Header Equations

$$\rho_{lp} = \rho\left[\text{Gas\$}, T = T, P = \frac{P_o + P_{low}}{2}\right]$$

$$mue_{lp} = \textbf{Visc}\left[\text{Gas\$}, T = T, P = \frac{P_o + P_{low}}{2}\right]$$

$$V_{d1l} = \frac{\dot{m}_{lp,header}}{\rho_{lp} \cdot Area_1}$$

$$V_{d2l} = \frac{\dot{m}_{lp,header}}{\rho_{lp} \cdot Area_2}$$

$$Re_{d1l} = \rho_{lp} \cdot V_{d1l} \cdot \frac{D_1}{mue_{lp}}$$

$$K_{hp1l} = \textbf{Interpolate}['300o', 'Re', 'K_h', 'Re' = Re_{d1l}]$$

$$K_{hp2l} = \textbf{Interpolate}['350o', 'Re', 'K_h', 'Re' = Re_{d1l}]$$

$$K_{hp3l} = \textbf{Interpolate}['400o', 'Re', 'K_h', 'Re' = Re_{d1l}]$$

Second Order Polynomial Fit to Lookup Table

$$K_{hp3l} + K_{hp2l} + K_{hp1l} = 3 \cdot a_{i1l} + [c_1 + c_2 + c_3] \cdot a_{i2l} + [c_1^2 + c_2^2 + c_3^2] \cdot a_{i3l}$$

$$c_1 \cdot K_{hp1l} + c_2 \cdot K_{hp2l} + c_3 \cdot K_{hp3l} = [c_1 + c_2 + c_3] \cdot a_{i1l} + [c_1^2 + c_2^2 + c_3^2] \cdot a_{i2l} + [c_1^3 + c_2^3 + c_3^3] \cdot a_{i3l}$$

$$c_1^2 \cdot K_{hp1l} + c_2^2 \cdot K_{hp2l} + c_3^2 \cdot K_{hp3l} = [c_1^2 + c_2^2 + c_3^2] \cdot a_{i1l} + [c_1^3 + c_2^3 + c_3^3] \cdot a_{i2l} + [c_1^4 + c_2^4 + c_3^4] \cdot a_{i3l}$$

$$K_{lp} = [a_{i1l} + a_{i2l} \cdot r_i + a_{i3l} \cdot r_i^2] \cdot rz$$

$$P_{low} - P_o = K_{lp} \cdot 0.5 \cdot \rho_{lp} \cdot V_{d2l}^2$$

Land and Groove Variables

$$N = 30$$

$$dx = \frac{L_g}{N}$$

$$dh = 4 \cdot \frac{Ac_g}{per_g}$$

$$Ac_g = \left[d_g + \delta \right] \cdot w_g$$

$$per_g = 2 \cdot \left[d_g + \delta + w_g \right]$$

$$\rho_h = \rho\left[Gas\$, T = T , P = \frac{P_{high} + P_{h,30}}{2} \right]$$

$$mue_h = \mathbf{Visc}\left[Gas\$, T = T , P = \frac{P_{high} + P_{h,30}}{2} \right]$$

$$\rho_l = \rho\left[Gas\$, T = T , P = \frac{P_{low} + P_{l,1}}{2} \right]$$

$$mue_l = \mathbf{Visc}\left[Gas\$, T = T , P = \frac{P_{low} + P_{l,1}}{2} \right]$$

Groove Mass Flow Rate Calculations

$$\frac{P_{high} - P_{h,1}}{w_{tip} + \frac{dx}{2}} = \rho_h \cdot f_{h,1} \cdot 0.5 \cdot \frac{1}{dh} \cdot v_{h,1}^{\,2}$$

$$\frac{P_{l,30} - P_{low}}{w_{tip} + \frac{dx}{2}} = \rho_l \cdot f_{l,30} \cdot 0.5 \cdot \frac{1}{dh} \cdot v_{l,1}^{\,2}$$

$$\frac{-P_{h,i} + P_{h,i-1}}{dx} = \rho_h \cdot f_{h,i} \cdot 0.5 \cdot \frac{1}{dh} \cdot v_{h,i}^{\,2} + \rho_h \cdot dv_{h\backslash dx,i} \cdot v_{h,i} \quad \text{for } i = 2 \text{ to } N$$

$$dv_{h\backslash dx,i} = -1 \cdot \left[\frac{1/6 \cdot v_{h,i+1} - v_{h,i} + 0.5 \cdot v_{h,i-1} + 1/3 \cdot v_{h,i-2}}{dx} \right] \quad \text{for } i = 3 \text{ to } N$$

$$dv_{h\backslash dx,2} = dv_{h\backslash dx,3}$$

$$v_{h,31} = 0$$

$$\frac{P_{l,i} - P_{l,i+1}}{dx} = \rho_l \cdot f_{l,i} \cdot 0.5 \cdot \frac{1}{dh} \cdot v_{l,i}^{\,2} + v_{l,i} \cdot dv_{l\backslash dx,i} \cdot \rho_l \quad \text{for } i = 1 \text{ to } N-1$$

$$dv_{l\backslash dx,i} = -1 \cdot \left[\frac{1/6 \cdot v_{l,i+1} - v_{l,i} + 0.5 \cdot v_{l,i-1} + 1/3 \cdot v_{l,i-2}}{dx} \right] \quad \text{for } i = 2 \text{ to } N-1$$

$$v_{l,0} = 0$$

$$dv_{l\backslash dx,1} = dv_{l\backslash dx,2}$$

$$v_{h,i} = 2 \cdot \frac{\dot{m}_{h,i}}{\rho_h \cdot Ac_g} \quad \text{for } i = 1 \text{ to } N$$

$$v_{l,i} = 2 \cdot \frac{\dot{m}_{l,i}}{\rho_l \cdot Ac_g} \quad \text{for } i = 1 \text{ to } N$$

$$Re_{dh,i} = \rho_h \cdot v_{h,i} \cdot \frac{dh}{mue_h} \quad \text{for } i = 1 \text{ to } N$$

$$Re_{dl,i} = \rho_l \cdot v_{l,i} \cdot \frac{dh}{mue_l} \quad \text{for } i = 1 \text{ to } N$$

$$f_{h,i} = \textbf{Interpolate}\left[\text{'High}_p\text{'}, \text{'Re'}, \text{'f'}, \text{'Re'} = Re_{dh,i}\right] \quad \text{for } i = 1 \text{ to } N$$

$$f_{l,i} = \textbf{Interpolate}\left[\text{'Low}_p\text{'}, \text{'Re'}, \text{'f'}, \text{'Re'} = Re_{dl,i}\right] \quad \text{for } i = 1 \text{ to } N$$

Groove to Land Mass Flow Rate Calculations

$$\rho_{h2,i} = \rho\left[\text{Gas\$}, T = T, P = \frac{P_{h,i} + P_{h2,i}}{2}\right] \quad \text{for } i = 1 \text{ to } N$$

$$mue_{h2,i} = \textbf{Visc}\left[\text{Gas\$}, T = T, P = \frac{P_{h,i} + P_{h2,i}}{2}\right] \quad \text{for } i = 1 \text{ to } N$$

$$\rho_{l,i} = \rho\left[\text{Gas\$}, T = T, P = P_{l,i}\right] \quad \text{for } i = 1 \text{ to } N$$

$$mue_{l,i} = \textbf{Visc}\left[\text{Gas\$}, T = T, P = P_{l,i}\right] \quad \text{for } i = 1 \text{ to } N$$

$$u_{m,i} = \frac{\dot{m}_{gl,i}}{\rho_{h2,i} \cdot dx \cdot \delta} \quad \text{for } i = 1 \text{ to } N$$

$$P_{h,i} - P_{h2,i} = K_{c,i} \cdot 0.5 \cdot \rho_{h2,i} \cdot u_{m,i}^{\,2} \quad \text{for } i = 1 \text{ to } N$$

$$\dot{m}_{gl,i} = \delta^{\,3} \cdot dx \cdot \rho_{l,i} \cdot P_{l,i} \cdot \left[\frac{\frac{P_{h2,i}}{P_{l,i}} - 1 + 12 \cdot \sigma \cdot Kn_i \cdot \left(\frac{P_{h2,i}}{P_{l,i}} - 1\right)}{24 \cdot mue_{l,i} \cdot w_l}\right] \quad \text{for } i = 1 \text{ to } N$$

$$k2_i = \frac{\textbf{Cp}\left[\text{Gas\$}, T = T, P = P_{l,i}\right]}{\textbf{Cv}\left[\text{Gas\$}, T = T, P = P_{l,i}\right]} \quad \text{for } i = 1 \text{ to } N$$

$$c2_i = \textbf{SoundSpeed}\left[\text{Gas\$}, T = T, P = P_{l,i}\right] \quad \text{for } i = 1 \text{ to } N$$

$$M2_i = \frac{\dot{m}_{gl,i}}{c2_i \cdot \rho_{l,i} \cdot \delta \cdot dx} \quad \text{for } i = 1 \text{ to } N$$

$$Re2_i = \frac{\dot{m}_{gl,i}}{dx \cdot mue_{l,i}} \quad \text{for } i = 1 \text{ to } N$$

$$Kn_i = \sqrt{\pi \cdot k2_i \cdot 0.5} \cdot \frac{M2_i}{Re2_i} \quad \text{for } i = 1 \text{ to } N$$

$$x_i = i \quad \text{for } i = 1 \text{ to } N$$

High Pressure Tip Calculations

$$\rho_{h2,31} = \rho\left[\text{Gas\$}, T = T, P = \frac{P_{h,30} + P_{h2,31}}{2}\right]$$

$$mue_{h2,31} = \textbf{Visc}\left[\text{Gas\$}, T = T, P = \frac{P_{h,30} + P_{h2,31}}{2}\right]$$

$$\rho_{l,31} = \rho\left[\text{Gas\$}, T = T, P = P_{low}\right]$$

$$mue_{l,31} = \textbf{Visc}\left[\text{Gas\$}, T = T, P = P_{low}\right]$$

$$u_{m,31} = \frac{\dot{m}_{gl,31}}{\rho_{h2,31} \cdot 0.5 \cdot w_g \cdot \delta}$$

$$P_{h,30} - P_{h2,31} = K_{c,31} \cdot 0.5 \cdot \rho_{h2,31} \cdot u_{m,31}^{\ 2}$$

$$\dot{m}_{gl,31} = \delta^{\ 3} \cdot 0.5 \cdot w_g \cdot \rho_{l,31} \cdot P_{low} \cdot \left[\frac{\frac{P_{h2,31}}{P_{low}} - 1 + 12 \cdot \sigma \cdot Kn_{31} \cdot \left(\frac{P_{h2,31}}{P_{low}} - 1 \right)}{24 \cdot mue_{l,31} \cdot w_{tip}} \right]$$

$$k2_{31} = \frac{\mathbf{Cp}\left[Gas\$, T = T , P = P_{low} \right]}{\mathbf{Cv}\left[Gas\$, T = T , P = P_{low} \right]}$$

$$c2_{31} = \mathbf{SoundSpeed}\left[Gas\$, T = T , P = P_{low} \right]$$

$$M2_{31} = \frac{\dot{m}_{gl,31}}{c2_{31} \cdot \rho_{l,31} \cdot \delta \cdot 0.5 \cdot w_g}$$

$$Re2_{31} = \frac{\dot{m}_{gl,31}}{0.5 \cdot w_g \cdot mue_{l,31}}$$

$$Kn_{31} = \sqrt{\pi \cdot k2_{31} \cdot 0.5} \cdot \frac{M2_{31}}{Re2_{31}}$$

Low Pressure Tip Calculations

$$\rho_{h2,32} = \rho\left[Gas\$, T = T , P = \frac{P_{high} + P_{h2,32}}{2} \right]$$

$$mue_{h2,32} = \mathbf{Visc}\left[Gas\$, T = T , P = \frac{P_{high} + P_{h2,32}}{2} \right]$$

$$\rho_{l,32} = \rho\left[Gas\$, T = T , P = P_{l,1} \right]$$

$$mue_{l,32} = \mathbf{Visc}\left[Gas\$, T = T , P = P_{l,1} \right]$$

$$u_{m,32} = \frac{\dot{m}_{gl,31}}{\rho_{h2,31} \cdot 0.5 \cdot w_g \cdot \delta}$$

$$P_{high} - P_{h2,32} = K_{c,32} \cdot 0.5 \cdot \rho_{h2,32} \cdot u_{m,32}^{\ 2}$$

$$\dot{m}_{gl,32} = \delta^{\ 3} \cdot 0.5 \cdot w_g \cdot \rho_{l,32} \cdot P_{l,1} \cdot \left[\frac{\frac{P_{h2,32}}{P_{l,1}} - 1 + 12 \cdot \sigma \cdot Kn_{32} \cdot \left(\frac{P_{h2,32}}{P_{l,1}} - 1 \right)}{24 \cdot mue_{l,32} \cdot w_{tip}} \right]$$

$$k2_{32} = \frac{\mathbf{Cp}\left[Gas\$, T = T , P = P_{l,1} \right]}{\mathbf{Cv}\left[Gas\$, T = T , P = P_{l,1} \right]}$$

$$c2_{32} = \mathbf{SoundSpeed}\left[Gas\$, T = T , P = P_{l,1} \right]$$

$$M2_{32} = \frac{\dot{m}_{gl,32}}{c2_{32} \cdot \rho_{l,32} \cdot \delta \cdot 0.5 \cdot w_g}$$

$$Re2_{32} = \frac{\dot{m}_{gl,32}}{0.5 \cdot w_g \cdot mue_{l,32}}$$

$$Kn_{32} = \sqrt{\pi \cdot k2_{32} \cdot 0.5} \cdot \frac{M2_{32}}{Re2_{32}}$$

Total Mass Balances

$$\dot{m}_{h,i} = \dot{m}_{h,i+1} + \dot{m}_{gl,i} \quad \text{for } i = 1 \text{ to } N-1$$

$$\dot{m}_{h,30} = \dot{m}_{gl,30}$$

$$\dot{m}_{l,i} = \dot{m}_{l,i-1} + \dot{m}_{gl,i} \quad \text{for } i = 2 \text{ to } N$$

$$\dot{m}_{l,1} = \dot{m}_{gl,1}$$

Inertial Coeffiecient Lookup

$$h = \delta$$

$$a_1 = \frac{1}{111}$$

$$a_2 = \frac{2}{112}$$

$$a_3 = \frac{3}{113}$$

$$a_5 = \frac{5}{115}$$

$$a_6 = \frac{6}{116}$$

$$r_1 = \frac{h}{d_g + h}$$

$$Re_{h,i} = \frac{\dot{m}_{gl,i}}{dx \cdot mue_{h2,i}} \quad \text{for } i = 1 \text{ to } N$$

$$K_{g1,i} = \textbf{Interpolate}\left['1', 'Re_h', 'K_c', 'Re_h' = Re_{h,i}\right] \quad \text{for } i = 1 \text{ to } N$$

$$K_{g2,i} = \textbf{Interpolate}\left['2', 'Re_h', 'K_c', 'Re_h' = Re_{h,i}\right] \quad \text{for } i = 1 \text{ to } N$$

$$K_{g3,i} = \textbf{Interpolate}\left['3', 'Re_h', 'K_c', 'Re_h' = Re_{h,i}\right] \quad \text{for } i = 1 \text{ to } N$$

$$K_{g5,i} = \textbf{Interpolate}\left['5', 'Re_h', 'K_c', 'Re_h' = Re_{h,i}\right] \quad \text{for } i = 1 \text{ to } N$$

$$K_{g6,i} = \textbf{Interpolate}\left['6', 'Re_h', 'K_c', 'Re_h' = Re_{h,i}\right] \quad \text{for } i = 1 \text{ to } N$$

Second Order Polynomial Fit to Lookup Table

$$K_{g6,i} + K_{g5,i} + K_{g3,i} + K_{g2,i} = 4 \cdot b_{0,i} + \left[a_2 + a_3 + a_5 + a_6\right] \cdot b_{1,i} + \left[a_2^2 + a_3^2 + a_5^2 + a_6^2\right] \cdot b_{2,i}$$
for $i = 1$ to N

$$a_2 \cdot K_{g2,i} + a_3 \cdot K_{g3,i} + a_5 \cdot K_{g5,i} + a_6 \cdot K_{g6,i} = \left[a_2 + a_3 + a_5 + a_6\right] \cdot b_{0,i} + \left[a_2^2 + a_3^2 + a_5^2 + a_6^2\right] \cdot b_{1,i} + \left[a_2^3 + a_3^3 + a_5^3 + a_6^3\right] \cdot b_{2,i} \quad \text{for } i = 1 \text{ to } N$$

$$a_2^{\,2} \cdot K_{g2,i} + a_3^{\,2} \cdot K_{g3,i} + a_5^{\,2} \cdot K_{g5,i} + a_6^{\,2} \cdot K_{g6,i} = \left[a_2^{\,2} + a_3^{\,2} + a_5^{\,2} + a_6^{\,2}\right] \cdot b_{0,i} + \left[a_2^{\,3} + a_3^{\,3} + a_5^{\,3} + a_6^{\,3}\right] \cdot b_{1,i} + \left[a_2^{\,4} + a_3^{\,4} + a_5^{\,4} + a_6^{\,4}\right] \cdot b_{2,i} \quad \text{for } i = 1 \text{ to } N$$

$$K_{c,i} = \left[b_{0,i} + b_{1,i} \cdot r_1 + b_{2,i} \cdot r_1^{\,2}\right] \cdot \textbf{If}\left[r_1, a_2, 0, 0, 1\right] + \left[K_{g2,i} + \left(K_{g1,i} - K_{g2,i}\right) \cdot \left(\frac{a_2 - r_1}{a_2 - a_1}\right)\right] \cdot \textbf{If}\left[r_1, a_2, 1, 1, 0\right] \quad \text{for } i = 1 \text{ to } N$$

Inertial Coeffiecient Lookup for the Tip

$$Re_{h,i} = \frac{\dot{m}_{gl,i}}{0.5 \cdot w_g \cdot mue_{h2,i}} \quad \text{for } i = N+1 \text{ to } N+2$$

$$K_{g1,i} = \textbf{Interpolate}\left['1', 'Re_h', 'K_c', 'Re_h' = Re_{h,i}\right] \quad \text{for } i = N+1 \text{ to } N+2$$

$$K_{g2,i} = \textbf{Interpolate}\left['2', 'Re_h', 'K_c', 'Re_h' = Re_{h,i}\right] \quad \text{for } i = N+1 \text{ to } N+2$$

$$K_{g3,i} = \textbf{Interpolate}\left['3', 'Re_h', 'K_c', 'Re_h' = Re_{h,i}\right] \quad \text{for } i = N+1 \text{ to } N+2$$

$$K_{g5,i} = \textbf{Interpolate}\left['5', 'Re_h', 'K_c', 'Re_h' = Re_{h,i}\right] \quad \text{for } i = N+1 \text{ to } N+2$$

$$K_{g6,i} = \textbf{Interpolate}\left['6', 'Re_h', 'K_c', 'Re_h' = Re_{h,i}\right] \quad \text{for } i = N+1 \text{ to } N+2$$

Second Order Polynomial Fit to Lookup Table

$$K_{g6,i} + K_{g5,i} + K_{g3,i} + K_{g2,i} = 4 \cdot b_{0,i} + \left[a_2 + a_3 + a_5 + a_6\right] \cdot b_{1,i} + \left[a_2^{\,2} + a_3^{\,2} + a_5^{\,2} + a_6^{\,2}\right] \cdot b_{2,i} \quad \text{for } i = N+1 \text{ to } N+2$$

$$a_2 \cdot K_{g2,i} + a_3 \cdot K_{g3,i} + a_5 \cdot K_{g5,i} + a_6 \cdot K_{g6,i} = \left[a_2 + a_3 + a_5 + a_6\right] \cdot b_{0,i} + \left[a_2^{\,2} + a_3^{\,2} + a_5^{\,2} + a_6^{\,2}\right] \cdot b_{1,i} + \left[a_2^{\,3} + a_3^{\,3} + a_5^{\,3} + a_6^{\,3}\right] \cdot b_{2,i} \quad \text{for } i = N+1 \text{ to } N+2$$

$$a_2^{\,2} \cdot K_{g2,i} + a_3^{\,2} \cdot K_{g3,i} + a_5^{\,2} \cdot K_{g5,i} + a_6^{\,2} \cdot K_{g6,i} = \left[a_2^{\,2} + a_3^{\,2} + a_5^{\,2} + a_6^{\,2}\right] \cdot b_{0,i} + \left[a_2^{\,3} + a_3^{\,3} + a_5^{\,3} + a_6^{\,3}\right] \cdot b_{1,i} + \left[a_2^{\,4} + a_3^{\,4} + a_5^{\,4} + a_6^{\,4}\right] \cdot b_{2,i} \quad \text{for } i = N+1 \text{ to } N+2$$

$$K_{c,i} = \left[b_{0,i} + b_{1,i} \cdot r_1 + b_{2,i} \cdot r_1^{\,2}\right] \cdot \textbf{If}\left[r_1, a_2, 0, 0, 1\right] + \left[K_{g2,i} + \left(K_{g1,i} - K_{g2,i}\right) \cdot \left(\frac{a_2 - r_1}{a_2 - a_1}\right)\right] \cdot \textbf{If}\left[r_1, a_2, 1, 1, 0\right] \quad \text{for } i = N+1 \text{ to } N+2$$

Lookup Table: 1

	Re_h	K_c
Row 1	2.5	26.28
Row 2	3.57	13.22
Row 3	4.298	10.65
Row 4	6.275	8.254
Row 5	9.64	6.97
Row 6	12.62	6.23
Row 7	19	5.18
Row 8	25.75	4.45
Row 9	31.27	4.02
Row 10	38.62	3.673

Lookup Table: 1

	Re_h	K_c
Row 11	130.4	2.378
Row 12		
Row 13		
Row 14		
Row 15		
Row 16		
Row 17		
Row 18		
Row 19		
Row 20		

Lookup Table: 2

	Re_h	K_c
Row 1	1.25	30.07
Row 2	1.92	14.73
Row 3	2.2	13
Row 4	2.56	11.49
Row 5	3.36	9.56
Row 6	5.27	7.52
Row 7	9.21	5.56
Row 8	13	4.62
Row 9	19.1	3.77
Row 10	25.5	3.28
Row 11	32	2.99
Row 12	38.4	2.8
Row 13	51.5	2.53
Row 14	77.4	2.25
Row 15	130	1.97
Row 16	200	1.9
Row 17		
Row 18		
Row 19		
Row 20		

Lookup Table: 3

	Re_h	K_c
Row 1	1.99	12.8
Row 2	2.83	10
Row 3	3.77	8.12
Row 4	6.08	6.3
Row 5	9.38	4.87
Row 6	12.4	4.17
Row 7	18.6	3.43
Row 8	24.8	3.06
Row 9	37.1	2.65
Row 10	48.5	2.43
Row 11	72	2.19
Row 12	130	1.89

Lookup Table: 3

	Re_h	K_c
Row 13	200	1.82
Row 14	130	1.9
Row 15	200	1.84
Row 16		
Row 17		
Row 18		
Row 19		
Row 20		

Lookup Table: 5

	Re_h	K_c
Row 1	1.24	15.8
Row 2	2.04	11.9
Row 3	3.07	8.9
Row 4	3.71	7.69
Row 5	4.33	6.84
Row 6	4.95	6.22
Row 7	6.171	5.355
Row 8	8.28	4.43
Row 9	10.5	3.87
Row 10	12.29	3.593
Row 11	15.98	3.147
Row 12	17.4	2.995
Row 13	20.7	2.817
Row 14	22.8	2.711
Row 15	30.54	2.462
Row 16	34.5	2.373
Row 17	44	2.201
Row 18	70.52	2
Row 19	130	1.779
Row 20	200	1.76

Lookup Table: 6

	Re_h	K_c
Row 1	1.79	12.37
Row 2	2.395	10.29
Row 3	2.888	8.87
Row 4	3.68	7.328
Row 5	4.303	6.507
Row 6	4.928	5.843
Row 7	6.15	5.084
Row 8	6.768	4.768
Row 9	7.394	4.503
Row 10	8.615	4.112
Row 11	9.835	3.816
Row 12	10.95	3.58
Row 13	12.24	3.402
Row 14	14.08	3.18

Lookup Table: 6

	Re_h	K_c
Row 15	15.88	3.01
Row 16	19.5	2.772
Row 17	24.15	2.577
Row 18	35.85	2.244
Row 19	56.3	2.022
Row 20	129.6	1.755
Row 21	200	1.72

Lookup Table: 400i

	Re	K_h
Row 1	12.74	60.34
Row 2	31.85	25.83
Row 3	63.69	14.47
Row 4	127.4	8.9
Row 5	318.5	5.684
Row 6	636.9	4.52
Row 7	955.4	4.103
Row 8	1274	3.872
Row 9	1911	3.623
Row 10	3185	3.441
Row 11	6369	3.421

Lookup Table: 350i

	Re	K_h
Row 1	12.74	37.97
Row 2	31.85	16.42
Row 3	63.69	9.354
Row 4	127.4	5.909
Row 5	318.5	3.947
Row 6	636.9	3.281
Row 7	955.4	3.022
Row 8	1274	2.879
Row 9	1940	2.68
Row 10	3185	2.653
Row 11	6369	2.668

Lookup Table: 300i

	Re	K_h
Row 1	12.74	22.59
Row 2	31.85	9.967
Row 3	63.69	5.863
Row 4	127.4	3.921
Row 5	318.5	2.868
Row 6	636.9	2.516
Row 7	955.4	2.378
Row 8	1274	2.32

Lookup Table: 300i

	Re	K_h
Row 9	1911	2.243
Row 10	3185	2.223
Row 11	6369	2.24

Lookup Table: 400o

	Re	K_h
Row 1	12.74	58.64
Row 2	31.85	24.66
Row 3	63.69	13.76
Row 4	127.4	8.613
Row 5	318.5	5.739
Row 6	636.9	4.775
Row 7	955.4	4.418
Row 8	1274	4.21
Row 9	1911	3.953
Row 10	3185	3.714
Row 11	6369	3.609

Lookup Table: 350o

	Re	K_h
Row 1	12.74	36.92
Row 2	31.85	16.21
Row 3	63.69	9.099
Row 4	127.4	6.02
Row 5	318.5	4.347
Row 6	636.9	3.788
Row 7	955.4	3.555
Row 8	1274	3.408
Row 9	1911	3.223
Row 10	3185	3.097
Row 11	6369	2.992

Lookup Table: 300o

	Re	K_h
Row 1	12.74	21.96
Row 2	31.85	9.722
Row 3	63.69	5.955
Row 4	127.4	4.268
Row 5	318.5	3.413
Row 6	636.9	3.125
Row 7	955.4	2.981
Row 8	1274	2.891
Row 9	1911	2.737
Row 10	3185	2.662
Row 11	6369	2.727

Lookup Table: High_p

	Re	f
Row 1	0.24	254
Row 2	0.49	126.6
Row 3	0.73	84.17
Row 4	0.97	62.94
Row 5	1.22	50.2
Row 6	1.46	41.71
Row 7	1.7	35.65
Row 8	1.94	31.1
Row 9	2.19	27.56
Row 10	2.43	24.73
Row 11	2.67	22.42
Row 12	2.92	20.49
Row 13	3.16	18.86
Row 14	3.4	17.46
Row 15	3.65	16.25
Row 16	3.89	15.19
Row 17	4.13	14.25
Row 18	4.37	13.42
Row 19	4.62	12.68
Row 20	4.86	12.01
Row 21	5.1	11.4
Row 22	5.35	10.85
Row 23	5.59	10.35
Row 24	5.83	9.891
Row 25	6.08	9.467
Row 26	6.32	9.076
Row 27	6.56	8.715
Row 28	6.8	8.379
Row 29	7.05	8.066
Row 30	7.29	7.774
Row 31	7.53	7.502
Row 32	7.78	7.246
Row 33	8.02	7.006
Row 34	8.26	6.78
Row 35	8.51	6.567
Row 36	17.01	2.965
Row 37	25.52	1.787
Row 38	34.02	1.214
Row 39	42.53	0.8822
Row 40	51.04	0.67
Row 41	59.54	0.5256
Row 42	68.05	0.4231
Row 43	76.55	0.348
Row 44	85.06	0.2919
Row 45	93.56	0.2491
Row 46	102.1	0.2162
Row 47	110.6	0.1905
Row 48	119.1	0.1704
Row 49	127.6	0.1546
Row 50	136.1	0.1421
Row 51	144.6	0.1322

Lookup Table: High_p

	Re	f
Row 52	153.1	0.1244
Row 53	161.6	0.1182
Row 54	170.1	0.1133
Row 55	178.6	0.1094
Row 56	187.1	0.1064
Row 57	195.6	0.1041
Row 58	204.1	0.1023
Row 59	212.7	0.1009
Row 60	221.2	0.09987
Row 61	229.7	0.09914
Row 62	238.2	0.09863
Row 63	246.7	0.09831
Row 64	255.2	0.09813
Row 65	263.7	0.09808
Row 66	272.2	0.09813
Row 67	280.7	0.09826
Row 68	289.2	0.09846
Row 69	297.7	0.09872
Row 70	306.2	0.09903
Row 71	314.7	0.09939
Row 72	323.2	0.09979
Row 73	331.7	0.1002
Row 74	340.2	0.1007
Row 75	348.7	0.1012
Row 76	357.3	0.1018
Row 77	365.8	0.1023
Row 78	374.3	0.103
Row 79	382.8	0.1036
Row 80	391.3	0.1043
Row 81	1500	0.1

Lookup Table: Low_p

	Re	f
Row 1	0.12	467.4
Row 2	0.24	234.2
Row 3	0.35	156.5
Row 4	0.47	117.6
Row 5	0.59	94.31
Row 6	0.71	78.77
Row 7	0.82	67.66
Row 8	0.94	59.33
Row 9	1.06	52.85
Row 10	1.18	47.67
Row 11	1.29	43.43
Row 12	1.41	39.9
Row 13	1.53	36.91
Row 14	1.65	34.34
Row 15	1.76	32.12
Row 16	1.88	30.18
Row 17	2	28.46

Lookup Table: Low_p

	Re	f
Row 18	2.12	26.94
Row 19	2.24	25.57
Row 20	2.35	24.35
Row 21	2.47	23.24
Row 22	2.59	22.23
Row 23	2.71	21.3
Row 24	2.82	20.46
Row 25	2.94	19.68
Row 26	3.06	18.96
Row 27	3.18	18.3
Row 28	3.29	17.68
Row 29	3.41	17.11
Row 30	3.53	16.57
Row 31	3.65	16.07
Row 32	3.76	15.6
Row 33	3.88	15.16
Row 34	4	14.74
Row 35	4.12	14.35
Row 36	4.24	13.98
Row 37	4.35	13.63
Row 38	4.47	13.3
Row 39	4.59	12.98
Row 40	4.71	12.68
Row 41	4.82	12.4
Row 42	4.94	12.13
Row 43	5.06	11.87
Row 44	5.18	11.62
Row 45	5.29	11.38
Row 46	5.41	11.16
Row 47	5.53	10.94
Row 48	5.65	10.74
Row 49	5.76	10.54
Row 50	5.88	10.35
Row 51	6	10.16
Row 52	6.12	9.988
Row 53	6.24	9.818
Row 54	6.35	9.655
Row 55	6.47	9.498
Row 56	6.59	9.346
Row 57	6.71	9.2
Row 58	6.82	9.059
Row 59	6.94	8.922
Row 60	7.06	8.79
Row 61	7.18	8.662
Row 62	7.29	8.539
Row 63	7.41	8.419
Row 64	14.82	4.703
Row 65	22.23	3.455
Row 66	29.65	2.824
Row 67	37.06	2.441
Row 68	44.47	2.181
Row 69	51.88	1.992

Lookup Table: Low_p

	Re	f
Row 70	59.29	1.848
Row 71	66.7	1.733
Row 72	74.11	1.639
Row 73	81.53	1.56
Row 74	88.94	1.493
Row 75	96.35	1.435
Row 76	103.8	1.384
Row 77	111.2	1.339
Row 78	118.6	1.298
Row 79	126	1.261
Row 80	133.4	1.227
Row 81	140.8	1.197
Row 82	148.2	1.168
Row 83	155.6	1.142
Row 84	163.1	1.118
Row 85	170.5	1.095
Row 86	177.9	1.074
Row 87	185.3	1.054
Row 88	192.7	1.035
Row 89	200.1	1.017
Row 90	207.5	0.9999
Row 91	214.9	0.9838
Row 92	222.3	0.9686
Row 93	229.8	0.9541
Row 94	237.2	0.9402
Row 95	244.6	0.927
Row 96	252	0.9143
Row 97	259.4	0.9022
Row 98	266.8	0.8906
Row 99	274.2	0.8794
Row 100	281.6	0.8687
Row 101	289.1	0.8583
Row 102	296.5	0.8484
Row 103	303.9	0.8388
Row 104	311.3	0.8295
Row 105	318.7	0.8206
Row 106	326.1	0.8119
Row 107	333.5	0.8035
Row 108	340.9	0.7954
Row 109	348.3	0.7876
Row 110	355.8	0.78
Row 111	363.2	0.7726
Row 112	370.6	0.7654
Row 113	378	0.7584
Row 114	385.4	0.7516
Row 115	392.8	0.745
Row 116	400.2	0.7385
Row 117	407.6	0.7322
Row 118	415	0.7261
Row 119	422.5	0.7201
Row 120	429.9	0.7143
Row 121	437.3	0.7085

Lookup Table: Low_p

	Re	f
Row 122	444.7	0.7029
Row 123	452.1	0.6974
Row 124	459.5	0.6921
Row 125	466.9	0.6868
Row 126	474.3	0.6816
Row 127	481.7	0.6765
Row 128	489.2	0.6716
Row 129	496.6	0.6709
Row 130	504	0.6664
Row 131	511.4	0.6621
Row 132	518.8	0.6578
Row 133	526.2	0.6537
Row 134	533.6	0.6496
Row 135	541	0.6456
Row 136	548.5	0.6417
Row 137	555.9	0.6378
Row 138	563.3	0.6341
Row 139	570.7	0.6304
Row 140	578.1	0.6267
Row 141	585.5	0.6232
Row 142	592.9	0.6197
Row 143	600.3	0.6162
Row 144	607.7	0.6128
Row 145	615.2	0.6095
Row 146	622.6	0.6063
Row 147	630	0.6031
Row 148	637.4	0.5999
Row 149	644.8	0.5968
Row 150	652.2	0.5938
Row 151	659.6	0.5908
Row 152	667	0.5878
Row 153	674.4	0.5849
Row 154	681.9	0.5821
Row 155	689.3	0.5792
Row 156	696.7	0.5765
Row 157	704.1	0.5738
Row 158	711.5	0.5711
Row 159	718.9	0.5684
Row 160	726.3	0.5658
Row 161	733.7	0.5632
Row 162	741.1	0.5607
Row 163	748.6	0.5582
Row 164	756	0.5558
Row 165	763.4	0.5533
Row 166	770.8	0.551
Row 167	778.2	0.5486
Row 168	785.6	0.5463
Row 169	793	0.544
Row 170	800.4	0.5417
Row 171	807.9	0.5395
Row 172	815.3	0.5373
Row 173	822.7	0.5351

Lookup Table: Low_p

	Re	f
Row 174	830.1	0.533
Row 175	837.5	0.5309
Row 176	844.9	0.5288
Row 177	852.3	0.5267
Row 178	859.7	0.5247
Row 179	867.1	0.5226
Row 180	874.6	0.5207
Row 181	882	0.5187
Row 182	889.4	0.5168
Row 183	896.8	0.5148
Row 184	904.2	0.5129
Row 185	911.6	0.5111
Row 186	919	0.5092
Row 187	926.4	0.5074
Row 188	933.8	0.5056
Row 189	941.3	0.5038
Row 190	948.7	0.502
Row 191	956.1	0.5003
Row 192	963.5	0.4986
Row 193	970.9	0.4968
Row 194	978.3	0.4952
Row 195	985.7	0.4935
Row 196	993.1	0.4918
Row 197	1001	0.4902
Row 198	1008	0.4886
Row 199	1015	0.487
Row 200	1023	0.4854
Row 201	1030	0.4838
Row 202	1038	0.4823
Row 203	1045	0.4807
Row 204	1052	0.4792
Row 205	1060	0.4777
Row 206	1067	0.4762
Row 207	1075	0.4748
Row 208	1082	0.4733
Row 209	1089	0.4719
Row 210	1097	0.4704
Row 211	1104	0.469
Row 212	1112	0.4676
Row 213	1119	0.4662
Row 214	1127	0.4648
Row 215	1134	0.4635
Row 216	1141	0.4621
Row 217	1149	0.4608
Row 218	1156	0.4595
Row 219	1164	0.4581
Row 220	1171	0.4568
Row 221	1178	0.4556
Row 222	1186	0.4543
Row 223	1193	0.453
Row 224	1201	0.4518
Row 225	1208	0.4505

Lookup Table: Low_p

	Re	f
Row 226	1215	0.4493
Row 227	1223	0.4481
Row 228	1230	0.4469
Row 229	1238	0.4456
Row 230	1245	0.4445
Row 231	1253	0.4433
Row 232	1260	0.4421
Row 233	1267	0.441
Row 234	1275	0.4398
Row 235	1282	0.4387
Row 236	1290	0.4375
Row 237	1297	0.4364
Row 238	1304	0.4353
Row 239	1312	0.4342
Row 240	1319	0.4331
Row 241	1327	0.432
Row 242	1334	0.4309
Row 243	1341	0.4299
Row 244	1349	0.4288
Row 245	1356	0.4278
Row 246	1364	0.4267
Row 247	1371	0.4257
Row 248	1379	0.4247
Row 249	1386	0.4236
Row 250	1393	0.4226
Row 251	1401	0.4216
Row 252	1408	0.4206
Row 253	1416	0.4196
Row 254	1423	0.4187
Row 255	1430	0.4177
Row 256	1438	0.4167
Row 257	1445	0.4158
Row 258	1453	0.4148
Row 259	1460	0.4139
Row 260	1467	0.4129
Row 261	1475	0.412
Row 262	1482	0.4111
Row 263	1490	0.4102
Row 264	1497	0.4092
Row 265	1505	0.4083
Row 266	1512	0.4074
Row 267	1519	0.4066
Row 268	1527	0.4057
Row 269	1534	0.4048
Row 270	1542	0.4039
Row 271	1549	0.403
Row 272	1556	0.4022
Row 273	1564	0.4013
Row 274	1571	0.4005
Row 275	1579	0.3996
Row 276	1586	0.3988
Row 277	1593	0.398

Lookup Table: Low_p

	Re	f
Row 278	1601	0.3971
Row 279	1608	0.3963
Row 280	1616	0.3955
Row 281	1623	0.3947
Row 282	1631	0.3939
Row 283	1638	0.3931
Row 284	1645	0.3923
Row 285	1653	0.3915
Row 286	1660	0.3907
Row 287	1668	0.3899
Row 288	1675	0.3892
Row 289	1682	0.3884
Row 290	1690	0.3876
Row 291	1697	0.3869
Row 292	1705	0.3861
Row 293	1712	0.3854
Row 294	1719	0.3846
Row 295	1727	0.3839
Row 296	1734	0.3832
Row 297	1742	0.3824
Row 298	1749	0.3817
Row 299	1757	0.381
Row 300	1764	0.3803
Row 301	1771	0.3795
Row 302	1779	0.3788
Row 303	1786	0.3781
Row 304	1794	0.3774
Row 305	1801	0.3767
Row 306	1808	0.376
Row 307	1816	0.3754
Row 308	1823	0.3747
Row 309	1831	0.374
Row 310	1838	0.3733
Row 311	1845	0.3726
Row 312	1853	0.372
Row 313	1860	0.3713
Row 314	1868	0.3706
Row 315	1875	0.37
Row 316	1883	0.3693
Row 317	1890	0.3687